

UNIVERSITY OF COPENHAGEN
NIELS BOHR INSTITUTE



Ph.D. Thesis

Julian Curry Robinson-Tait

**Cavity Enhanced Phase Measurements
and Continuous Atomic Clocks**

Advisor: Jörg Helge Müller

This thesis has been submitted to the Ph.D. School of The Faculty of Science,
University of Copenhagen on 30.09.2024

Abstract

The advancement of optical atomic clocks leads to new methods of testing fundamental physics, and discovering impactful applications for society. A technological gap exists for an atomic clock that is better than what can be achieved with vapor cells but less complicated than the best optical atomic clocks.

This thesis explores themes of optical atomic clocks based on continuous and passive cavity-enhanced phase measurements of neutral ^{88}Sr . These methods may be a simpler way of realizing state-of-the-art atomic clocks that maintain high performance. We study two regimes that differ in the number of atoms: the weak and the strong collective cooperativity regimes.

The weak regime is where the atom number is low, and their behavior is linear and classical. We build a ^{88}Sr beam machine from scratch to demonstrate continuous cavity-enhanced phase measurements on a travelling atomic beam. We only use the broad cooling transition $^1\text{S}_0 \rightarrow ^1\text{P}_1$ to increase the atomic density and signal size. We use the narrow $^1\text{S}_0 \rightarrow ^3\text{P}_1$ transition of strontium with a decay rate of $2\pi \cdot 7.5\text{kHz}$ as our clock transition and employ a cavity-enhanced measurement technique called NICE-OHMS. The resulting signal has a Doppler-free saturation feature that can be used as a narrow error signal to stabilize a laser. The foundations have been set for the first reporting of a NICE-OHMS measurement on a continuous atomic beam, and only a few technical adjustments are required before the machine can be tested as a frequency standard.

The strong regime is where the atom number is high, and it is qualified by the emergence of collective effects characterized by the theory of cavity quantum electro-dynamics. Our atom-cavity system exhibits a non-linear phenomenon called bi-stability. Two stable solutions can exist for the cavity field for the same input parameters; the chosen solution depends on the history of the atom-cavity system. On a pulsed machine (different from the continuous machine mentioned above), we experimentally explore this regime and employ a simple and versatile measurement scheme inspired by NICE-OHMS that allows cavity phase and transmission information to be retrieved. The phase exhibits a sharp π step linked to the atomic resonance that could be used as an error signal to lock a laser. For a laser stabilized to this error signal, we estimate an achievable short-term stability below $3.7 \cdot 10^{-14} / \sqrt{\tau/1\text{s}}$, assuming a continuous replenishment of atoms into the cavity.

Resumé

Udviklingen af optiske atomure er en lovende vej til nye metoder til at teste grundlæggende fysik og opdage virkningsfulde anvendelser for samfundet.

Denne afhandling udforsker det teknologiske gab for et atomur, der er bedre end hvad der kan opnås med dampceller, men mindre kompliceret end de bedste optiske atomure. Vores udforskning fokuserer på et optisk atomur baseret på kontinuerlige og passive kavitets-forstærkede fasemålinger af strontium-88 atomer. Vi studerer to regimer: de svage og de stærke kollektive kooperativiteter.

Det svage regime er, hvor kavitets transmission er lavt og er lineært og klassisk. Vi bygger en Atom-stråle fra bunden for at demonstrere kontinuerlige kavitetsforstærkede fasemålinger på en bevægende atomstråle. Vi bruger $^1S_0 \rightarrow ^3P_1$ -overgangen i strontium med en henfaldsrate på $2\pi \cdot 7,5$ kHz som vores clock-overgang og anvender en måleteknik kaldet NICE-OHMS, der gør det lettere at undgå kavitetsstøj. Det resulterende signal har en Doppler-fri mætningsfunktion, der kan bruges som et smalt fejlsignal til at stabilisere en laser. Strålemaskinen bruger kun den brede køleovergang $^1S_0 \rightarrow ^1P_1$ til at øge atomtætheden og signalstørrelsen. Grundlaget er lagt for den første NICE-OHMS-måling på en kontinuerlig atomstråle, og det første signal er i horisonten med blot et par tekniske justeringer.

Det stærke regime er, hvor atomtallet er højt, og det er kvalificeret af fremkomsten af kollektive effekter karakteriseret ved teorien om kavitetskvante-elektrodynamik. Vores atom-kavitets system udviser et ikke-lineært fænomen kaldet bi-stabilitet. To stabile løsninger kan eksistere for kavitetsfeltet for de samme inputparametre; den valgte løsning afhænger af historien om atom-kavitets-systemet. På en pulserende maskine (forskellig fra den ovennævnte kontinuerlige maskine) udforsker vi eksperimentelt dette regime og anvender et simpelt og alsidigt måleskema inspireret af NICE-OHMS, der gør det muligt at hente information om kavitetsfase og transmission. Fasen udviser et skarpt π -trin knyttet til atomresonansen, der kunne bruges som et fejlsignal til at låse en laser. Vi estimerer en opnåelig korttidsstabilitet under $3,7 \cdot 10^{-14} / \sqrt{\tau/1 \text{ s}}$, idet vi antager en kontinuerlig genopfyldning af atomer ind i kavitetsmet.

Acknowledgements

Thank you, Jörg Helge Müller, for your supervision and inspiring knowledge of physics, and patience. You are always ready for an in-depth discussion, which I never took for granted.

Thank you, Jan W. Thomsen, for our great physics discussions, your input to the thesis, and your leadership and focus. I look forward to working with you in the coming years.

Thank you, Eliot Bohr and Sofus Kristensen, for being fantastic colleagues and close friends. We really grew together over the last three years; we shared great memories and endeavored arduous times. You guys were instrumental in many of the quality memories of my PhD. I have huge faith that you will excel in your careers, and I look forward to keeping in touch.

Thank you, Andrea Pertoldi, for all the pasta dishes we cooked together and for being an excellent roommate and friend. Living in Copenhagen is not the same now you left.

Thank you, Asbjorn Arvad Jorgensen, for being a great physics sparring partner and, at times of need, also a wise mentor.

Thank you, Stefan Alaric Schäffer, for your continued wisdom and guidance. I look forward to sharing a lab with you in the future.

Thank you, Camila Silva and Jonathan Elsborg. We shared several months working together on the beam machine. You gave me a glimpse into what makes a great team, and I thoroughly enjoyed our time working together. You were the dream team. I hope we keep in touch and have the opportunity to work together again!

Thank you, Omid Vartehparvar and Valentin Combier, for the time we worked together, albeit too brief. I learned a lot from you both. I hope we stay in touch!

Thank you, Eric Planz; it has been a pleasure to take this PhD journey with you from the *very* start, and my life would have looked quite different without you.

Thank you, Jacob Thornfeld Hansen, for the coffee breaks and climbing. You are wickedly smart, and I wish you the best of luck in completing your PhD thesis.

Thank you, Patrik Sund, for being a reliable friend and for the adventures, board games, and brunches.

Thank you, Jade Ajagun-Brauns and Natalie Allen, for being great friends

and for keeping up our countless Panum lunches!

Thank you Mikkell Tang, your simulation skills are unmatched and I learned a lot from you!

Thank you, Bruno Laburthe-Tolra, Benjamin Pasquiou, and Martin Robert-de-Saint-Vincent, for hosting me at the University Paris Nord 13. I learned a lot and enjoyed our discussions, and I wish you the best of success!

Thank you, Peter Bell, my reliable top lad and brother from another mother.

Thank you, Jen, for being there, reminding me there is life outside of work, and for your patience while I wrestled with the thesis writing.

Thank you for everything Mum. You are my role model.

List of Publications

The author contributed to the following publications.

1. Eliot A. Bohr et al. “Collectively enhanced Ramsey readout by cavity sub- to superradiant transition”. *Nature Communications* 15.1 (Feb. 2024), p. 1084.
2. Sofus Laguna Kristensen et al. “Subnatural Linewidth Superradiant Lasing with Cold Sr 88 Atoms”. *Physical Review Letters* 130.22 (May 2023), p. 223402.

The following publications are in preparation and contain the work presented in this thesis.

1. Julian Robinson-Tait et al. “Quadrature Detection of Optical Bistability in the Bad-Cavity Limit” [In preparation]

Table of Contents

Abstract	ii
Resumé	iii
Acknowledgements	iv
List of Publications	vi
1 Introduction	1
1.1 Atomic Clock Principle	2
1.2 Towards Continuous Operation	3
1.3 Thesis Outline	4
1.4 Related Research	5
2 Optical Forces on Strontium and Atomic Beams	8
2.1 Radiation Pressure Force	9
2.2 Magneto-Optical Trap	10
2.3 Strontium	10
2.4 Characterization of Atomic Beams	13
2.5 High Phase-Space Density Atomic Beams	14
3 NICE-OHMS Scheme, Sensitivity and Shifts	17
3.1 Measurement Scheme Overview	19
3.2 Carrier Depleted NICE-OHMS	23
3.3 Stark Shift from Sidebands	25
3.4 Conclusion	29
4 Cavity Enhanced Saturated Spectroscopy on a Slow Beam	30
4.1 Phase Shift from Atoms in a Cavity	31
4.2 Simulations vs Analytical Spectroscopy on a Beam	32
4.3 Conclusion	42

5	The Strontium Beam Machine Construction	43
5.1	Overview	45
5.2	Strontium Oven	48
5.3	Magnetic Coils	49
5.4	Lasers	53
5.5	Optics	56
5.6	Spectroscopy Cavity	58
5.7	Optics for NICE-OHMS	67
5.8	Control with Red-pitaya	67
5.9	Microwave Beat Detection in Cavity Transmission	68
5.10	Testing Microwave Electronics with FM Spectroscopy at Oven Nozzle	70
5.11	Conclusion	72
6	The Strontium Beam Machine Characterization	75
6.1	Overview	75
6.2	Varying Deflection Angle with Compensation Coils	77
6.3	Beam Detection with Camera	79
6.4	Atom Number and Velocities	83
6.5	Next Steps to Continuous Super-radiance	85
6.6	Next Steps to Continuous NICE-OHMS	86
6.7	Conclusion	88
7	Cavity QED and Bi-stability	90
7.1	CQED	90
7.2	Saturation Induced Bi-stability	94
7.3	Driven CQED Enhanced Clocks	99
7.4	Conclusion	100
8	Exploring the Bi-stability Regime with Quadrature Detec- tion	101
8.1	Overview	102
8.2	Finding the Turning Point of a Falling Atom Cloud	107
8.3	Exploring Bi-stability for Different Cavity Pump Rates	112
8.4	Quantitative Analysis	119
8.5	Conclusion	121

9	The Dissipative Ring Trap Concept	123
9.1	Concept	124
9.2	Preparing the Simulation	126
9.3	Static Reference Frame Simulation	131
9.4	Conclusion	133
10	Conclusion and Outlook	134
A	Old Clogged Sr Oven Nozzle	136
B	Atom Number and Flux Calculations	138
C	Atom-Cavity Parameter Summary Table	140

Chapter 1

Introduction

Time, or frequency, is the most accurate base unit the scientific community can measure, thanks to huge advancements in atomic clocks. Two of the best atomic clocks [1, 2] started today would take 40 billion years until they disagreed by 1 s.

The great scientific effort pushing the frontier of frequency metrology allows the exploration of fundamental physics in new ways [3]. This includes setting new limits in the search for dark matter [4], probing general relativity [5] where measurements of gravitation red-shift can resolve height differences below a centimeter, and testing for drifts in fundamental constants [6]. Now that optical atomic clocks are orders of magnitude more precise than the Cs microwave clocks that define the SI second, the push towards redefining the second based on optical atomic clocks is becoming increasingly more pressing [7].

The development of supporting technologies for atomic clocks such as frequency combs, ultra-narrow lasers, and ultra-low expansion (ULE) cavities have applications of their own, such as precision spectroscopy [8], terrestrial and submarine seismology [9], and LIDAR, to name a few.

An equally impactful but immensely technical challenge is reducing the size, weight, and power consumption (SWaP) while still benefiting from the performance of the optical atomic clock. Each trade-off in performance versus SWaP can open new possibilities like chip-based atomic clocks [10], satellite-based gravitation wave detectors [11], and military applications like hold-over clocks for resilience against GPS denial attacks [12].

In this chapter, we give a basic introduction to a passive atomic clock and an outline of research to overcome the limits of state-of-the-art atomic

clocks.

1.1 Atomic Clock Principle

The history of clocks [13] has shown that improving a clock’s ability to measure time goes hand-in-hand with the oscillator’s frequency, the thing that does the *ticking*. This is why the most precise clocks to date use optical light as the oscillator. These oscillations are on the order of $100 \cdot 10^{12}$ per second. Electron transitions in an atom are sensitive to optical light over a very narrow range, so-called the linewidth $\Delta\nu$. The ability to *split-the-line* depends on: the oscillator frequency ν_0 , parameterized by the quality factor $Q = \nu_0/\Delta\nu$; the noise that makes it harder to precisely resolve the linewidth, which is parameterized as the signal-to-noise ratio (SNR); and the type of noise which qualifies how the standard deviation goes down with more data points i.e. a longer averaging time τ . Combining Q , the SNR, and assuming white noise, we can estimate the ultimate fractional frequency uncertainty $\sigma_y(\tau)$:

$$\sigma_y(\tau) \approx \frac{1}{K} \frac{1}{Q} \frac{1}{\text{SNR}} \frac{1}{\sqrt{\tau}} \quad (1.1)$$

Here, K is a value dependent on the measurement scheme. The frequency uncertainty is a simplified but useful metric to relate clocks of different architectures and quantify the general improvement of frequency metrology over time. To date, the best optical lattice atomic clock has a fractional uncertainty of $8 \cdot 10^{-19}$ [1], and the best ion clock is at $9.4 \cdot 10^{-19}$ [2].

There are two ways of measuring the frequency reference: passively or actively. We first focus on the passive case because it is most closely related to the topic of this thesis. The atom is interrogated with a voltage-controlled oscillator (e.g., a laser), and a response from the atom is seen when the oscillator is close to its electronic transition resonance, for example, in the form of scattered light. The transmitted signal from the atoms is used to generate an error signal to steer the oscillator to the atomic resonance by closing a feedback loop (see figure 1.1). This technique is used in the Cs microwave clock, optical lattice clock, and ion clock.

A frequency reference or frequency standard becomes an optical atomic clock once the systematic shifts have been meticulously measured in an error

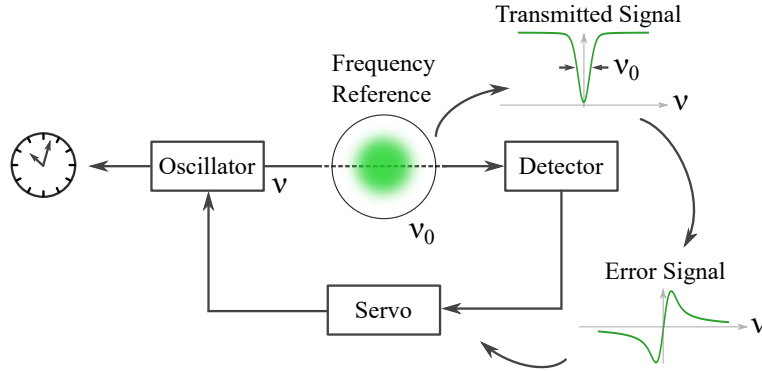


Figure 1.1: **Passive Frequency Reference.** A simple feedback loop for a frequency reference.

budget, and the operating frequency has been compared to another atomic clock and linked to the definition of the SI second.

1.2 Towards Continuous Operation

Further research and development to improve the state-of-the-art optical clocks is likely only to reveal more applications of atomic clocks and fundamental discoveries. However, the very best neutral atom optical atomic clocks are limited by their pulsed operation. They have in-built dead-times between frequency measurements where the feedback loop is paused, leading to Dick noise [14]. The noise comes from the aliasing of higher frequencies down to low frequencies and is now the dominant noise source that limits the time required to reach a certain fractional frequency uncertainty.

At present, the primary motivation for pulsed operation is the laser light used to trap the atoms shifts and broadens the clock transition, so it must be switched off during interrogation. During this time, the atom cloud can expand, fall due to gravity, and collide with background gases, meaning fresh atoms must be prepared before another frequency measurement can be made. The frequency measurement is typically based on fluorescence, which also heats the atoms, destroying the atomic cloud. This has led to research in non-destructive measurements [15, 16], but still does not solve the problem completely.

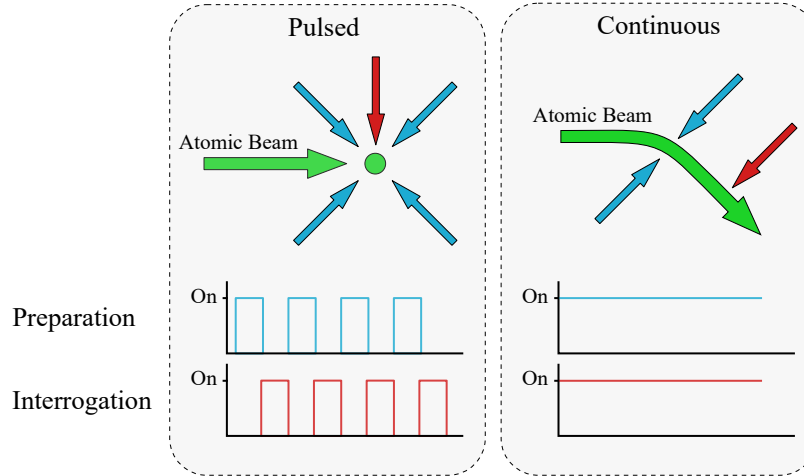


Figure 1.2: **Pulsed versus Continuous Clocks.** An abstract model showing the difference between a pulsed system that prepares and interrogates at the same point versus a continuous system where the preparation and interrogation are separated in space.

Another possible solution to avoid the Dick noise is interleaving two atomic clocks [17, 18] or preparing two separate atom clouds in the same chamber and measuring them alternatively. This can effectively remove the dead time by replacing it with the up-time of a second clock, but it can suffer from systematic shifts between the two clocks, and it will certainly increase the complexity. A potentially simpler route, and one of the main topics of this thesis, is whether preparation and interrogation can be separated in space and carried out continuously (see figure 1.2), fully eliminating Dick noise. A continuous system comes with its challenges, namely reaching the same atomic density and characterizing and controlling the additional systematic shifts that come from frequency measurements on a traveling atomic beam.

1.3 Thesis Outline

To compensate for the lack of atomic density in a beam architecture frequency standard, we investigate using optical cavities to enhance the light-matter interaction.

The thesis can be divided into three parts, with an overarching theme

of cavity-enhanced measurements of atomic clouds and continuous optical frequency standards.

Chapters 2-6 concern the study of applying a phase-sensitive measurement scheme NICE-OHMS to realize a continuous frequency standard on an atomic beam. The theory of laser cooling (2), the cavity-enhanced measurement scheme NICE-OHMS (3), saturated spectroscopy on a beam (4), and construction (5) and characterization (6) of a beam machine designed for continuous frequency metrology on the $^1S_0 \rightarrow ^3P_1$ transition of strontium. We set a solid foundation for the theory and built a fully functional and characterized beam machine. Due to a lack of time and resources, we were unable to perform a frequency measurement in time to be included in this thesis. These chapters represent the bulk of the author's contributions during his PhD project, and the author led the designing, building, and operation of every part of the beam machine.

Chapters 7-8 concern the theory (7) and experimental results (8) of passive quadrature detection of a driven cavity QED system in the bad cavity regime, suspected to be a system attractive for frequency metrology [19, 20]. Taking inspiration from previous work [21], we study the dynamics at a time-scale that can be considered *quasi-continuous* but on a pulsed system (i.e. not the system detailed in chapters 5 and 6 but a neighbouring experiment). Work in chapter 3 also inspired the measurement scheme. The author led the design of the measurement methods, data taking, and analysis, with help from Sofus L. Kristensen, Eliot Bohr, and Stefan A. Schäffer.

Chapter 9 details numerical simulations of a novel type of circulating magneto-optical trap that could miniaturize and simplify a beam machine and be part of a robust and compact continuous atomic clock. The author had the original idea and was the main developer of this concept with physics sparring from Stefan A. Schäffer and Jörg Helge Müller.

1.4 Related Research

We now introduce some related research themes in optical atomic clocks linked to continuous operating optical atomic for context, but not featured in this thesis.

1.4.1 Optical Super-Radiant Laser

A huge technical load is carried by the narrow-linewidth clock laser locked to a ULE cavity when realizing an optical atomic clock. The laser must have a long enough coherence time that matches or exceeds the atomic transition linewidth and must act as a flywheel with sufficient stability to cover the dead time in pulsed clock operation [22]. The ULE cavities are so well-engineered now that they are limited by the Brownian motion of the mirrors. Cryogenic cavities [23] can reduce the Brownian motion, but it is still the limiting factor. The path is unclear on how further improvements in ULE cavities will be made, and the ultimate precision of optical atomic clocks relies on them.

An optical atomic clock based on a continuous superradiant laser, otherwise known as an active clock, is a promising route to relaxing the extreme demands of the clock laser. The principle of operation is that an ensemble of atoms is excited, and if a part of their emission is reused to stimulate more emission, the output power can be extremely coherent. In this case, the light directly emitted from the atoms constitutes the clock laser while inheriting the absolute frequency of an atomic transition. This technique is used in the active hydrogen maser [24] and gas lasers such as the He-Ne laser [13], but has yet to be demonstrated continuously on a narrow optical clock transition. So far, this has been demonstrated in a pulsed fashion [25, 26] and recently, a single pulse was also shown to produce light with an emission linewidth almost an order of magnitude below the natural linewidth of the atomic transition [21], confirming the feasibility of the concept. Still, more work needs to be done to reach fully continuous lasing, which would also eliminate Dick noise. Several groups now pursue a proposal for a continuous superradiant laser based on a simple *hot* beam architecture [27].

1.4.2 Nuclear Clocks

Taking the notion of a higher frequency oscillator enables higher accuracy frequency measurements one step further; researchers are pursuing a transition in the nucleus of Th-232 using laser light in the deep UVC range at 148 nm [28] as a potential frequency reference for a *nuclear* clock. This wavelength's oscillation frequency has an additional factor of 4 compared to the frequency of the optical lattice clock [1] using 689 nm light. However, the real advantage comes when the thorium atoms are doped into a crystal lattice. The lattice

confinement is so strong that the motion is below the excitation wavelength (Lamb-Dicke regime), suppressing first-order Doppler shifts. Since nuclear transitions are also robust to external fields and its chemical environment, nuclear clocks could be a path to solid state, continuously operating nuclear clock. The problems involved with continuous vs pulsed, and lasing cooling and trapping atoms are not applicable. The research in nuclear clocks will be very interesting to follow as the technologies of generating deep UVC laser light matures.

1.4.3 Spin-Squeezing

The quantum projection noise (QPN) limit is a standard limit of any atomic clock relying on independent atoms. This limit can be beaten through careful engineering and readout of atomic states via spin-squeezing. A microwave atomic clock was the first to demonstrate the advantage of spin-squeezing [29, 30], followed by several other optical atomic clock experiments [31]. A lot of effort has been put into spin-squeezing atomic clocks, but the authors of a review [32] argue that spin-squeezing offers limited benefits as long as dead-time and laser phase-noise effects are dominant, further motivating the need for continuous optical atomic clocks.

Chapter 2

Optical Forces on Strontium and Atomic Beams

The precise manipulation of atoms with laser light has enabled a huge field of cold neutral atom research. The pioneering work by Claude Cohen-Tannoudji, Steven Chu and William Daniel Phillips awarded them the Nobel Prize in 1997.

Generally, the more atoms contributing to the frequency measurement of an atomic clock, the larger the signal and hence signal-to-noise ratio and the better the frequency reference (as illustrated in equation 1.1). Cooling and compressing atoms into a small region and reducing their spectral spread (Doppler width) with lasers is the main purpose of laser cooling in atomic clocks. We use the concept of phase-space to encapsulate the concept of cooling and compression, and so the largest phase-space density is the figure of merit for laser cooling atomic clouds and beams.

In this chapter, we will cover the details of the radiation pressure force, how it can be used to create a magneto-optical trap (MOT)[33], and include overview of the literature on atomic beams and how their phase-space density has been enhanced by laser forces. This chapter gives context for the entire thesis, especially chapters 5 and 6 that give details about the beam machine built by the author for continuous frequency metrology.

2.1 Radiation Pressure Force

The scattering force on an atom relies on the repeated absorption of photons with momentum. Each photon absorbed provides a small momentum kick, and for a collimated and monochromatic laser beam, a net force can be produced. For a two-level atom, the force \mathbf{F} relates to:

$$\mathbf{F} = \hbar\mathbf{k}\gamma\rho_{ee} = \hbar\mathbf{k}\frac{\gamma}{2}\frac{s_0}{1 + s_0 + 4\left(\frac{\delta}{\gamma}\right)^2} \quad (2.1)$$

$$\mathbf{k} = k\hat{k} \quad (2.2)$$

Here, \mathbf{k} is the wavevector of the laser beam, γ is the natural decay rate of the atomic transition, s_0 is the saturation parameter, and δ is the detuning including the Doppler shift:

$$\delta = \omega - \omega_a + \mathbf{v} \cdot \mathbf{k} \quad (2.3)$$

Here, ω is the laser frequency, ω_a is the atomic resonance frequency, $\mathbf{v} \cdot \mathbf{k}$ is the dot product of the velocity vector and wavevector corresponding to the Doppler shift in three dimensions.

Two counter-propagating beams that are red-detuned by approximately half the natural decay rate of the atomic transition, $\omega - \omega_a \approx -\gamma/2$ will act to remove velocity along $\pm\hat{k}$, provided the atom is in the capture velocity. This is called an optical molasses because the atom is slowed by a resistive force.

While the average speed of an atom in optical molasses is dampened to zero, the kinetic energy $\langle v^2 \rangle$, and therefore the temperature, balances to a finite value due to the competition between heat removed and heat added by random recoils from spontaneous emission. For optimal parameters, the Doppler limited temperature T_D is:

$$k_B T_D = \hbar\gamma/2 \quad (2.4)$$

Although radiation pressure can produce very large accelerations, the force saturates as s_0 approaches and exceeds one because the rate of stimulated emission increases and momentum is transferred in the opposite direction to absorption, resulting in no additional net force. However, more complicated stimulated emission-enhanced cooling techniques exist, like bi-chromatic cooling [34] and SWAP cooling [35] that can beat the saturation limit by up to a factor of 10.

2.2 Magneto-Optical Trap

To introduce a position dependence to the force and achieve compression and ultimately trapping, the magnetic hyperfine states can be used along with a magnetic field to provide an extra degree of freedom to tune the laser in and out of resonance dependent on a position in space. In the simplest case, we take the transition in the form $J_g = 0 \rightarrow J_e = 1$ where J is the total electronic angular momentum for L-S coupling. J defines the number of magnetic states by $2J + 1$. A ground state that has no magnetic states simplifies this example. This shift of the magnetic states is called the Zeeman shift and for the magnetic state m_j , the energy splitting is:

$$\Delta E = \mu_B B m_j g_J \quad (2.5)$$

Here, B is the magnetic field magnitude aligned along the quantization axis, μ_B is the Bohr magneton and g_J is the Landé g-factor. Figure 2.1 shows this shift in 1D for a magnetic field gradient a_B that follows $B = a_B z$ so the magnetic field is zero at $z = 0$ which defines the center of the trap. For an atom at rest, only the state $m_j = +1$ is Zeeman shifted into resonance when $z > 0$, meaning σ^+ polarized light coming from the right will scatter light, pushing the atom towards lower z . The same is true in reverse for an atom at rest at $z < 0$, the $m_j = -1$ state is shifted into resonance of the σ^- polarized laser. In the case where the atom is at rest at $z = 0$, light from both directions is absorbed by the atom equally, so no net force is produced.

Extending this picture into 3D by introducing light along each axis confines an atom to a single point in space, known as a magneto-optical trap (MOT). The magnetic field is generated by a pair of anti-helmholtz coils, comprised of two coils of the same radius, and spaced by one radius. The current is sent in opposite directions as depicted in figure 2.1 so the magnetic field cancels at the center $x, y, z = 0$.

2.3 Strontium

Divalent atoms like Mg, Ca, and Sr bear symmetries in their energy level structure because their electron structure can be simplified to a charged nucleus with effectively 2 orbital electrons. The 2 electrons allows for richer energy level structure with transitions in the visible wavelengths compared

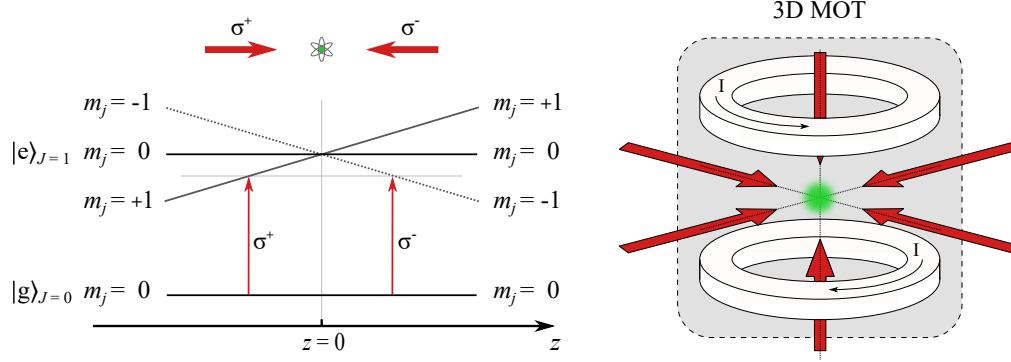


Figure 2.1: Zeeman Levels and the 3D MOT.

to monovalent atoms like K, Rb, and Cs with their single effective orbital electron.

Strontium's energy level structure in figure 2.2 has three main transitions relevant for clocks from its ground-state. The broadband cooling transition $^1S_0 \rightarrow ^1P_1$ has a large natural decay rate of $2\pi \cdot 30$ MHz so can be used to reach large laser decelerations over a broad velocity capture range. This transition is not fully closed, and some atoms are lost from the cycling transition during cooling due to $^1P_1 \rightarrow ^1D_2$ with a branching ratio of around 1:50 000. The Doppler limit is 0.7 mK which is low enough¹ for transfer into the capture range of the narrowband cooling transition $^1S_0 \rightarrow ^3P_1$ with a natural decay rate of $2\pi \cdot 7.5$ kHz, which can bring trapped atoms down to a few μ K temperatures. The clock transition $^1S_0 \rightarrow ^3P_0$ used in the best optical lattice clock [1] can split the line to a fractional frequency to below a fraction uncertainty of 10^{-18} . The clock transition is only available for ^{87}Sr with nuclear spin, but it can be opened with the addition of a strong magnetic field for ^{88}Sr [36].

In the case of this work, we use the $^1S_0 \rightarrow ^3P_1$ transition for our clock operation because it is easier to make lasers with linewidths below $2\pi \cdot 7$ kHz, rather than the immense technical challenges of addressing the $2\pi \cdot 1$ mHz transition. The insights from a novel clock operating on the kHz transition will be extremely valuable in ultimately realizing a clock on the mHz-narrow

¹A few tricks are usually played to enhanced the transfer efficiency, like broad-band cooling.

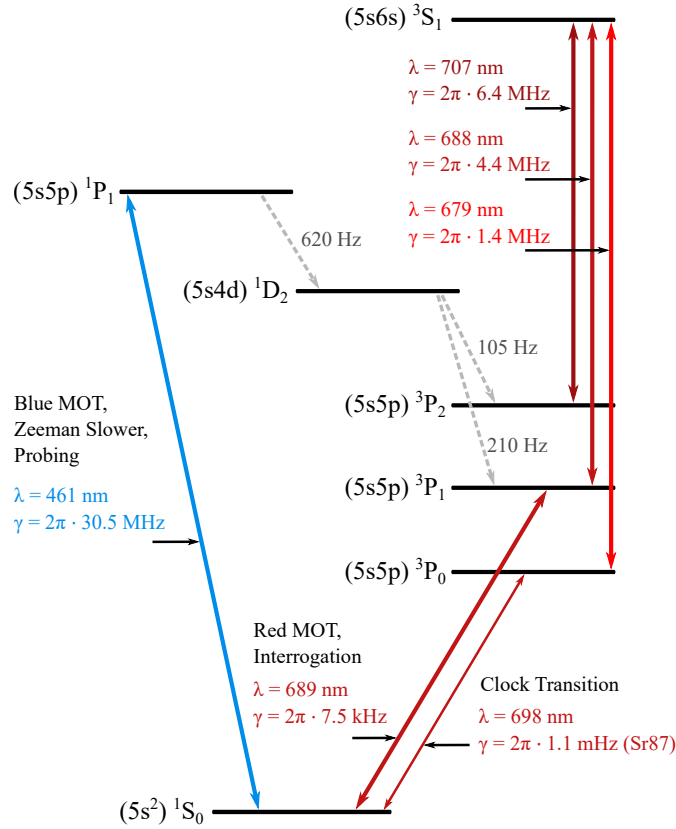


Figure 2.2: **Grotrian Diagram for Sr.** The Grotrian diagram shows the key transitions relevant for this work: the dipole-allowed $^1S_0 \rightarrow ^1P_1$ transition for broadband laser cooling, and the inter-combination line $^1S_0 \rightarrow ^3P_1$ for narrow-band laser cooling and also used as our clock-transition. The typical clock transition used in the best atomic clocks $^1S_0 \rightarrow ^3P_0$ is shown here for reference but is not used in this work. The transitions to 3S_1 are also here for reference, commonly used to arrange the population of atoms in the $(5s5p) \ ^3P$ states and sub-states.

clock transition. This also means we do not have to use ^{87}Sr and gain in atomic flux and signal by opting for the 10 times more abundant isotope ^{88}Sr .

2.4 Characterization of Atomic Beams

Norman Ramsey's textbook on Molecular Beams [37] is a reliable source for key concepts, and here we will summarize a few of the important equations necessary for the rest of the thesis.

A beam is typically produced by heating material in an oven, and the atomic vapor leaks out of a small hole in the oven lid. The resulting beam differential intensity versus velocity $dI(v)$, with a given velocity v along the axis of propagation, is described by:

$$dI(v) = \frac{2I_0}{\alpha^4} v^3 \exp(-v^2/\alpha^2) dv \quad (2.6)$$

$$\alpha = \sqrt{2k_B T/m} \quad (2.7)$$

Here, integrating $dI(v)$ over all velocities results in I_0 , α is the characteristic velocity (1.22 α is the median velocity and 1.33 α is the mean velocity), k_B is the Boltzmann constant, m is the mass of the atoms in the beam, and T is the temperature of the oven. In the example of a strontium beam, the typical operating temperatures are around 520-550 C and results in velocities on the order of $300 \text{ m} \cdot \text{s}^{-1}$.

Attributing the property of temperature to an atomic beam or atomic cloud along the z -axis, the temperature can be defined as:

$$T_z = \frac{\langle v_z^2 \rangle m}{k_B} \quad (2.8)$$

The corresponding Doppler full-width at half-max (FWHM) Γ_{Dop} is:

$$\Gamma_{\text{Dop}} = 2\nu/c\sqrt{2 \log(2)k_B T/m} \quad (2.9)$$

Where ν is the transition frequency and c is the speed of light.

2.5 High Phase-Space Density Atomic Beams

As previously mentioned, high-density atomic ensembles typically lead to measurements with larger signal sizes, which is important for a frequency reference. There are several figures of merit that describe the density and temperature of an atomic beam, and the chosen figure of merit depends on the application. An overview of the different metrics is given in [38], but since the publications discussed in this section use different metrics, we will just take them case by case. Not all of the publications use their beam experiments for frequency metrology.

We can broadly categorize the different beam regimes as thermal or hot if the beam velocity is straight out of the source or oven, and slow or cold if it has been laser cooled².

The Ludlow group in the US (NIST) [39] demonstrated a Ramsey-Bordé interferometer scheme on two counter-propagating thermal beams of calcium and demonstrated a fractional instability of 10^{-16} without the need for vibration isolation. This work is notable because, to date, it is the best continuous optical atomic clock, and the authors claim there was room for improvement. The atomic beams do not undergo any laser cooling or compression. The counter-propagating atomic beams are used to measure and cancel the systematic shifts associated with spectroscopy on atoms with a fast-moving center of mass. This system is roughly two decades in fractional uncertainty away from the state of the art [1], which is a testament to the potential of frequency references based on atomic beams and that there could be plenty more improvement with the introduction of laser cooling.

The Robert-de-Saint-Vincent and Laburthe-Tolra group in France (Paris Nord 13)[40] show a shelving spectroscopy scheme on a strontium atomic beam straight from an oven and achieve a fractional instability of $2 \cdot 10^{-12}$, and they estimate the shot-noise limited instability could be down to $3 \cdot 10^{-14}$. They use 689 nm light to shelve atoms into the 3P_1 state but perform readout on the 461 nm to benefit simultaneously from narrow spectral selectivity but also large signal-to-noise read out from the fast scattering transition $^1S_0 \rightarrow ^1P_1$.

The Wilkowski group in Singapore [41] showed a Sr atomic beam which

²It would seem appropriate to include an intermediate category such as *luke-warm* to differentiate the beams with velocities $\text{m} \cdot \text{s}^{-1}$, such as the one built in chapter 5, and $\text{cm} \cdot \text{s}^{-1}$ beams. For now we will stick to hot and cold.

has similarities to the machine built in chapter 5. The atomic beam is first slowed by a Zeeman slower and then deflected with an angled 2D MOT into a 30° off-axis chamber. They chose this extra deflection step to load a 3D MOT inside a chamber that is separated by a differential pumping tube to reach better vacuum pressures and, therefore, longer 3D MOT lifetimes. They implement the magnetic field of their 2D MOT with rectangular coils in the Ioffe configuration, likely enhancing the efficiency of their 2D MOT compared to an anti-Helmholtz configuration. They characterize the deflected atomic beam by monitoring how quickly the MOT was loaded and find a maximum loading rate of $6 \cdot 10^9 \text{ s}^{-1}$. They perform a frequency measurement on the deflected atomic beam on the $^1\text{S}_0 \rightarrow ^3\text{P}_1$ transition and the scattered light collected with a photomultiplier tube. They resolve a saturated feature of 140 kHz on a Doppler envelope of $\Gamma_D = 9.4 \text{ MHz}$. This is a very interesting comparison benchmark for frequency measurements made in the future on the beam machine in chapter 5.

The advantage of having a beam traveling several tens $\text{m} \cdot \text{s}^{-1}$ is that no extra laser forces are required to keep the beam from falling due to gravity over a 10 cm scale. In contrast, the following three experiments/publications are precisely controlled and very slow atomic beams requiring extra measures to counteract gravity, increasing complexity and cost. All the implementations consist of at least two MOT cooling stages and loading into a dipole guide or moving conveyor-belt lattice.

The Schreck group in the Netherlands (Zeeman Institute) [38] demonstrated the first beam with continuous phase-space density greater than 1, meaning the output was a BEC. Due to the machine's complexity, they are building another machine with a simplified design that also incorporates a high finesse optical cavity to realize a super-radiant laser on the mHz transition of ^{87}Sr .

The Thompson group in the US (NIST) [42] demonstrated continuous loading into a high finesse ring-cavity and deterministic positioning using the cavity as an optical conveyor belt. They already observed continuous strong collective coupling.

The Katori group in Japan (RIKEN) [43] demonstrated a continuous outcoupled beam of ^{88}Sr in a moving optical lattice. They plan to make a longitudinal Ramsey interferometer [44] which spatially separates the Ramsey $\pi/2$ -pulses as opposed to the conventional approach of delivering the pulses separated in time on a trapped atom cloud.

All three experiments/publications have aspirations for performing fre-

quency metrology but have not yet demonstrated it, hinting at the significant complexity of building a slow beam continuous atomic clock.

Chapter 3

NICE-OHMS Scheme, Sensitivity and Shifts

A continuous optical atomic clock based on an atomic beam is a promising concept to overcome the Dick noise that limits the best pulsed optical atomic clocks. However, the challenge for continuous operation is reaching a high enough atomic density to compete with the signal-to-noise of pulsed atomic clocks.

A promising solution to recover extra signal-to-noise is to use a Fabry-Pérot enhancement cavity placed around the atomic beam to enhance the interaction length (or optical depth) of the light with the atoms. The lack of atomic density can be exchanged for a smarter measurement method. This method can also be *destructive* because the cavity is continuously replenished with new atoms. A cavity finesse F of above 1000 is routinely achieved, equivalent to enhancing the measurement sensitivity by $2F/\pi$. Sensitivity can be thought of as the minimum detectable signal from the noise. Furthermore, the beam bouncing back and forth in the cavity produces a Lamb dip, a saturation feature that is Doppler-free. In the ideal situation, the center of the saturation feature is pinned to the zero-velocity group and also the unshifted atomic frequency required for the feedback loop of a frequency reference. The uniform curvature of the optical wave-fronts inside the cavity also minimizes shifts and broadenings from distorted wave-fronts [45].

Noise-Immune Cavity-Enhanced Optical-Heterodyne Molecular-Spectroscopy (NICE-OHMS) is a smart measurement scheme that utilizes the benefits of an enhancement cavity while also being resilient to the extra noise from the imperfect laser-cavity stabilization lock. NICE-OHMS is competitive with

the most sensitive techniques for measuring the presence of atoms. It was first proposed in a paper by Ye et al. [46] and is still one of the most sensitive measurement techniques demonstrated to date, although it was performed in 1998. They achieved an optical depth detection sensitivity¹ of $5 \cdot 10^{-13}$ with 1 s integration time. The advantage of this technique comes from the combination of cavity-enhanced absorption spectroscopy with frequency modulation (FM) spectroscopy by choosing the FM frequency to equal the free spectral range (ω_{FSR}) of the cavity. Since a cavity free spectral range is typically in the 100 MHz to few GHz, the beat note is far from 1/f noise which aids in approaching shot-noise limited detection.

Although NICE-OHMS has a reputation for being one of the most sensitive measurement techniques, it has not seen broad adoption because of the nuances in its implementation.

The Axner group at [47, 48, 49] Umea University has made great contributions to the theory and experimental aspects of NICE-OHMS in the high-saturation regime on thermal molecular gas cells for trace gas measurements. They noted that the Kramers-Kronig relationship, which links the absorptive and dispersive properties of a driven two-level atom, breaks down at high saturation. This was instrumental for us to realize that different information could be held in the phase and transmission and motivated the simulations in chapter 4 using a full optical Bloch equation model.

The time and frequency group with Patrick Gill and Anne Curtis at NPL [50] have also made contributions to the use of NICE-OHMS, for example on trace ammonia detection at 1532 nm.

In our own group at the Niels Bohr Institute, NICE-OHMS was performed on a several mK cold strontium cloud [51] in the context of frequency metrology. NICE-OHMS was also studied in the context of iodine gas cells [52]. The results of these works were a strong motivator for the pursuit of NICE-OHMS in this thesis.

In this chapter, we will introduce the scheme, scaling, and limits of NICE-OHMS in the context of approaching shot-noise-limited detection of atoms with a narrow atomic transition. We also identify possible sources of systematic shifts that are important to quantify for frequency metrology.

¹Not to be confused with fractional frequency.

3.1 Measurement Scheme Overview

Conceptually, NICE-OHMS is like an interferometer, but the paths are not separated in space but in optical frequency. A frequency modulation triplet is generated by sending an optical light field through an electro-optical modulator (EOM) (see figure 3.1). All three components of the spectral triplet are transmitted through the cavity; their relative amplitude is maintained even if the total power fluctuates due to the laser frequency noise or cavity resonant frequency noise, thereby earning its laser-cavity *noise-immunity*. The triplet in transmission is measured by a high bandwidth photodiode, and all three components are already perfectly spatially overlapped. Without any atomic phase shift on the carrier, there is no (or small constant) signal because the triplet cancels out. In the presence of a phase shift by atoms, the triplet is unbalanced and a beat note appears. In the presence of atoms, the beat note is mixed with the original modulation source and low-passed to remove harmonics. This results in a signal at baseband that is proportional to the atomic phase shift. An example phase spectrum is shown in figure 4.1.

The same EOM also applies the Pound-Drever-Hall (PDH) sidebands to lock the cavity to the laser. The PDH sidebands do not transmit through the cavity because they are out of resonance with the cavity. They are reflected off the cavity mirror, then detected by an additional photodiode, and used to stabilize the cavity to the laser light (not pictured).

3.1.1 Sensitivity

NICE-OHMS is great at sensing small concentrations of atoms with large signal-to-noise. In this next section, we follow the derivation for the sensitivity in [53] and make inclusions where our specific application for frequency metrology on a narrow atomic transition might change some conclusions about the NICE-OHMS sensitivity.

Beer-Lambert's law of an absorbing medium states the input power P_{in} into a standard cell containing a medium with absorption coefficient α and interaction length L results in an output power P_{out} of:

$$P_{\text{out}} = P_{\text{in}} \exp(-\alpha L) \tag{3.1}$$

In the weak absorption limit, where $\exp(-\alpha L) \approx 1 - \alpha L$, the input power approximately equals the output power $P_{\text{out}} \approx P_{\text{in}} = P_0$ (to follow the notation

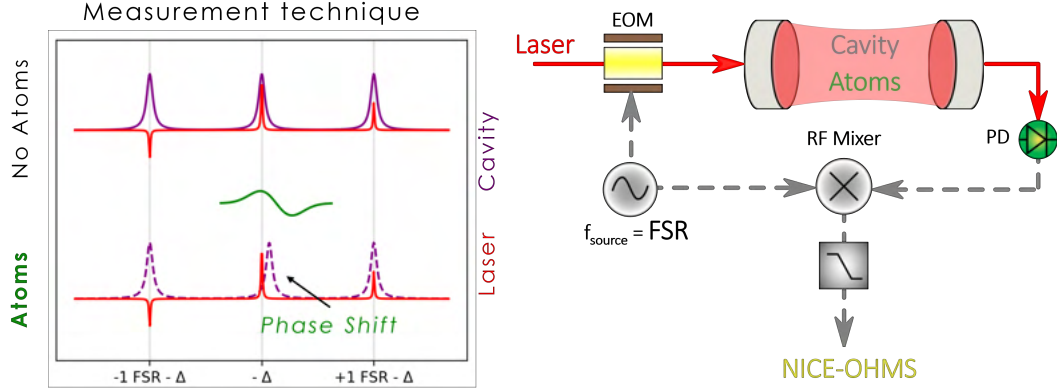


Figure 3.1: **NICE-OHMS Scheme.** Left illustrates the NICE-OHMS scheme where an optical triplet passes through the empty cavity. A phase shift from a medium inside the cavity shifts the cavity resonance and unbalances the triplet. The right shows a simplified diagram of how this scheme may be implemented.

in the literature) so we can use the input power to calculate the shot-noise. The signal contrast is proportional to $P_0(\alpha L)$.

The two noise sources we consider here are the shot noise and detector noise. The shot noise is related to the discreteness of photons and electrons. The statistics of coherent light is Poissonian so for N detected photons, the variance is N . The minimum detectable absorption $(\alpha L)_{\min}$, abbreviated to MDA, on a detector can be described by the sum of variances of the shot-noise and the detector-noise:

$$(\eta P_0(\alpha L)_{\min})^2 = 2eB\eta P_0 + \eta^2\sigma_{\text{NEP}}^2 B \quad (3.2)$$

Where η is the detector responsivity, so ηP_0 is the detected photo-current, B is the measurement bandwidth, and σ_{NEP} is the noise equivalent power² of the detector with units of power per square-root hertz. The addition of the detector noise deviates from the derivation in the literature, but we include it here because detector-noise-dominated measurements are a possibility because low-noise fast-response detectors in the visible wavelengths can be hard to find and are very specialized equipment. The shot noise is uncorrelated

²NEP is defined as the power equivalent to producing a signal on the detector with a signal to noise ratio of 1.

with electronic noise, so the variances can be added. Substituting in for the optical power reaching the detector and detector responsivity η , we get the MDA for a simple single-pass spectroscopy cell.

$$\eta P_0 (\alpha L)_{\min} = \sqrt{2eB \eta P_0 + \eta^2 \sigma_{\text{NEP}}^2 B} \quad (3.3)$$

$$(\alpha L)_{\min} = \sqrt{\frac{2eB}{\eta P_0} + \frac{\sigma_{\text{NEP}}^2 B}{P_0^2}} \quad (3.4)$$

Omitting all other technical noise sources, if the dominant noise contribution is the detector noise, then increasing the power to the detector improves the sensitivity proportional to the power. When the dominant noise is the shot noise, increasing the power to the detector only increases the sensitivity by the square root of the power. This can be an important consideration when designing the measurement scheme.

As [53] points out, a sensitivity of 10^{-8} can be achieved using reasonable detector efficiencies and laser powers for direct single-pass spectroscopy. In practice, realizing this fundamental limit can be close to impossible due to technical noise sources from measuring at baseband. The introduction of the FM triplet allows the spectroscopy information to be kept at a high frequency away from $1/f$ noise, making it easier to approach the shot-noise limited minimum detectable absorption. This modifies the minimum detectable absorption by:

$$(\alpha L)_{\min} = \sqrt{\frac{2eB}{\eta P_0} + \frac{\sigma_{\text{NEP}}^2 B}{P_0^2}} \frac{\sqrt{2}}{J_0 J_1} \quad (3.5)$$

The measurement at higher frequency comes at a price of a factor $\sqrt{2}/J_0 J_1$ increase in the minimum detectable absorption where J_0 and J_1 are the 0-th and 1-st coefficients of the Bessel function for a modulation index β . This factor is always less than 1, and it arises because some of the total power is pushed into the sidebands, reducing the power used to interrogate the atoms.

Finally, introducing the cavity has a direct linear improvement of the MDA with respect to finesse. For a given input power, the cavity acts to amplify the number of passes the light makes through the atoms and changes the MDA by:

$$(\alpha L)_{\min} = \frac{\pi}{2F} \sqrt{\frac{2eB}{\eta P_0} + \frac{\sigma_{\text{NEP}}^2 B}{P_0^2}} \frac{\sqrt{2}}{J_0 J_1} \quad (3.6)$$

The minimum detectable absorption decreases (improves) linearly with cavity finesse. This has an important consequence in implementing a real cavity with optical losses. We can parameterize this with a transmission efficiency factor β_L , which has a value between 0 and 1 where 0 is no transmission. Now, the cavity transmitted power $P_{\text{cav}} = P_0 \beta_L$ replaces P_0 in equation 3.6. Being shot-noise dominated or being detector noise dominated changes the scaling for input powers P_0 , so in some cases, the inclusion of a cavity could be a hindrance.

So far, a summary of the scaling of the theoretical limit for the NICE-OHMS detection sensitivity has been presented. However, the scaling implied in this equation neglects a few important technical and physical details. We do not attempt to modify the equation to account for these details here but include it for discussion and provide citations where possible for further consideration.

Equation 3.6 is derived from arguments related to Beer-Lambert law of absorption through a medium. However, what is actually measured by NICE-OHMS is the phase-shift. In the low atomic saturation limit, the absorption and phase-shift are linked by the Kramer-Kronig relation. This relation is true when the saturation parameter $s_0 < 1$, which is the ratio of the laser intensity I and the atomic saturation intensity I_{sat} is small such that:

$$I_{\text{sat}} = \frac{\hbar\omega_a\gamma}{2\sigma_0} \quad (3.7)$$

$$s_0 = \frac{I}{I_{\text{sat}}} \quad (3.8)$$

Where $\hbar\omega_a$ is the photon energy of the atomic transition, γ is the natural decay rate of the transition, and σ_0 is the scattering cross-section. However, for atomic transitions that are narrow (i.e. small γ) and for typical light intensities circulating in a cavity (i.e. large I), s_0 can be larger than one even for very low cavity input powers (1 nW and less). In the high saturation limit, $s_0 > 1$, the Kramer-Kronig relationship no longer holds true. The authors in [47, 49] make an in-depth derivation of the minimum detectable phase (the phase equivalent of the minimum detectable absorption) in the high saturation regime. They also develop an analytical equation for line-shape that

includes the details for saturated spectroscopy. A critically important claim in the paper is that spectroscopy techniques that utilize phase measurements are affected much less than direct absorption measurements, and they introduce the concept of *saturation-insensitive* detection. Their derivation are very technical and considers thermal gases, so it is not directly applicable to slow atomic beams. We take a more detailed look into the phase from saturated spectroscopy discussion in chapter 4, and for now continue the discussion of the measurement scheme.

3.2 Carrier Depleted NICE-OHMS

For narrow transitions that are interesting for atomic clocks, we would like to have control over the carrier power (i.e. the power that interacts with the atoms) while still using all the optical power available to produce a large beat note in transmission. For NICE-OHMS, the carrier and sideband power are connected by the EOM modulation index, so to avoid having to lower the total power, we introduce "Carrier-Depleted NICE-OHMS", where the microwave power driving the EOM causes phase-modulations on the order of π . This causes the carrier to become depleted while power is pushed into the sidebands without any additional complexity in equipment, as shown in figure 3.2. The electric field $E_0 e^{i(\omega t + \phi)}$ after an EOM follows the relation:

$$E = E_0 e^{i(\omega t + \phi)} \sum_n J_n(\beta) e^{in\Omega t} \quad (3.9)$$

Where $J_n(\beta)$ is the Bessel function of the first kind for a modulation index β and Ω is the modulation angular frequency.

There are nuances to this method that will have to be accounted for. There will be an increased sensitivity to rf input power to the EOM. As shown in the bottom right subplot in figure 3.2, the carrier power drops off rapidly as the increasing modulation index β approaches 2.41. The difference in β between a fractional carrier power of $1 \cdot 10^{-5}$ and $2 \cdot 10^{-5}$ is less than 0.01. Controlling β to 1 part in 1000 should not be too challenging for purpose-designed microwave electronics and a temperature-stabilized EOM. Still, it should be kept in mind, as it could be a source of drift.

Driving the EOM at large modulation index β distributes power into the $n = \pm 2$ and $n = \pm 3$ sidebands. These sidebands will not participate in the useful signal but only introduce more noise. Recently, a method of producing

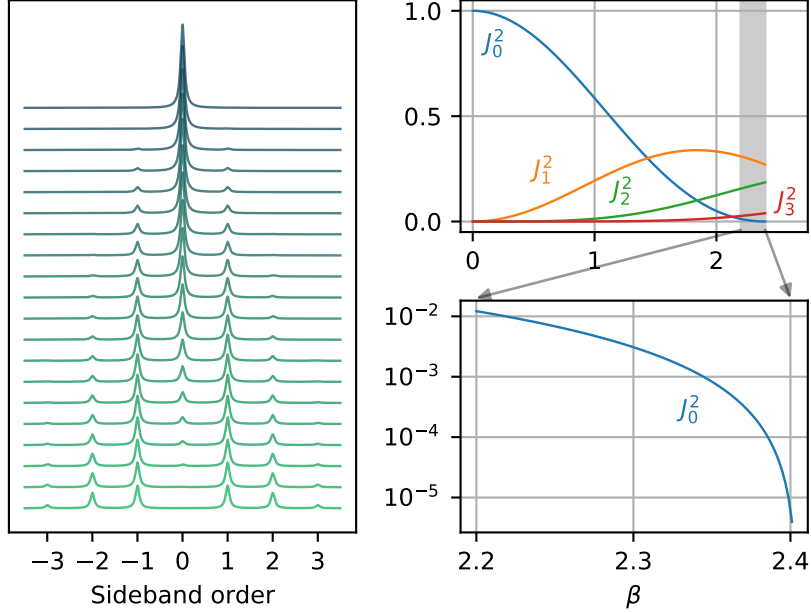


Figure 3.2: **Carrier Depleted NICE-OHMS.** The left shows the spectrum of monochromatic light after phase-modulation by an EOM with increasing β (top to bottom). The spectra are displayed vertically for better visibility. The carrier is depleted, and the power goes into the ± 1 , ± 2 and even ± 3 sidebands for large β . The top right quantifies the proportion of the total power in each sideband, and the bottom right shows how the carrier is depleted on a log graph. For β approaching 2.41, the carrier is almost entirely depleted.

a synthetic FM triplet without extra parasitic sidebands was shown [54] by driving an AOM with two tones instead of an EOM with one tone. That could be considered to avoid this problem. However, the modulation frequency is limited to the AOM bandwidth which is typically < 0.5 GHz, which fixes the minimum cavity length to be larger than 30 cm. Specialized high-frequency AOMs will be required to reach the free-spectral-range of smaller optical cavities.

Even though the sidebands are separated by a ω_{FSR} which is large compared to the linewidth of the transition $\omega_{\text{FSR}}/\gamma \approx 500,000$, the optical intensity is enhanced by the cavity $2F/\pi \approx 1,000$ which may reach intensities strong enough to induce significant AC stark shifts. We quantify this shift

in the next section.

3.3 Stark Shift from Sidebands

The unique aspect of NICE-OHMS is the sidebands, so the perturbing effect from the sidebands on the atoms could be a dominant source of frequency shift or broadening and will be crucial to quantify in an error budget and, worst case, might make the NICE-OHMS scheme unviable for some frequency metrological applications. Here, we try to quantify these concerns for the example of ^{88}Sr on the $^1\text{S}_0 \rightarrow ^3\text{P}_1$ transition.

The AC stark shift E_L on an energy level can be calculated from the real part of the polarizability α :

$$E_L = -\frac{\text{Re}(\alpha) I}{2\epsilon_0 c} \quad (3.10)$$

Where ϵ_0 is the vacuum permittivity, c is the speed of light, and I is the laser intensity. The polarizability of an atom must consider all relevant transitions between nearby energy levels for the ground and excited state, so we take the sum over k for as many transitions as possible for the most accurate polarizability:

$$\alpha_i(\omega_L) = 6\pi\epsilon_0 c^3 \sum_k \frac{A_{ik}}{\omega_{ik}^2(\omega_{ik}^2 - \omega_L^2)} \quad (3.11)$$

Where i is the energy level being shifted. To find the Einstein coefficient for a given transition, A_{ik} , we are usually only given the total transition rate A_T from the excited state to the fine-structure manifold states below. So one further equation allows us to retrieve A_{ik} from A_T :

$$A_{ik} = A_{T,ik} \zeta_{ik} R_{ik} \quad (3.12)$$

Where $\zeta_{ik} = \omega_{ik}^3/\omega_{T,ik}^3$ is the energy correction factor to the transition rate due to the fine-structure splitting, and:

$$R_{ik} = (2L_k + 1)(2J_i + 1) \left\{ \begin{matrix} J_i & 1 & J_k \\ m_i & p & m_k \end{matrix} \right\}^2 \quad (3.13)$$

Where the quantum numbers J is angular momentum, m is the projection of the angular momentum, p is the change in angular momentum, ± 1 for

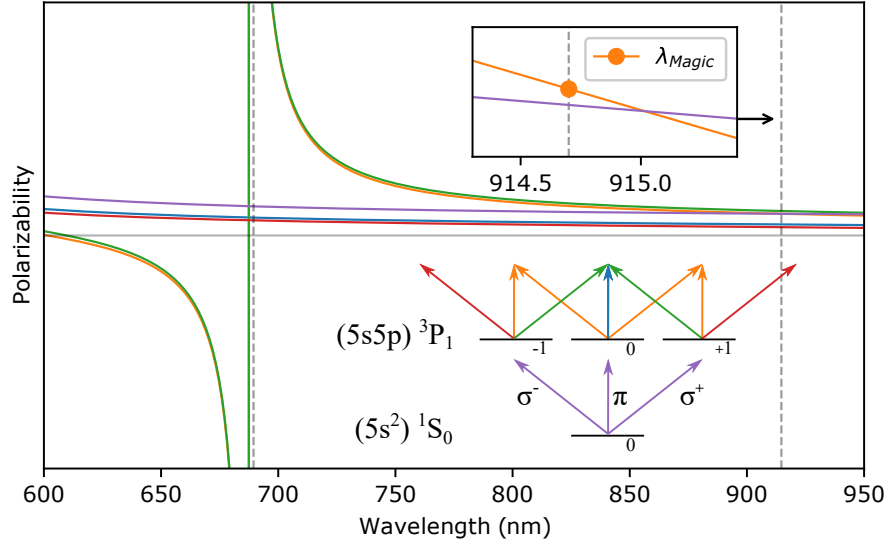


Figure 3.3: **Polarizability of Sr 1S_0 and 3P_1 Energy Levels.** The polarizability landscape is plotted versus wavelength. The inset shows the crossing of 1S_0 and 3P_1 for the magic wavelength for circularly polarized light. It agrees with the known value for the magic wavelength λ_{Magic} . The $J = 0 \rightarrow J = 1$ sublevels are illustrated in the color corresponding to the polarizability. Due to symmetry, several sublevel transitions have the same color.

circular and 0 for linear polarized light, and in braces $\{ \}$ is the Wigner $3j$ -symbol which gives the fraction of the coupling strength between an excited state and lower state. The various transition rates and line frequencies are taken from reference [55] for the first ten orbital states, and reference [56] is used for the $^1S_0 \rightarrow ^3P_1$ transition rate and frequency. Figure 3.3 shows the polarizability for the ground state 1S_0 and 3P_1 . The magic wavelength is the wavelength where the energy shift of both the excited and lower states are equal and is represented by a crossing point. We use this crossing point to help confirm the correct implementation of numbers and equations by showing an agreement with the magic wavelength of less than 1%, which will be sufficient for our requirements.

We extract the difference in AC-stark shift between the 1S_0 and 3P_1 tran-

State	m-state and polarization		Stark shift for saturation parameter 1, (Hz)
	m	p	
3P_1	0	0	0.0456
3P_1	0 or ± 1	± 1 or 0	2.73
3P_1	± 1	∓ 1	2.73
3P_1	± 1	± 1	0.0386
1S_0	0	Any	0.0744

Table 3.1: Calculated Light Shift Table for Sideband.

sition close to the $^1S_0 \rightarrow ^3P_1$ resonance and study how the NICE-OHMS sidebands shift the transition of interest. We only take the shifts for states $m = 0$, which are tabulated in Table 3.1. A significantly large shift on 3P_1 $m = 0$ for circularly polarized light $p = \pm 1$ is due to coupling to the neighboring $^3P_1 \rightarrow (5s6s) ^3S_1$ transition at 688 nm, which can be seen in figure 3.3. The shift is 100 times larger than the shift for linearly polarized light, $p = 0$, because the $m = 0 \rightarrow m = 0$ is forbidden when $J_g \neq 0$. Carefully controlling the quantization axis and polarization will play an important role in reducing the light shift.

As an example case for 1 μ W power in the sideband, the saturation parameter for cavity finesse of 5000 and waist radius 250 μ m is 108000, and a shift between 1S_0 $m = 0$ and 3P_1 $m = 0$ is 3.11 kHz, and increases linearly with power. The size of the shift will only become noticeable when it reaches the same size as the power broadening $\gamma\sqrt{1+s_0}$ and anticipated operating saturation parameter is typically $s_0 = 100$. We do not make any conclusions about whether this AC stark shift is just a shift, or rather a broadening on the lineshape, and we leave this to future work.

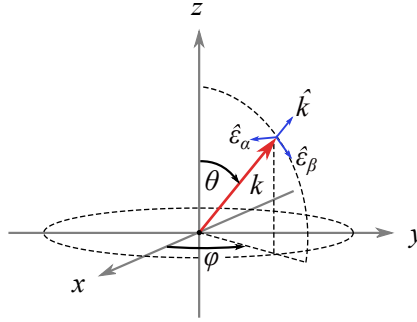
3.3.1 Quantization Axis

From the estimations of the light shift from the NICE-OHMS sidebands on the $^1S_0 \rightarrow ^3P_1$ transition reveals that the σ transitions cause shifts that are 100 times larger than the π transitions. It raises the question about how well the polarization and quantization axis can be practically matched to minimize the shift.

To estimate the impact of a misaligned quantization axis and polariza-

Polarization	Excitation Probability		
	σ_+	σ_-	π
ϵ_α	0.5	0.5	0
ϵ_β	$0.5 \cos^2 \theta$	$0.5 \cos^2 \theta$	$\sin^2 \theta$

Table 3.2: Excitation Probabilities for Polarization and k-vector.

Figure 3.4: **Polarization Coordinate Definition.** The representation of the \hat{k} vector with respect to x, y, z and the polarization $\hat{\epsilon}_\alpha, \hat{\epsilon}_\beta$.

tion, we define a wavevector by $\hat{k}(\theta, \phi)$ in spherical coordinates, where θ is the polar angle between the k vector and the z -axis, and ϕ is the azimuthal angle between the orthogonal projection of k on the x - y plane and the x -axis. The magnetic field vector is aligned along the z -axis that defines our quantization axis, see figure 3.4. For linearly polarized light following the Loudon convention [57], are the decomposition of the horizontal $\hat{\epsilon}_\alpha$ and vertical polarization $\hat{\epsilon}_\beta$ vector. Table 3.2 shows the excitation probabilities of σ_+, σ_-, π transitions with respect to the polarization and \hat{k} vector. Note, the transition probability only depends on θ which makes sense given the rotational symmetry around the z -axis.

Both the quantization alignment relative to the k -vector θ and the purity of the light polarization are important to minimize the probability of σ transitions. For cleaning the polarization, picking out some numbers from Thorlabs inventory of polarization optics, an optical polarizing beam cube has an extinction ratio between transmitted p-polarized and s-polarized of 1000:1, and a Glan-Taylor Calcite polarizers have 100,000:1. Indeed the polarization purity can be scrambled as soon as the light reflects off the wrong surface at the wrong angle or transmits through a slightly birefringent ma-

terial, but we will take 1000:1 as a realistically achievable value. This is sufficient control to purify the vertical polarization to 1 part in 1000.

To minimize the σ transition probability due to misaligned quantization axis, θ must be $\pi/2$ or $3\pi/2$. Taking the Taylor expansion for $\cos^2(\theta)/2$ close to $\pi/2$, we arrive at an estimate for the excitation probability of σ_{\pm} for a misaligned quantization axis:

$$P(\sigma_+; \sigma_-) |_{\pi/2} \approx \frac{1}{2} (\theta^2 + \dots) \quad (3.14)$$

To keep the transition probability $P(\sigma_+; \sigma_-) < 0.01$, θ must be controlled better than $\sqrt{0.02} = 0.14$ rad or 8° , which is easily achievable.

3.4 Conclusion

NICE-OHMS is a technique that has shown some of the highest sensitivity of optical measurement techniques, but following the derivation of the sensitivity reveals nuances involved with driving narrow transitions. We include the importance of a high transmission efficiency cavity and a low noise detector and generally outline the issue by starting from an absorption-based derivation.

We identify the need for greater control of the atom probing power and introduce carrier-depleted NICE-OHMS. This provides much higher control of the carrier probe power with no extra complexity in equipment.

The uniqueness of NICE-OHMS may also be its largest limitation. We quantify the AC-stark shift from the NICE-OHMS sidebands and conclude that the shift can be large compared to the atomic linewidth γ but still small relative to the power broadening. The AC-stark shift for accidentally driving the σ transitions is 100 times larger than for π transitions, so we quantify how carefully the polarization and quantization axis need to be controlled to avoid driving the σ transitions, and we conclude it is very feasible without special equipment.

In the following chapter, we look closer at the numerical and analytical phase spectrum to be detected by NICE-OHMS, in the context of a slow atomic beam of neutral atoms.

Chapter 4

Cavity Enhanced Saturated Spectroscopy on a Slow Beam

Saturated absorption spectroscopy is a well-covered topic in several textbooks [58, 13, 37]. It can produce a Doppler-free feature, meaning the feature's width and line center do not depend on the motion of atoms to first order.

Historically, in the Quantum Metrology lab at the Niels Bohr Institute, Christensen et al. [59] and Schäffer et al. [51] experimentally explore saturated spectroscopy on a cloud of cold atoms that are prepared and trapped in a pulsed machine. They study the regimes of several mK atomic clouds, first with $2.5 \cdot 10^7$ atoms at 5 mK in a cavity with finesse 85 and again with $4 \cdot 10^7$ atoms at 14 mK and cavity finesse 1240. Their measurement is made with NICE-OHMS, the scheme detailed in chapter 3. Their signal-to-noise is huge, and the dominant fluctuations come from the variation in the properties of the atomic cloud between each MOT preparation. The pulsed nature makes it difficult to qualify the system's noise properties. They suggest great potential in using saturated spectroscopy on dense clouds of atoms to achieve state-of-the-art performances for a frequency reference. Their measurements and insight set the stage for building a high phase-space density beam machine and performing NICE-OHMS on the beam. The construction of this beam machine is detailed in chapters 5 and 6.

To support the design of the beam machine, this chapter will explore the saturated feature in phase rather than absorption (because NICE-OHMS is sensitive to the phase). Finding literature that looked into the saturated feature in phase space on a cold beam and a high-finesse linear cavity was tricky, so we carried out simulations of the saturated feature and its dependence on

cavity input power, velocity offset along cavity axis, beam axial temperature dependence, and atomic beam propagation velocity. Additionally, the authors in [47, 49] claim that spectroscopy techniques that utilize phase measurements are affected much less than direct absorption measurements, and they coin the term *saturation-insensitive* detection. This conclusion further motivates the need for an optical Bloch equation model to capture the full picture.

Importantly, cavity-enhanced saturated spectroscopy measurements detailed in this chapter and in [59] and [51] are in the low collective cooperativity regime, where atom-cavity coherences are not strong enough to be expressed. This is in contrast to chapters 7 and 8, which investigate saturation-induced features in a high collective cooperativity regime.

4.1 Phase Shift from Atoms in a Cavity

In the case of a phase-sensitive measurement scheme like NICE-OHMS, we start by finding the analytical description for the phase shift of atoms in a cavity. The phase-shift by a two-level atom ϕ_{at} probed by a laser at frequency ω detuned from atomic resonance by $\Delta_a = \omega - \omega_a$ is:

$$\phi_{at}(\Delta_a, N) = N \frac{3\lambda^2}{2\pi} \frac{\Delta_a/\gamma}{1 + s_0 + 4\Delta_a^2/\gamma^2} \quad (4.1)$$

Where N is the total number of atoms interacting with the laser beam assuming a top-hat distribution, λ is the transition wavelength, γ is the natural lifetime of the transition, and s_0 is the saturation parameter. The saturation parameter is defined as the ratio between the laser intensity and the saturation intensity:

$$s_0 = \frac{I}{I_{sat}} \quad (4.2)$$

The phase shift is convoluted with the velocity distribution of atoms $\rho(v_x, \Gamma_D)$ by:

$$\phi_D(\Gamma_D, N) = \int_{-\infty}^{\infty} \phi_{at}(\Delta_a - kv_x, N) \rho(v_x, \Gamma_D) dv_x \quad (4.3)$$

Here Γ_D is the Doppler width or the Gaussian full-width at half-max. We take the direction x to be along the cavity axis and z to be perpendicular

to the cavity axis. The signal strength S_1 for NICE-OHMS with the carrier resonant to the atomic transition is finally [15]:

$$S_1 \propto \frac{2F}{\pi} (\phi_{D,forw} - \phi_{D,back}) \quad (4.4)$$

The accumulated phase by the light field in the cavity going forwards $\phi_{D,forw}$ and backwards $\phi_{D,back}$ can be assumed to be identical in the case of a linear cavity with identical mirrors and center-of-mass velocity at zero relative to the cavity. However, we consider what happens when the cloud has a velocity offset relative to the cavity in section 4.2.2. We only plot the phase and omit J_0 and J_1 for simplicity.

This set of equations gives us the basis to understand the simulations to come and calculate an anticipated signal size for the beam experiment using NICE-OHMS. Crucially, these equations do not include the physics for a saturated feature, which is included in the numerical model explained next.

4.2 Simulations vs Analytical Spectroscopy on a Beam

We were motivated to investigate the saturated feature alongside the analytic model above with a more rigorous numerical method to identify effects that are not captured in the analytical model, such as Dopplerons [60, 61] and divergence from the Kramers-Kronig relation [47]. Fortunately, our colleague Mikkel Tang has a numerical solver for the full Jaynes-Cummings model using a second-order Runge-Kutter integrator. The reader can find further details of the numerical solver in his PhD thesis [62] and [63, 64], but in brief, it simulates step-wise in time the motional and internal degrees of freedom of *super-atoms*¹ in an atomic beam traveling through a standing wave of a cavity and includes laser forces. These simulations are as close as one can get before making real measurements.

The parameter space is large, and we are limited by the time it takes for the simulation to converge, which could be several hours for large Rabi frequencies and large atom numbers. We started with simulating parameters based on the experiment detailed in chapter 5 and searched outwards in parameter space to explore different regimes and scaling.

¹Atoms are clustered into super-atoms comprising of 100 to speed up simulations.

Using the parameters for the beam machine (see table C.1) and a cavity input power of 1 nW, we find the spectrum plotted in figure 4.1, with points representing the solutions to the numerical solver. A line representing the classical phase described in the previous section is included, and the atom number required to match the data is only increased by 10% which is reasonable considering the models handle the physics with completely different complexity, i.e., a Monte-Carlo simulation using the Jaynes Cummings model vs a simple analytical approach using convolutions.

The full CQED model reveals the saturated feature, which is seen as a narrow dispersive feature with a steeper slope than that corresponding to the broad envelope. We introduce a phenomenological phase representing the saturated feature ϕ_{sat} with an opposite phase to the Doppler envelope, and that only arises from a subgroup of atoms near resonance to parameterize the saturated feature, namely:

$$\phi = \frac{2F}{\pi} (\phi_D - \phi_{\text{sat}}) \quad (4.5)$$

$$\phi = \frac{2F}{\pi} (\phi_D(\Gamma_D, N) - \phi_D(\alpha_D \Gamma_D, \alpha_N N)) \quad (4.6)$$

Here, α_D is a factor < 1 that is a factor of the Doppler width, and α_N is a factor < 1 that is a factor of the atom number.

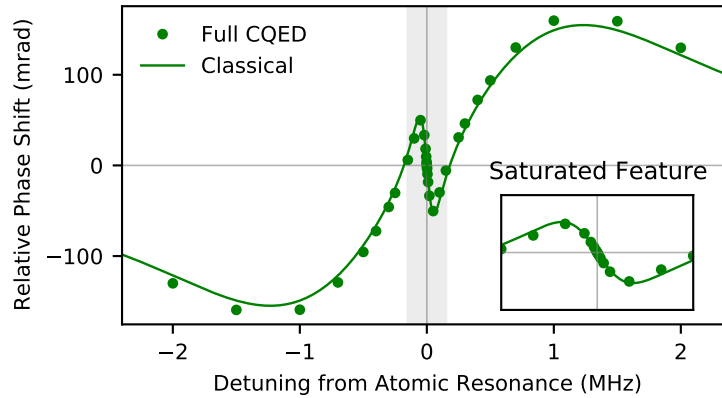


Figure 4.1: **Phase Spectrum with Saturated Feature.** Simulated phase shift showing the central Lamb-dip. The line is the anticipated analytical phase shift for a Doppler-broadened atomic beam transiting a cavity.

The dominant broadening for the central peak is power broadening $\Gamma_P = \gamma\sqrt{1 + s_0}$, and we investigate this in figure 4.2. Increasing the power changes the peak-to-peak height and width of the saturated feature, shown on the left-hand column of plots. As shown on the top right of figure 4.2, the rescaling factors used to fit the saturated feature follow a relationship of approximately $\alpha_D = \alpha_N = \Gamma_P/2\Gamma_D$ which is the ratio of the power-broadened linewidth and the Doppler linewidth, with an extra factor of 1/2. This ratio comes from the overlap of saturated atoms compared to the total atom number, and increasing the power addresses atoms with larger Doppler shifts. Until $\alpha \approx 1$, the incline slows due to the power broadening matching the Doppler width.

The balance between the height and width of the saturated feature defines the gradient $\delta\phi/\delta\nu$ at resonance, and this gradient links directly to the achievable shot-noise-limited linewidth. The linewidth for 1 s integration time derived specifically for NICE-OHMS from the Sharlow-Townes in [19] is:

$$\Delta v_{\text{SNL}} = \frac{\pi}{2\eta\frac{P_{\text{in}}}{h\nu}\left(\frac{\delta\phi}{\delta\nu}\right)^2} \quad (4.7)$$

Here, P_{in} is the input power. The relation of gradient to power is not linear, meaning the smallest feature width is not necessarily resulting in the sharpest gradient, and this relationship with power is shown in the bottom right of figure 4.2. The steepest gradient is found to be at 1 nW input power; however, the best shot-noise-limited linewidth is at 10 nW. For increasing power, the gradient suffers as the saturated feature flattens, and beyond 30 nW, the Doppler envelope would have a steeper slope if not for the saturated feature. This inspires the question: is the saturated feature a hindrance in some cases, and can we find a regime that still utilizes the cavity phase enhancement of $2F/\pi$ while also finding a way to destroy the saturated feature? It's worth noting that in this ideal scenario, the velocity distribution is perfectly centered around zero-resonance but in reality is might have a bias, especially in a beam scenario. The main benefit of the saturated feature is that it will remain fixed to zero even if the velocity distribution has a bias; see the later section 4.3, hence the name Doppler-free.

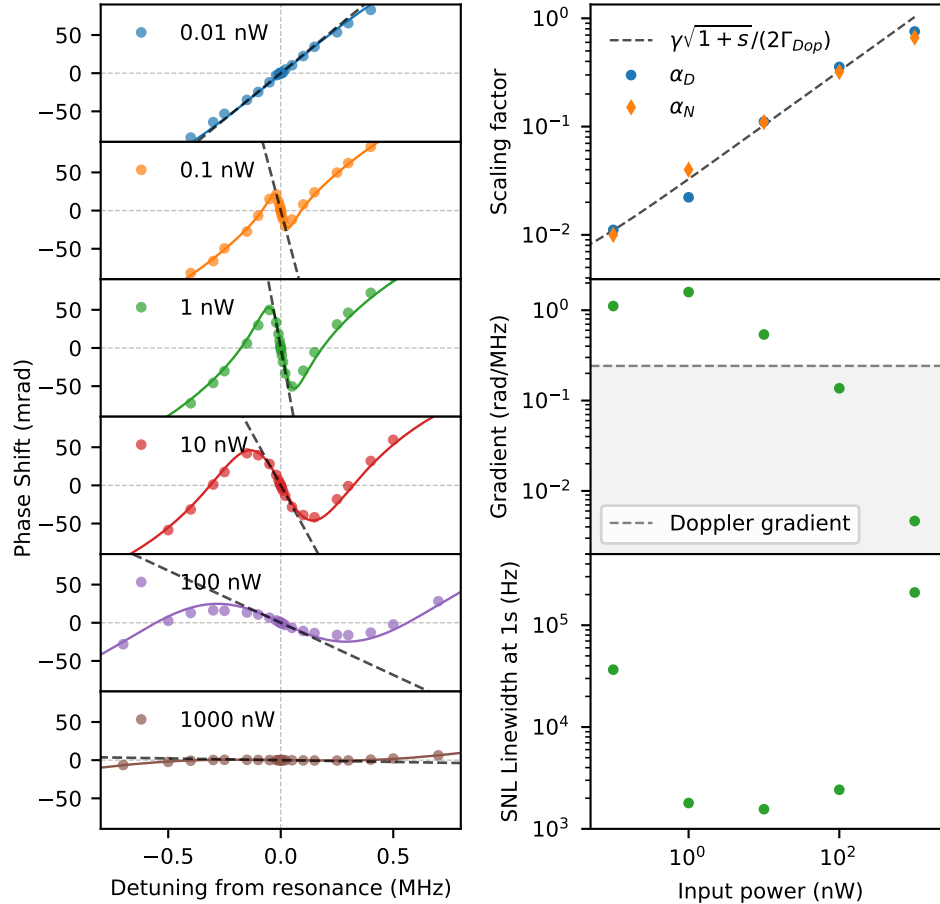


Figure 4.2: **Saturated Feature versus Power.** Left is the simulated phase with varying power, represented by dots, smooth line representing a fit, and dark dashed line representing the extracted gradient. The top right shows the scaling factors for the fits, along with a proposed model with the dashed line. The middle right shows the gradient plotted versus input power and a horizontal line represents the gradient from the Doppler envelope. The sign of the gradient is neglected. The bottom right shows the equivalent shot-noise limited linewidth for a 1 s integration time.

4.2.1 Temperature dependence

So far, the dominant broadening mechanism has been Doppler, and additional laser cooling to reduce the Doppler width means more atoms are in a narrower spectral range. The simulations in figure 4.3 shows a series of reasonably achievable atomic temperatures from 4 mK to 4 μ K that might be achieved by molasses cooling on the 7.5 kHz wide $^1S_0 \rightarrow ^3P_1$ that has a Doppler limit $< 1 \mu$ K. Note that only the temperature in 1D along the cavity axis is important for the Doppler broadening in the phase spectrum. The optical molasses cooling only needs to be implemented along the same axis as the cavity axis. Cooling along the other two axes would increase the atom number density by slowing or collimating the beam.

Figure 4.3 shows the phase spectrum at 4 mK, and for lower temperatures, the peak-to-peak phase on the Doppler envelope increases because of more atoms closer to the resonance frequency. Although the gradient of the saturated feature improves at first for 0.4 mK, it declines for 0.04 mK. It completely vanishes for 4 μ K because now the Doppler linewidth is on the same order as the power broadening linewidth.

As identified in the previous section, the power broadening from the probe must be less than the Doppler broadening to resolve a saturated feature. This is an interesting line of reasoning that leads naturally on to the later sections where we investigate how a collective phenomenon introduces a different kind of saturated feature for large atom number and low atomic temperatures (the strong collective cooperativity regime) in chapter 7, and experimentally tested in chapter 8.

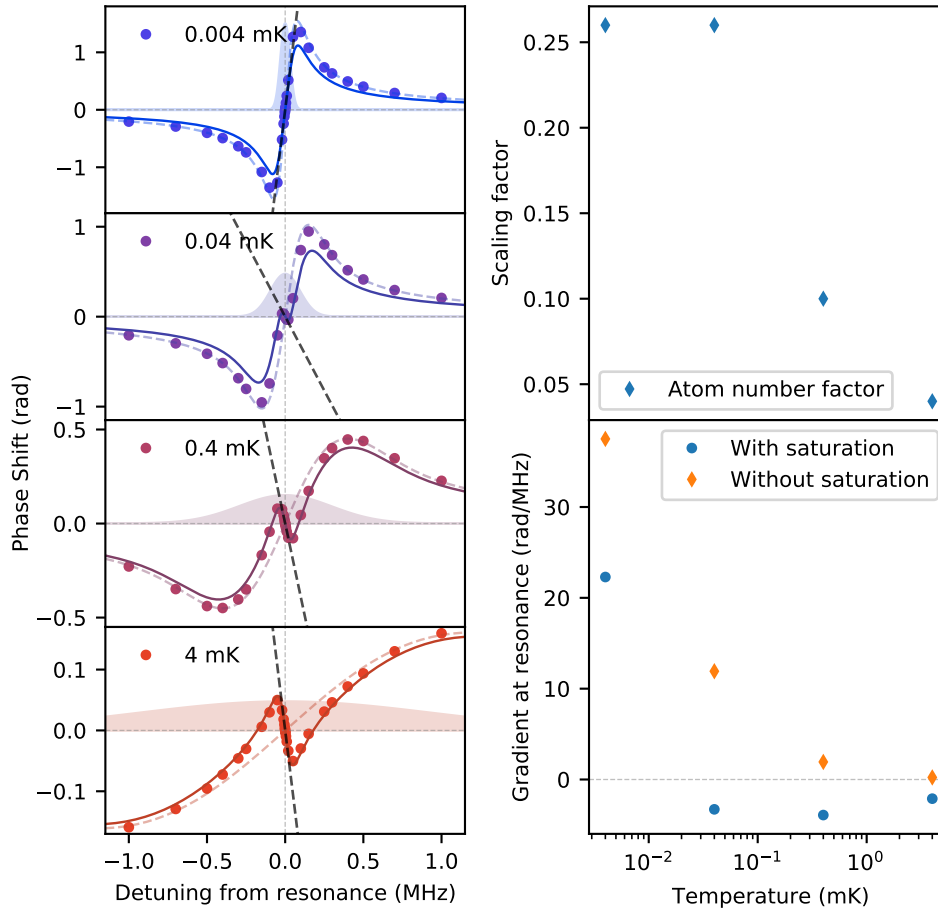


Figure 4.3: **Saturated Feature versus Temperature.** Left is the simulated phase with varying temperatures represented by dots. The smooth line represents a fit using the analytical model, and the dashed line represents a fit without considering the saturated feature. The background shaded region shows the Doppler distribution of atoms where the height is arbitrary but the number of atoms (or the area beneath the Gaussian profile) remains constant between all graphs. The top right shows the fitting atom number factor, and the bottom right shows the extract gradient.

4.2.2 Velocity Bias Along Cavity Axis Dependence

A unique situation for interrogation on a slow atomic beam is that a mismatched pointing vector of the atomic beam could accumulate a significant velocity bias relative to the cavity axis. For example, a beam propagating at $25 \text{ m} \cdot \text{s}^{-1}$ with a 2.2° angle off-perpendicular relative to the cavity axis corresponds to a velocity bias of $1 \text{ m} \cdot \text{s}^{-1}$. On the scale of the perpendicular beam temperature on the order of mK, this can be a significant velocity offset, and hence Doppler shift offset. We experimentally investigate the tuning of an atomic beam propagation angle in section 6.2. Gravity on an atomic beam travelling at $25 \text{ m} \cdot \text{s}^{-1}$ over 15 cm only gains $0.5 \text{ cm} \cdot \text{s}^{-1}$, so negligible compared to an improperly deflected beam.

The results of a velocity bias are illustrated in figure 4.4. For increasing velocity offsets, the saturated feature slowly vanishes until the velocity offset is so large there are no atoms close to rest, which is also reflected in the atom number fitting parameter which follows a clear Gaussian falling to zero for large velocity offset. Optimizing the beam angle to make the phase spectrum symmetrical could be a robust method of aligning the beam perfectly perpendicular to the cavity axis. For example, for a hot-beam superradiant laser [65], it is necessary to avoid an atom intersecting several cavity anti-nodes during its cavity transit, i.e., $\langle v_x \rangle$ must be as close to zero as possible.

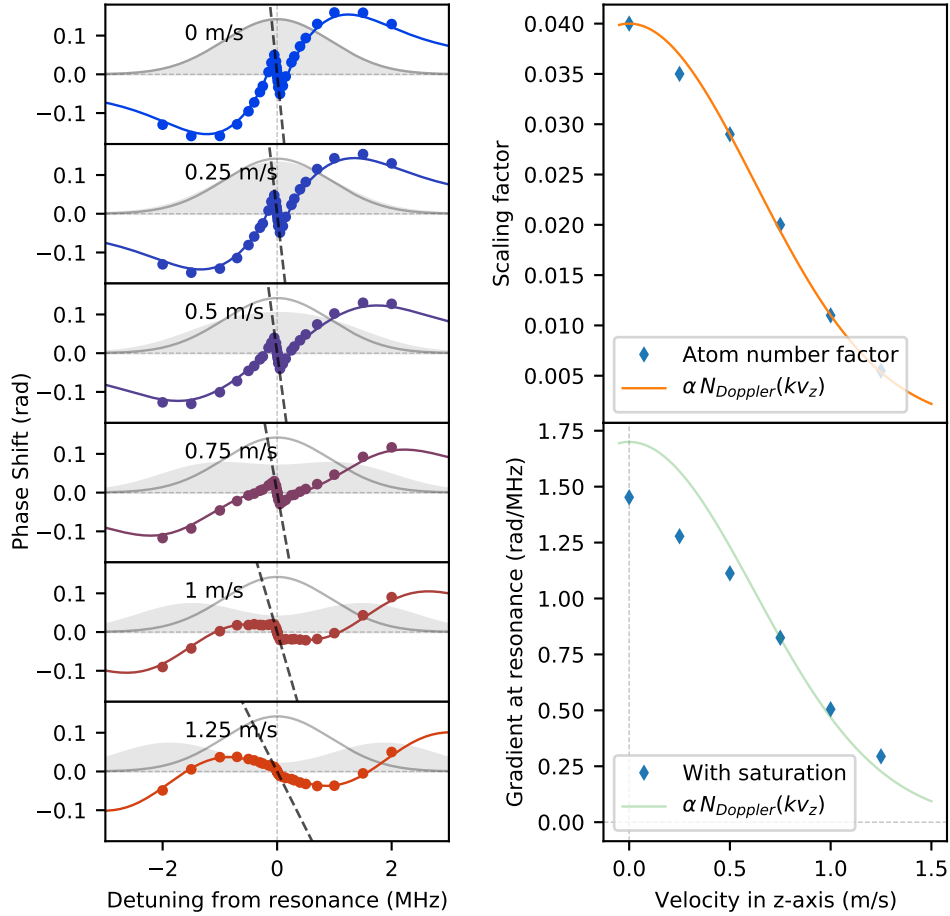


Figure 4.4: **Phase Spectrum vs Velocity Bias.** Left shows the phase-spectrum for the same atomic beam that is offset with increasing velocities indicated in the legend. The shaded Gaussians represent the Doppler detuning of the atoms with increasing offset, and the outline of the $0 \text{ m} \cdot \text{s}^{-1}$ velocity offset remains for comparison in all panels. Right shows the atom number scaling factor follows a Gaussian perfectly with an arbitrary scaling factor, as does the gradient.

4.2.3 Transit Broadening Dependence

An important degree of freedom for an atomic beam is the effect of the transit time on the saturated feature. We simulate a beam of constant instantaneous atom number in the cavity volume for various transit velocities. Doubling the beam speed also requires the flux to be doubled. For this simulation, we keep the Doppler detuning but deactivate motion so that for low transit velocities like $12 \text{ m} \cdot \text{s}^{-1}$, the atomic beam divergence does not cause a drop in cavity atom number. This should allow effects only due to transit time to be reliably expressed, and the phase-spectrums are plotted in figure 4.5.

For increasing transit velocity v_z , the saturated feature gradually vanishes. The transit time broadening Γ_t is the rate at which atoms enter and leave the cavity, which we define as:

$$\Gamma_t = \frac{v_z}{2w_0} \quad (4.8)$$

The saturation feature starts to vanish when Γ_t reaches the same as the on-resonance Rabi-frequency. An atom entering the cavity does not have time to reach saturation before it exits, so the saturation feature does not exist [66].

The effect of transit broadening is likely the cause of the signal vanishing for powers = 0.1 and 0.01 nW in the first simulation in this section, figure 4.2. At these power levels, even the transit broadening for $20 \text{ m} \cdot \text{s}^{-1}$ is on the same scale as the Rabi frequency.

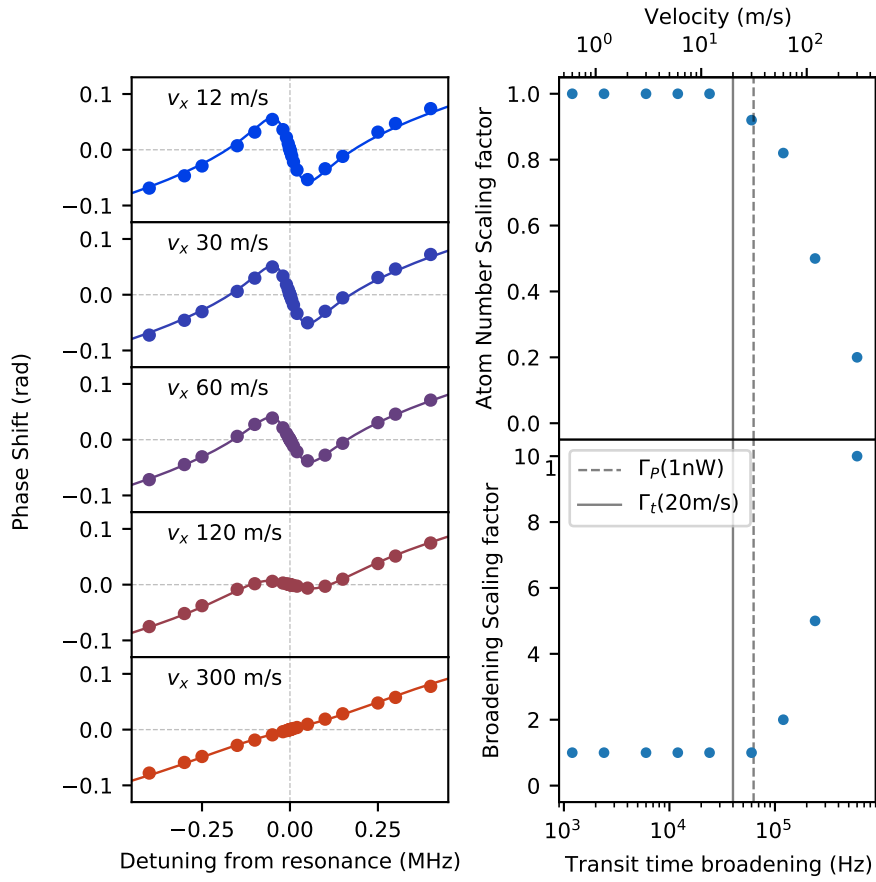


Figure 4.5: **Phase Spectrum vs Transit Time.** The transit velocity is gradually increased, and the phase spectrum is plotted with the analytical fit. Right shows the fit parameters plotted on two different x-axis that are shared by the top axis in velocity, and the bottom axis is in the corresponding transit broadening in units of Hz.

4.3 Conclusion

The simulations of the atomic beam through an optical cavity in the low cooperativity regime successfully showed that the saturation feature can be described with considerations of effective atoms and effective broadening represented by fitting parameters α_N and α_D . The primary features are well understood, and no significant deviations have been observed. However, we still lack a general equation for the size of the saturated feature, a topic of future work.

In selecting the optimal parameters for the error signal resulting in the most narrow laser linewidth, several bounds on the probing power must be considered and navigated to optimize the signal, given available resources of atom flux and achievable cavity parameters. Primarily, the power broadening must be large enough to overcome the transit broadening $\Gamma_P > \Gamma_t$, and it must be smaller than the Doppler width $\Gamma_P < \Gamma_D$.

Chapter 5

The Strontium Beam Machine Construction

We plan to demonstrate dead-time free frequency measurement with NICE-OHMS on an optical transition, which is not limited by Dick noise. We aim to realize a continuous and high flux source of neutral strontium-88 that is cooled and compressed into a region protected from direct stray blue-light for interrogation with an optical cavity on the 7.5 kHz inter-combination transition $^1S_0 \rightarrow ^3P_1$ at 689 nm.

Our method of implementation is as follows. A continuous beam of ^{88}Sr emerges from a Zeeman slower with a longitudinal speed of approximately $30 \text{ m} \cdot \text{s}^{-1}$ and enters a 45° angled 1D MOT region. The MOT will cool and compress the atomic beam transversely and deflect the atomic beam into a cavity region protected from stray cooling light, reducing the AC Stark shifts on the 1S_0 and 3P_1 states. The primary concern is the intense light from the Zeeman slower with roughly 70 mW, and the secondary concern is the large amount of scattered light in the deflection chamber. The atomic beam is sent to overlap with the mode volume of a linear cavity in a smaller chamber, which is 15 cm away from the Zeeman slower and deflection MOT, and with no line-of-sight to the Zeeman vacuum viewport, which scatters a lot of light.

The author would strongly recommend the thesis of Shayne Bennetts [67] as a useful source for designing and building any strontium AMO experiment.

The experiment has had an unfortunate history. The original design implemented a 20° MOT deflection angle which was very compact and ideal for higher atom fluxes and velocities. The previous version of the experiment has

an oven lid design with capillary tubes [68], which is a frequently used design for achieving a higher density and collimated atomic beam compared to just a hole in a lid. However, we suspected the oven lid was leaking strontium from undesired locations like sealing edges and screw points, which we could verify with blue fluorescence imaging at the cavity nozzle, see absorption image in appendix A. If a significant portion of the flux was going in the wrong direction, we feared this would impact the useful flux into the spectroscopy part of the experiment. These problems were further exaggerated by how compact the deflection chamber was, making it tough to measure the flux because of the large amounts of stray light. Finally, the cavity mirrors were coated with reflectivity that was too high that the manufacturers themselves could not measure it. After a significant effort was made to couple light into the cavity, we suspected the mirror losses were dominant and that coupling power into the cavity was impossible even outside vacuum. These problems and other reasons motivated us to order new cavity mirrors with coatings that could be verified by the manufacturer. We changed the deflection chamber to a much larger octagon (Kimball Physics) vacuum chamber with DN160 windows for far more optical access to better test and understand how to deflect atoms with a MOT. Fortunately, we had one of these chambers spare. We changed the oven lid to a simpler 1.5 mm diameter hole so we could guarantee atoms were traveling through the experiment, but at the expense of atom collimation towards the experiment and, therefore, faster oven depletion. We put in roughly 10 g, and we anticipate plenty of experimental operation time before the strontium is depleted. We removed the 5 mm diameter copper differential pumping tube just after the oven which makes alignment of the oven and Zeeman slower laser easier, at the expense of worse vacuum pressures at the deflection chamber and cavity chamber. However, since the lifetime of a single atom in a beam experiment is very short before it hits a wall, we are less sensitive to background gas collisions impacting the experiment, so we can operate at higher pressures without penalties. We also suspected we would gain more from oven molasses cooling because the collimated atomic beam can have a three times larger diameter. We upgraded the two 461 nm cooling lasers of around 100 mW to three high-power Nichia diode lasers with > 500 mW free running output power. This meant that we had far more available power for probing and laser cooling, and we could test out extra optical molasses at the oven and a second cooling axis on the 1D MOT. Finally we also ordered a gate valve so vacuum operations would not oxidize the strontium in the oven.

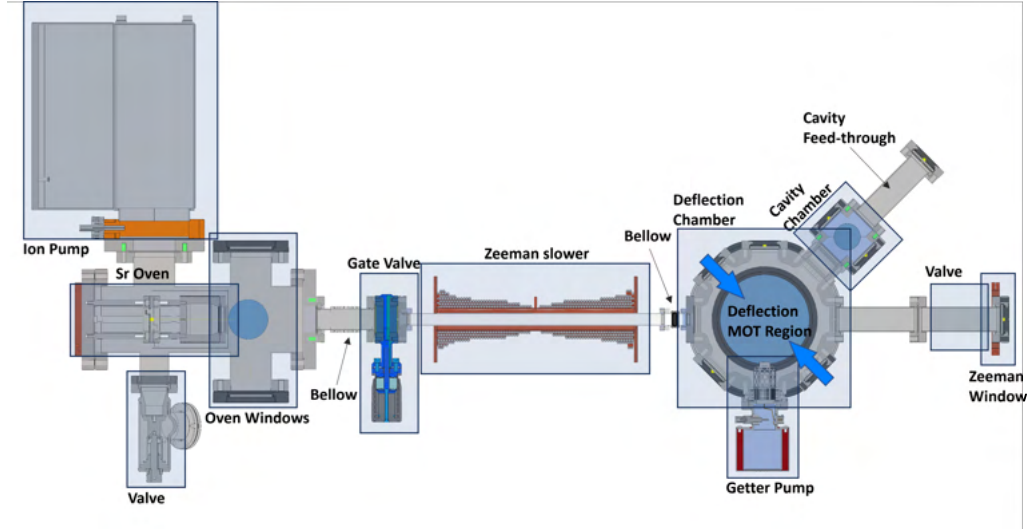


Figure 5.1: **Cross-section of Strontium Beam Machine from Top-Down.** Description of apparatus in the text. The direction of gravity aligned into the page. The optical cavity and magnetic coils around the deflection chamber are omitted for simplicity; details are given figure 5.5

On February 17, 2022, the experiment table was completely cleared, and we restarted the building of the experiment with the changes mentioned above.

5.1 Overview

The strontium beam starts from the oven chamber. 10 grams of strontium are loaded into the oven, and twisted-pair heating wire is wrapped around the oven body. A thermocouple is secured to the oven body to monitor the temperature. A DN40 lid with a 1.5 mm diameter hole in the centre is screwed onto the oven and sealed with a nickel-plated copper gasket. One layer of heat shielding surrounds the oven. Steel rods mount the oven 7.4 cm away from the DN100 plate, to further minimize heat flow. The oven chamber is attached to an all-metal right-angle valve for roughing and turbo pumping, and a large volume ion pump.

The oven windows in a 4-way cross in $x - y$ plane are used to probe the flux coming from the oven nozzle, and for molasses cooling to enhance the

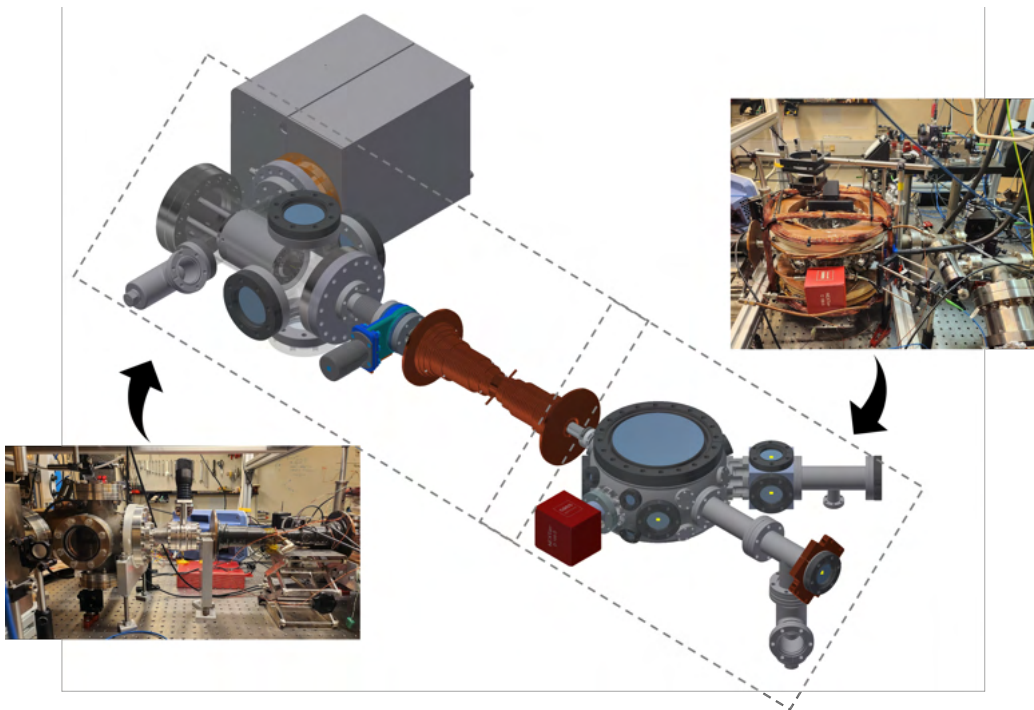


Figure 5.2: CAD Drawing Oblique Angle.

flux reaching the deflection chamber by collimating the atomic beam. The large divergence of the atomic beam coats about 50% of the windows, but there is still sufficient optical access close to the oven nozzle.

The oven chamber is attached to the Zeeman slower by a DN40 bellow for stress relief and flexibility in alignment, followed by a gate valve that can separate the oven chamber to the deflection and cavity region. The gate valve allows high vacuum to be maintained on one side of the gate, while the other side is exposed to atmospheric pressure. This means operations can be made separately on either side of the gate, for example, refilling the oven with strontium while avoiding having to pump down and bake out the deflection and cavity chambers.

The Zeeman slower is a copper wire wrapped around a 40 cm long DN16 tube. The tube is attached to the chamber by a DN16 bellow onto the west flange of the octagon deflection chamber. The Kimball Physics deflection chamber has 8 DN40 flanges, 16 DN16 flanges, and 2 DN160 flanges. A NEX Torr ion pump is directly attached to the south flange. The getter cartridge just barely intersects with the optical access of DN160 viewport, and the magnetic field from the pump is negligible at the deflection region. The east flange is attached to a DN40 tube for sufficient clearance for the right-angle valve and capped by a viewport for the Zeeman slower laser. The 6-cross DN40 cube cavity chamber is attached with a Kimball Physics shallow adaptor to the north-east flange, and this is where the optical cavity is placed, and the atomic beam will deflect into. A DN40 T-tube is attached to the exit of the cavity chamber, and the cavity piezo control wires are fed through a DN16 flange.

North, south-east, south-west and north-west are capped with DN40 viewports and the deflection MOT beams are sent through south-east and north-west viewports, indicated by bold blue arrows. Finally the big DN160 viewports seal the top and bottom with great optical access to the beam. These viewports were given custom anti-reflection coating.

5.1.1 Vacuum part cleaning

There is plenty of advice on how to clean vacuum components for UHV. The key message is to focus on avoiding oils/hydrocarbons on internal surfaces or crevices because these will get thinly distributed around the experiment during a bake out and are very harmful to high reflectivity mirrors, impacting the finesse and transmission efficiency drastically.

We cleaned all internal surfaces first with 99.9% acetone, followed by 99.9% ethanol, taking lint-free wipes and q-tips to attack hard-to-reach regions where the most dirt often hides. Use powder-free gloves and avoid touching your face or other surfaces while cleaning. Smaller vacuum parts were placed into an ultra-sonic bath of acetone. Take care not to damage the knife edge while cleaning or handling vacuum parts. Use kitchen aluminium foil to place over table surfaces and cover flanges with foil to protect knife edges and avoid dust/dirt falling in post-cleaning.

5.1.2 Bake out

Once cleaned and partially/fully assembled, a global uniform heating (baking) of the entire vacuum chamber is necessary for reaching low vacuum pressures. There is plenty of advice on baking out an experiment, and the duration and temperature of the bake depend on your target pressure. The main goal is to keep the bake-out uniform with slow increases in temperature to avoid large temperature gradients around sensitive parts like windows. Keep regions with parts that are sensitive to dirt at a higher temperature so any dirt will deposit at colder regions. Baking the experiment above 120 C for up to a week is sufficient for removing water vapor deposited into the internal surfaces of the vacuum chamber. Higher back-out temperatures decrease the pumping time but threaten damaging heat-sensitive components like piezos and viewport windows.

5.2 Strontium Oven

The oven is a heating wire coiled around a crucible filled with strontium, with a 1.5 mm diameter hole on the lid that connects with a DN40 flange. The gasket is made of nickel-plated copper because strontium can reduce the melting point of copper and cause the seal achieved by the gasket to fail and the oven lid to leak. The oven is surrounded by a heat shield, allowing the centre to get hotter and stopping radiation from reaching the chamber walls. For a while, there was water cooling around the vacuum chamber housing the oven during operation, but eventually we stopped using it because the housing was only reaching 50 C which is still hot to touch but not hot enough to burn or boil anything. The typical oven operation temperature is around 515 C.

5.2.1 Characterization and Fit

To characterize the divergence of the beam from the oven, we perform simple laser absorption spectroscopy using linearly polarized light at 461 nm corresponding to the $^1S_0 \rightarrow ^1P_1$ transition of strontium. A laser beam from an ECDL was aligned parallel and 2 cm away to the oven lid surface and centred to the oven lid hole by eye. The ECDL was then frequency-tuned over 4 GHz while the transmission was monitored on a photodiode. During the frequency tuning, a second photodiode monitors the difference in power and is used to remove any background power fluctuations. See the result in figure 5.3.

A Gaussian profile is fit to the data, and it clearly does not fully describe the lineshape, which is actually more peaked than a cloud of atoms in thermal equilibrium. This sharper peak is a consequence of the atoms traveling in a beam with the average velocity being in a specific direction. We take the full-width half-max = 0.781(4) GHz and use it to estimate a velocity of $\Delta v_{\text{beam-axis}}$ 736 m · s⁻¹, so 318 m · s⁻¹ either direction. Further reading with details about analytical models for the beam shape from an oven nozzle was explored by Staub et al. [69].

5.3 Magnetic Coils

Several magnetic coils are required in the experiment, and their design considerations are explained, and magnetic fields were mapped here.

5.3.1 Zeeman Coil

The Zeeman slower coil was built before 2020 [70] by coiling a copper wire around a DN16 tube and secured in place with heat-resistant epoxy. Piping runs along the coil to remove heat with water cooling, but we did not need this because it did not get that hot at operating temperatures. It utilizes a balanced design where the magnetic 0-field is in the centre of the coil, the magnetic field profile is shown in figure 5.4. The length from DN16-to-DN16 flange was 40 cm.

5.3.2 Coils at Angled MOT

Figure 5.5 illustrates the coil configuration around the deflection chamber.

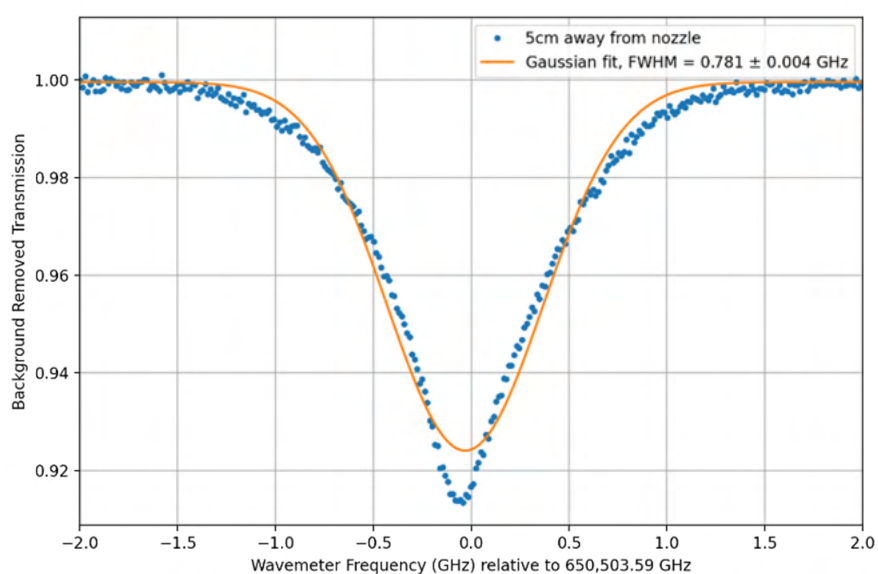


Figure 5.3: **Absorption Spectroscopy at Oven Lid.** The transmission dip for free scanning a Toptica 461 nm ECDL around $^{88}\text{Sr } ^1\text{S}_0 \rightarrow ^1\text{P}_1$ transition. The frequency axis is reconstructed from a high-finesse 7S wavemeter. The slight mismatch of the peak on resonance could be a small angle relative to the beam axis and the oven lid. A Gaussian fit is made and the FWHM is extracted.

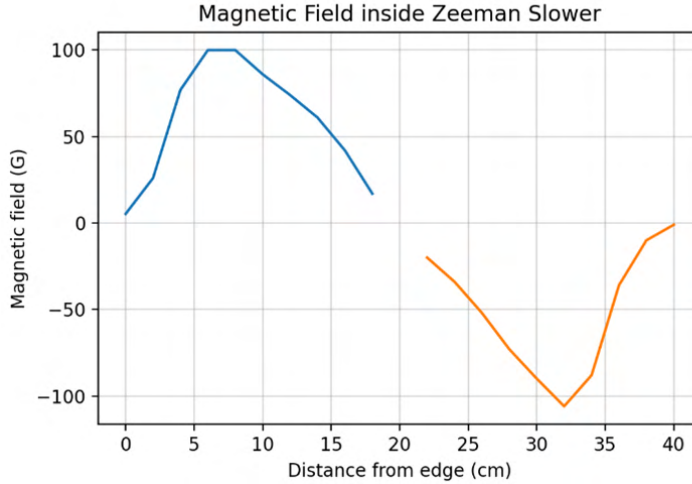


Figure 5.4: **Zeeman Coil Magnetic Field.** Magnetic field magnitude along the atomic propagation axis with the coil driven at 7 A at 1.00 V. The gaussmeter probe is about 18 cm long, hence the gap in data at the center.

The deflection-MOT (hereon called 1D MOT) coils are a pair of reused coils from the Sr1 experiment. They were removed from Sr1 and replaced by a design that did not incorporate a metal holder to avoid high inductances that would resist the action of quickly switching on and off the coils, which is required for the operation of a red MOT cooling stage. Since the beam experiment does not need to rapidly switch the coils, these were perfect because they already fit the Kimball chamber geometry with the anti-Helmholtz configuration. After the problems experienced by the Sr1 team, we were also reluctant to build a new pair, given the troubles they had, when there was a perfectly functional pair already available.

We drive this anti-Helmholtz coil pair in series with a single power supply, which would be sufficient to achieve the necessary magnetic field gradients as anticipated by simulations of about $20 \text{ G} \cdot \text{cm}^{-1}$. The magnetic field was mapped out with a Gaussmeter by measuring the magnetic field magnitude along the coil axis for each point on an 8x8 grid placed in the center of the coil, see Figure 5.6. The average magnetic field magnitude is used to estimate the coil turns to be 94, and a gradient of $8.9 \text{ G} \cdot \text{cm}^{-1}$ in the anti-Helmholtz configuration, driven with 10 A, so $0.89 \text{ G} \cdot \text{cm}^{-1} \cdot \text{A}^{-1}$. The diameter of the coil is 23.0 cm, the length is 3.5 cm and the spacing of the coil pair is approx-

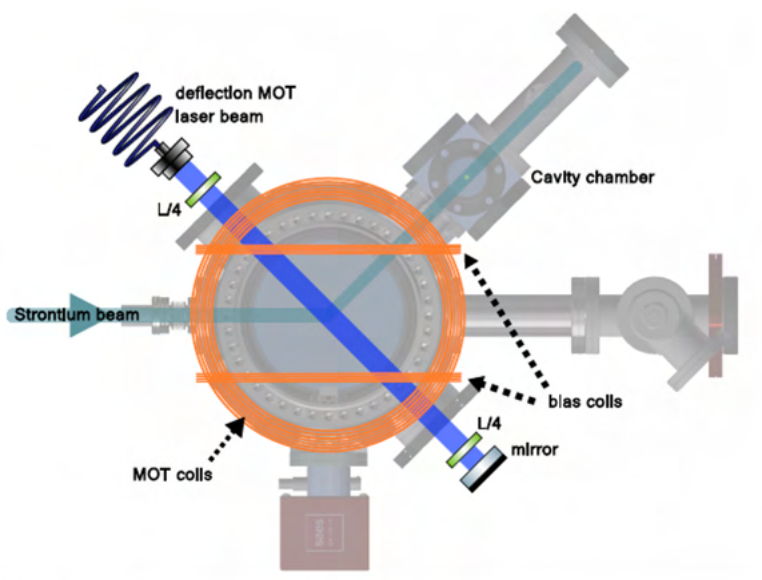


Figure 5.5: **Magnetic Coils and Optics.** Pictured is the deflection chamber from figure 5.1 now with the coils and optics. The MOT coils axis is parallel to the y-axis, and there is a pair of bias coils. A second pair of bias coils are aligned along the x-axis. A third pair of bias coils were not implemented due to having sufficient control of the atomic beam deflection and the geometry requiring winding around the chamber rather than pre-winding and mounting. Author: Johnathan Elsborg.

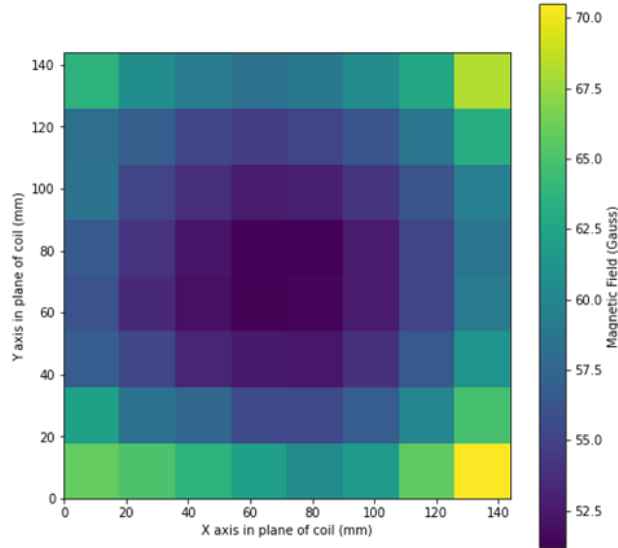


Figure 5.6: **Magnetic Field Magnitude of MOT Coil.** MOT coil is driven by 10 A at 2.22 V.

imately 12 cm.

5.3.3 Compensation coils

Since the 1D MOT coils are powered in series and so the magnetic field ratio from each coil is fixed, we would benefit from fine tuning the 0-field position with an extra two pairs of coils in Helmholtz configurations to compensate for any irregularities. We anticipated to need a $50 \text{ G} \cdot \text{cm}^{-1}$ field gradient along the 1D MOT, based on the magnitude required for Sr1 blue MOT. The compensation coils were designed and built by Jonathan Elsborg to provide a 0.5 cm shift in the position of the 0-field.

5.4 Lasers

The beam experiment requires several injected laser diodes to operate due to the lack of cheap and high-power sources of 461 nm. The laser diodes receive injection light from different sources via a polarization maintaining, single-mode optical fibers, and each laser diode and optics setup is mounted

WL (nm)	Name	Source	Stabilization Technique	Relative Det. (MHz)
461	Grandparent	Toptica DLPro ECDL	Modulation Transfer Spectroscopy	-120
461	Parent	Nichia Diode	IL to Grandparent laser	-520 -20 0
461	Zeeman	Nichia Diode	IL to Parent laser	-520
461	MOT	Nichia Diode	IL to Parent laser	-20
461	Molasses	Nichia Diode	IL to MOT laser	-20
689	Mausoleum	Moglabs ECDL	PDH lock to ULE Cavity	-42.1
689	Cavity	Ushio Diode	IL to Mausoleum laser	0
689	SWAP	Ushio Diode	IL to Cavity Laser	± 10

Table 5.1: **Laser Overview.** An overview of all operational lasers for the beam machine. The molasses and SWAP lasers were built and tested but not used for this work due to time or instability. IL: Injection Locked.

on its own breadboard. This modularity helps keep the optics grouped and a breadboard can be mounted anywhere it fits. As a trade-off, we may suffer from larger drifts because a thinner breadboard will be more prone to warping, especially if loaded in a strange way. The individual lasers are summarized in table 5.1. More details about the Mausoleum or clock laser can be found in the PhD thesis of Eliot Bohr [71].

The blue laser diodes can output enough power to classify them as a class IV laser, which means they are considered particularly harmful. Therefore, we have enclosed all these optical breadboards with black Thorlabs protective laser cardboard.

Schematics of each blue laser optical breadboards are shown in figure 5.7, and red optical breadboard in figure 5.8. The oven molasses board is not included because the laser was too inconsistent for stable use and must be rebuilt.

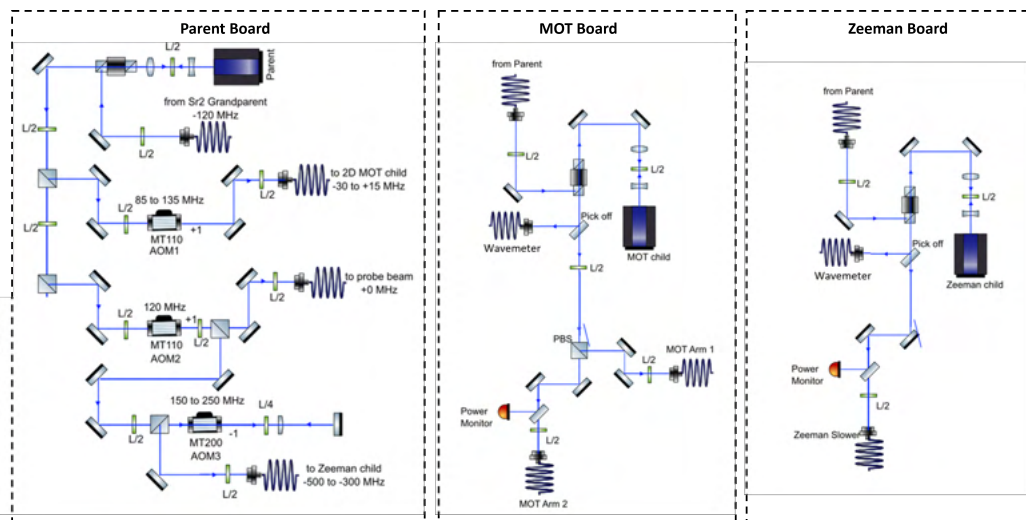


Figure 5.7: **Blue Laser Board Schematics.** The schematics mostly resembles the current state, some elements were removed and included. The Zeeman and MOT board were built with a lot of help from Jonathan Elsborg.

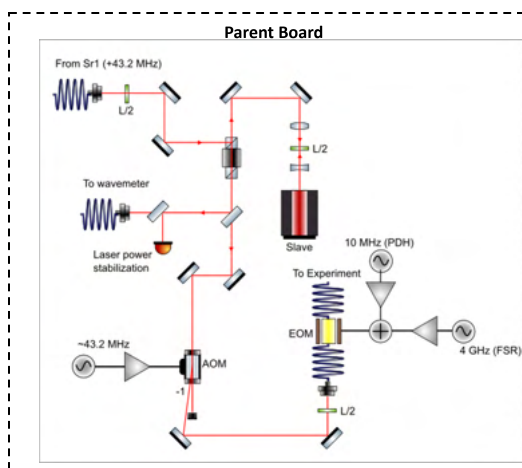


Figure 5.8: **Red Laser Board Schematics.** The red laser optical breadboard including the fibre coupled Jenoptik electro-optical modulator driven by two tones, one for Pound-Drever-Hall sidebands, and one for the NICE-OHMS sidebands. The breadboard was built entirely by Camila Beli Silva.

5.5 Optics

The laser light is delivered to the experiment through optical fibres into cage optics, which significantly simplifies the alignment process thanks to the pre-alignment offered by the cage optics. Each fibre injection and launch point act like a checkpoint for alignment. Using fibres result in homogeneous gaussian beams that maintain their shape for roughly 40 cm before the imperfection of the lens starts to become apparent. Building everything with fibre connections comes at the expense of optical power, due to poor coupling efficiencies ($< 50\%$) of the free-space mode shapes produced by the slaved laser diodes into the fibres. However, we have plenty of optical power to spare to compensate and achieve 70-80 mW of output power for the Zeeman slower, and 40 mW in both arms of the MOT.

The polarization maintaining fibres deliver light to a cage optic telescope to test out several beam sizes on the performance of the 1D MOT. Thorlab's cage optics is ideal for constructing a simple and configurable telescope because the optics can be translated along the laser propagation direction by translating the optic along 4 rods and then secured in place with screws. To help in the choice of the lenses for the telescope, a simple ray-tracing ABCD matrix calculation was made, and the design charts are shown in Figure 5.9. The telescope is built with a fibre source – lens 1 – lens 2 scheme, where lens 1 is 1 inch diameter diverging lens and lens 2 is 2 inch diameter converging lens. This configuration can achieve the most compact form.

We opted for a diverging lens of $f = -100$ mm and converging lens of $f = 100$ mm, that can achieve beam waist diameters between 20 – 40 mm with a total cage optic length of 120 – 170 mm.

We intended to attach the cage options to the vacuum chamber using a cage to a DN40 adaptor, but due to the geometry restrictions from the MOT coils, they would not fit. Instead, the cage options were mounted on the table, which on the plus side, gave more freedom in translating and angling the MOT beams. The MOT coil beam was retro-reflected by a 2 inch mirror and a 2 inch $\lambda/4$ waveplate is placed in front of the mirror to ensure the correct polarization for the MOT.

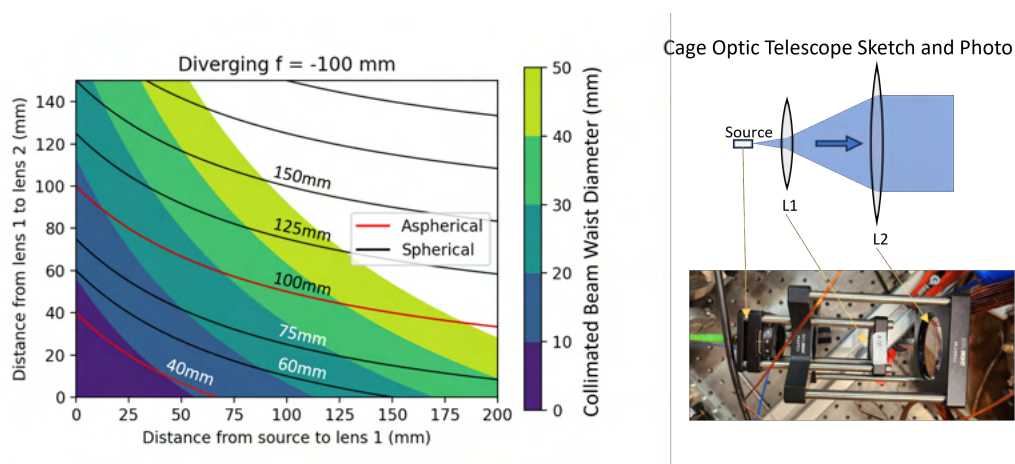


Figure 5.9: **MOT Beam Telescope Focal Length Design Charts.** The color bar indicates the waist diameter of the beam exiting the cage optic, given the collimation condition has been satisfied. The solid lines crossing through the colormap indicate the achievable beam diameters for a given converging lens with the indicated focal length. The red line means there is also both a regular and aspheric lens option available at Thorlabs. The right shows a sketch and photograph of the cage options.

Description	Equation
Cavity Waist Radius	$w_0 = \sqrt{\frac{\lambda}{2\pi} \sqrt{2r_{OC}\ell}}$
Cavity Transmission	$T = 1 - L - R$
Finesse	$F = \pi \frac{\sqrt{R}}{\sqrt{1-R}}$
Cavity Coupling Efficiency	$\eta_{\text{cav}} = \frac{T^2}{(1-R)^2}$
Round Trip Time	$t_{\text{rt}} = \frac{F\ell}{\pi c}$
Free Spectral Range	$\omega_{\text{FSR}} = \frac{2\pi}{t_{\text{rt}}}$
Spectral Linewidth	$\kappa = \frac{\omega_{\text{FSR}}}{F}$

Table 5.2: **Table of Cavity Equations.** w_0 : waist radius, λ : cavity resonant wavelength, r_{OC} : radius of curvature of each mirror assuming both have the same, ℓ : mirror spacing, R : cavity power reflection, T : cavity power transmission, L : cavity power losses due to scattering or absorption.

5.6 Spectroscopy Cavity

A fabry-perot optical cavity is made of two mirrors facing each other, separated by a distance. Designing, building, characterizing, and operating a high-finesse cavity for precision spectroscopy is complicated and nuanced and here we start with a series of important equations to aid in the design.

5.6.1 High Reflectivity Mirrors

Highly reflective coatings – while crucially also keeping optical losses low – are achieved by thin-film deposition of several alternating layers of dielectric material to create a Bragg mirror on a slightly concave silica glass window characterized by its radius of curvature r_{OC} . There is some uncertainty in the deposition process, so companies usually guarantee a lower bound for reflectivity. The key to the highest finesse cavities is using super-polished mirrors with roughness at the single Angstroms.

We were aiming for a finesse of 22,000, which meant a reflectivity of 99.986%. We approached three different companies, Laseroptik, Layertec, and FiveNine, and their individual price per mirror for the increasing number of mirrors can be seen in the graph below. FiveNine is known to be one of

the best and most reliable providers of mirror coatings, but this comes at a cost. We ended up choosing Layertec because they were the only company to offer characterization of the mirrors that they had coated for free, which no other company could offer – and they were the cheapest for a small batch.

Batches of mirrors are coated at a time, and we ordered eight mirrors but they could statistically only expect a yield of 80%. Luckily, all eight mirrors were within specification, allowing for four pairs of mirrors.

5.6.2 Hollow Zerodur Cavity Spacer

We had two ultra-low expansion Zerodur glass cylinders machined with access for optical and atomic beams; see 3D model and photographs in figure 5.10. The spacer is designed to be mounted with Viton O-ring that fits into the grooves around the top and bottom of the cavity spacer. The cavity with the O-rings is wedged into a DN40 tube and was originally designed to be lying down; however, we mounted it vertically because the optical access was more favourable.

5.6.3 Alignment Requirements

Larger radius of curvature mirrors are more difficult to align than smaller radius of curvature mirrors [72], and a quick assessment of the precision requirements in mirror angle and positioning was made to help design the cavity alignment set-up. The cavity axis is defined by the line that intersects the two focal points of each mirror; see figure 5.11.

$$\Delta y = f \frac{f \sin(\Delta\theta) + \Delta\ell}{\ell - f \cos(\Delta\theta) - f} \approx -\frac{f \Delta\theta + \Delta\ell}{2} \quad (5.1)$$

Where f is the focal length and also the r_{OC} , $\Delta\theta$ is the angle misalignment in radians, $\Delta\ell$ is the vertical mirror displacement. For small $\Delta\theta, \Delta\ell$ and $\ell \ll f$, it reduces to a simple equation. Plotting Δy for various displacements and angles reveals the diamond of successful alignment, shown in figure 5.12. $|\Delta y| < 3 \text{ mm}$ is defined by the aperture of the cavity spacer. The alignment precision of $< 1 \text{ mrad}$ can be achieved with Thorlabs mirror mounts and position alignment of $< 1 \text{ mm}$ is easily achieved by micro-translation stages.

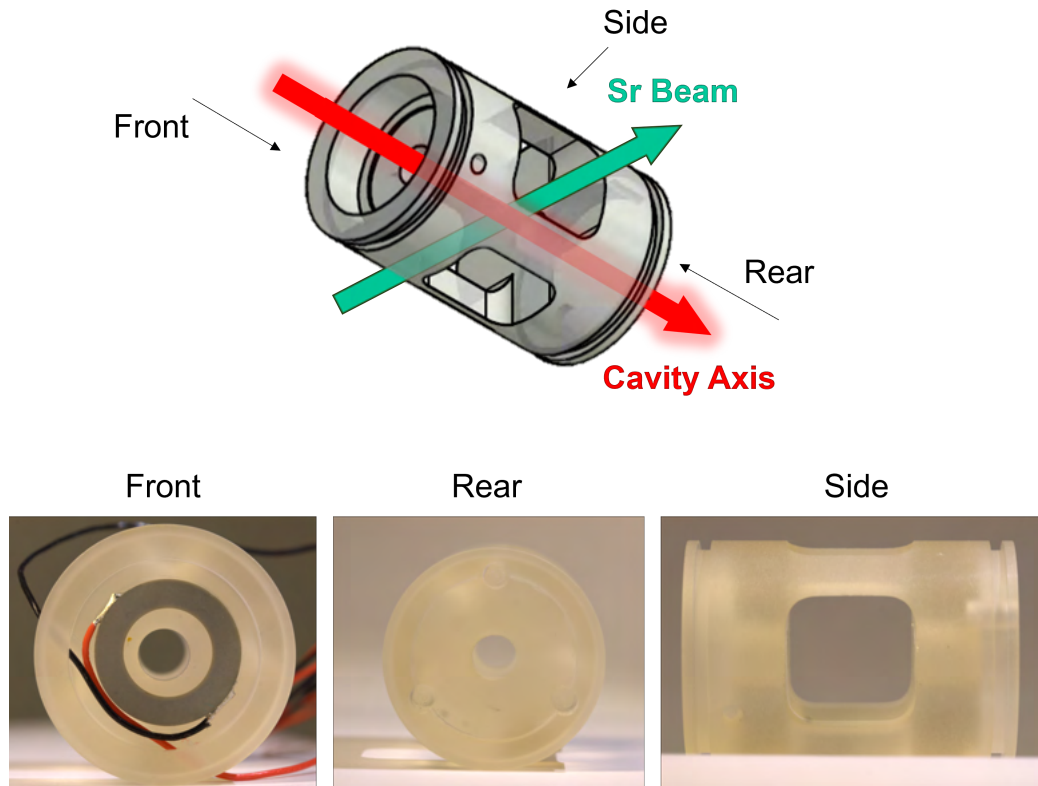


Figure 5.10: **Cavity Spacer Model and Photographs.** The photo shooting direction and side are indicated on the 3D model. The front photo shows an example piezo mounted in the cavity spacer, with feedthrough for the wires. A small amount of EPOTEK 353ND is placed to fix the wire to the spacer for strain relief on the piezo when handling the wires, but space is left for gas flow.

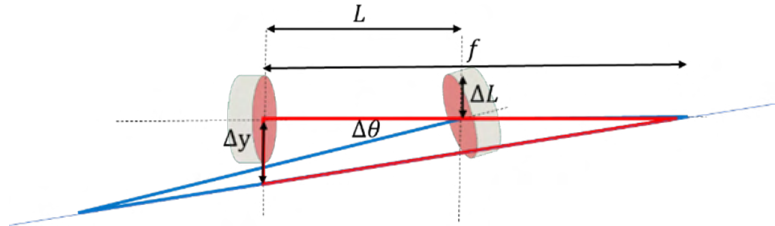


Figure 5.11: **Mirror Alignment Sketch.** ℓ is the mirror separation, f is the focal length, $\Delta\ell$ is the vertical misalignment, $\Delta\theta$ is the angle misalignment, Δy is the position of the cavity axis on the mirror, which should be inside the dimension of the mirror or any apertures.

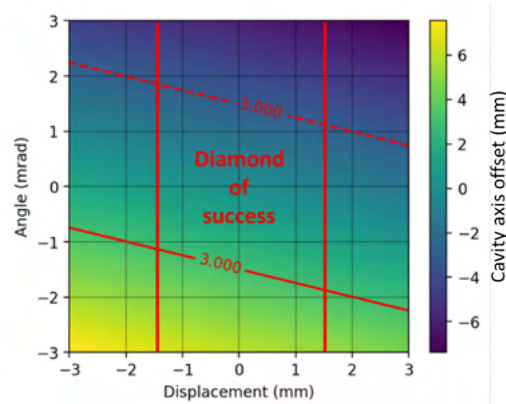


Figure 5.12: **Diamond of Success.** The tolerance of angle and translation required to align the cavity axis through a 6 mm radius hole with $\ell = 37$ mm and $r_{OC} = 4$ m. Outside the region called the diamond of success shows the deviation of angle and displacement, which means cavity alignment is not possible.

5.6.4 Cavity Assembly

To aid in the cavity construction and alignment, we had three criteria for the cavity assembly setup:

- The breadboard is aligned vertically so gravity acts to help keep the mirror and gluing surfaces level and prevent glue flowing to undesired areas.
- The cavity can be heated uniformly to 120 C to cure the glue.
- A laser beam that can probe the cavity during alignment, and before and after baking.

The setup is shown in the photo collage in figure 5.13, and the whole procedure of gluing piezo and mirrors to spacer takes two days, with most of the time spent on baking for several hours to ensure a good cure.

The order of operations for assembling and gluing the cavity spacer was as follows:

1. Glue the piezo to the first mirror, trying to center the piezo ring with the center of the mirror. Bake.
2. Glue the mirror piezo stack to the cavity spacer. Bake.
3. Align a laser beam to thread the center axis of the cavity spacer and get perfectly retroreflected, verified by maximizing the coupling back into the fiber. This was monitored at the rejection port of an optical isolator upstream.
4. Place glue on the edges of the now aligned mirror. Bake.
5. Couple back into the cavity again to verify that the bake did not change the alignment.

The choice of glue is important when planning how to assemble your cavity mirrors, piezo, and spacer, especially for UHV requirements. Anecdotally, we have had bad experiences with the Torr-seal glue for securing cavity mirrors to the cavity spacer, with stories of mirrors falling off inside vacuum. So, we spent time investigating an alternative. For our application, the main considerations are how the glue is cured, how much it outgasses, and its viscosity.

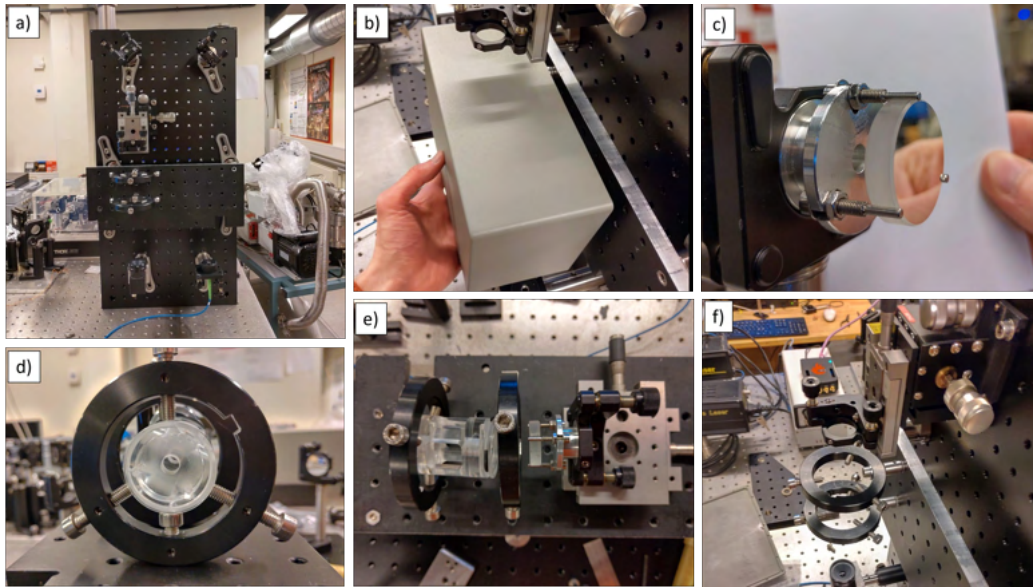


Figure 5.13: **Cavity Assembly Collage.** An acrylic mock cavity is used during testing and preparation of the setup and is pictured here. Panel a) shows the laser setup with a fibre and collimator launching up and two mirrors to reflect the beam towards the cavity, and a photodetector in cavity transmission. In a), as well as e) and f), shows the 3-axis micrometre positioner with a 4th positioner along the cavity axis for further reach. The mirror is held in a grip that mounts into a mirror mount, shown in panel c). The cavity spacer itself is secured at 6 points, shown in panel d). Panel b) shows the box containing two heating resistors that surround the assembled cavity for baking.

High viscosity glue is used like cement for building over large gaps $> 100\ \mu\text{m}$, and low viscosity is used for small gaps $< 100\ \mu\text{m}$ and fillets. We opted for low viscosity for a few reasons:

- At the $100\ \mu\text{m}$ glue width, the thermal expansion starts to contribute to the overall length change since the Zerodur material has such a low coefficient of thermal expansion. However, most of the expansion is likely dominated by the piezo itself expanding, so this was just a precaution.
- Even for low outgassing glues, exposed surface area still contributes to outgassing, and using lower viscosity glue meant smaller gluing spots, less glue, and less available surface area for outgassing.

The glue of choice, also used by several other groups, was heat-curing Epotek 353ND. After 10-15 minutes, the glue would already start to become firm but requires a bake at $100\ \text{C}$ for an hour to benefit from its full low-out-gassing performance. Figure 5.14 shows our gluing strategy. We avoided making any fillet joins (where the glue climbs up the edge) because the piezo's performance can be compromised if it becomes restricted in the axis of its expansion.

5.6.5 Piezo Bode Plot

The response of a piezo with a cavity mirror glued to it can be measured in several ways, and having a bode plot is very useful in understanding the behaviour of feedback for stabilization. Here, we probe the transfer function of the piezo by applying a sine wave of constant voltage amplitude to the piezo input while varying the frequency and monitoring the cavity transmission. The light injected into the cavity has sidebands at constant frequency offset. These sidebands are used as markers to relate the input phase and amplitude to the output phase and amplitude of the system for a given frequency. The results are plotted in figure 5.15. The first piezo resonance is at $3600\ \text{Hz}$ which must be navigated by appropriate digital or analog low-pass filters.

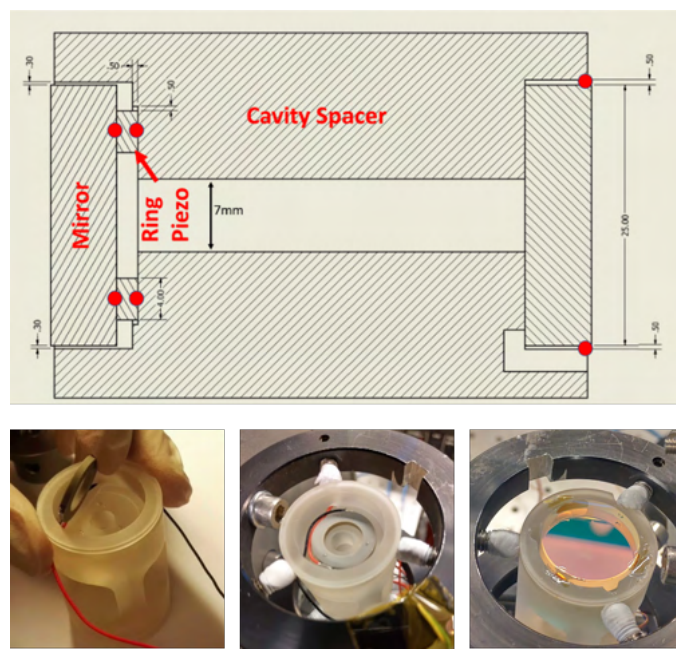


Figure 5.14: **Gluing Strategy.** A cross-section schematic of the cavity with critical dimensions indicated in millimeters. The red circles indicate where the glue is applied. The series of photos are in order of procedure from left to right.

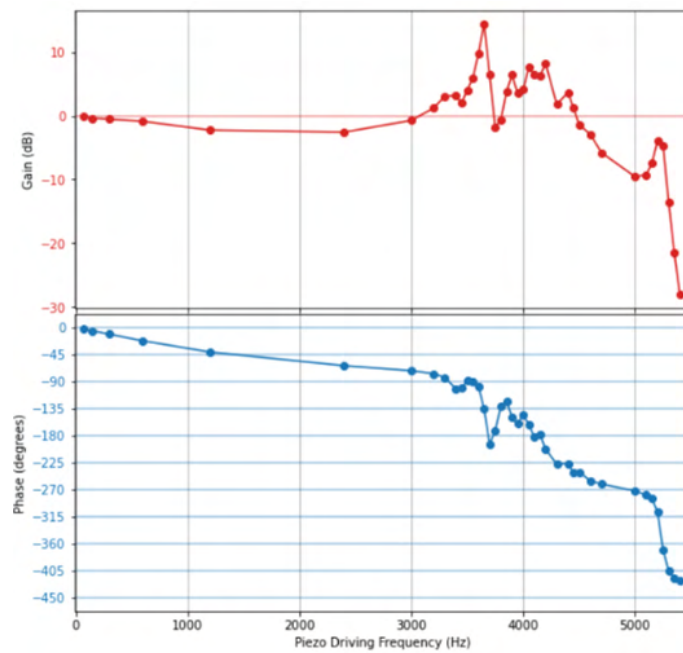


Figure 5.15: **Piezo Bode Plot.** Gain and phase response of piezo mirror with respect to frequency. The first resonance is around 3600 Hz.

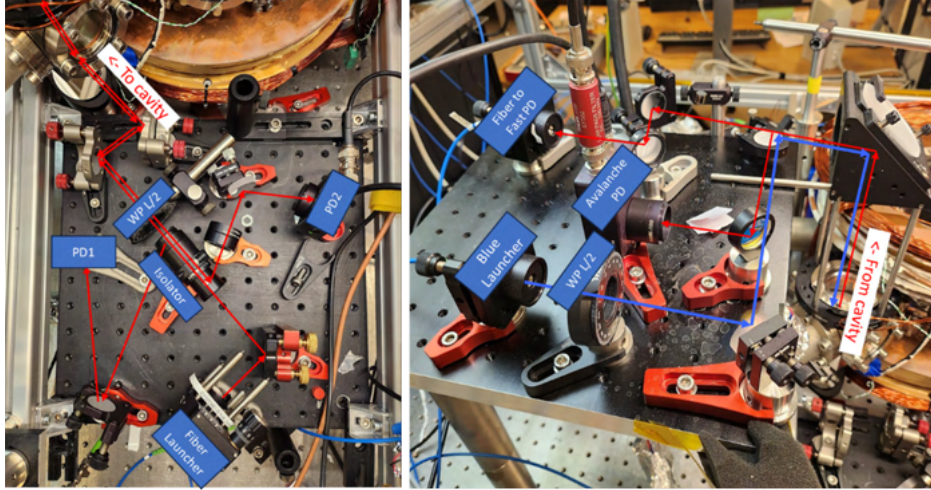


Figure 5.16: **Annotated Photos of Cavity Optics.** Left shows the launching of 689 nm light towards the cavity. The isolator rejection ports are used to monitor the power on PD1, and the back-reflection from the cavity is sent to PD2 for PDH stabilization. Right shows the optics in transmission, including a flip mirror to send the cavity transmission light either to a fibre-coupled fast photodiode, or avalanche photodetector. A dichroic mirror allows the launching of blue probe light in reverse through the cavity.

5.7 Optics for NICE-OHMS

To stabilize the cavity in preparation for NICE-OHMS measurements, we stabilize the spectroscopy cavity to the spectroscopy laser. Locking the optical cavity to the laser is performed with a Pound-Drever-Hall (PDH) lock, a ubiquitously used locking technique that is simple to implement. The sidebands for locking the cavity are applied alongside the sidebands for NICE-OHMS using the same EOM and summing two radio-frequencies.

5.8 Control with Red-pitaya

Red-pitaya (RP) is a company that sells a cheap programmable digital radio with two input channels and two output channels. It is easy to get started and easily customizable for the more complicated tasks thanks to the opensource

software and firmware. We use the 125-14 model which has 14-bit output resolution and $125 \text{ MS} \cdot \text{s}^{-1}$ and bandwidth between 0-50 MHz. If powered by a clean linear power supply rather than the stock switched power supply supplied by the manufacturers, the red pitaya is sufficient for most of our applications. We use four separate RPs with the PyRPL GUI [73] to perform:

- Automated cavity transmission search and locking
- Power stabilization with an AOM
- Cavity PDH lock-in detection
- Intelligent laser current control

5.9 Microwave Beat Detection in Cavity Transmission

NICE-OHMS, detailed in Chapter 3, requires the detection of a beat note at the free-spectral range of the optical cavity. The free-spectral range of our cavity is at 3.7 GHz, placing it uncomfortably in the microwave regime where great care must be taken with impedance matching, connector wear-and-tear, grounding, capacitive and inductive coupling, etc. These issues mostly arise due to the wavelength of microwaves matching the size of cables and connectors. Also, photodetectors in the visible wavelengths are not widely available beyond response speed of 1 GHz due to limitations in carrier mobility in the material, so our options were limited. Synthesizers and spectrum analysers at 4 GHz are more specialized, so the chance of finding the correct equipment in a lab that deals mostly with radio-frequencies can start to be challenging when wanting to prototype different schemes quickly.

5.9.1 Microwave Electronics

We purchased a Newport 818-BB-45F fibre coupled, non-amplified, battery biased, fast photodetector, the only one we could find at the time with high enough bandwidth and sensitive to 689 nm light. We mounted it firmly in a metal box along with 3 amplifiers ZX60-83LN-S each providing roughly 22 dB of gain and 1.3 dB noise each, and a band-pass filter with a passband of 3 to 4.3 GHz. The electronics are contained in a metal box shown in figure

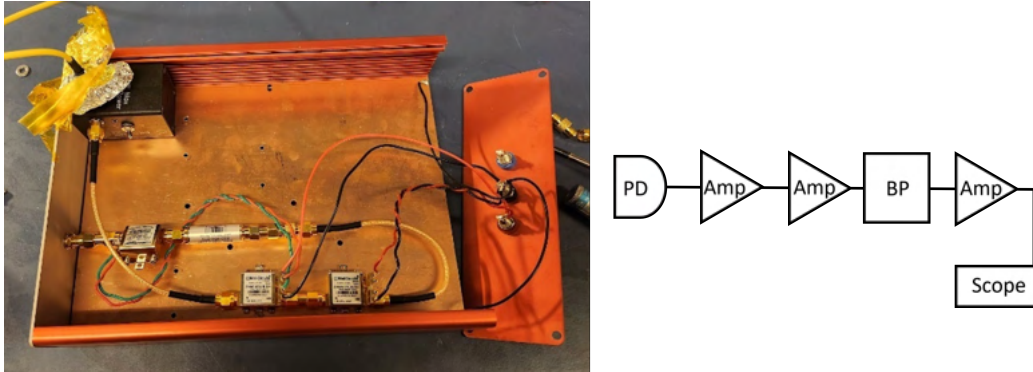


Figure 5.17: **Microwave Detection Electronics Box.** The photodetector is battery-powered. The amplifiers are screwed into a copper grounding plate. The amplifiers are powered by banana sockets supplying ± 15 V. The box is closed and fixed with a metal lid, and small holes are covered with aluminium. PD: Photodetector, Amp: Amplifier, BP: Bandpass, Scope: Oscilloscope

5.17 with metal coil or tape covering holes to prevent transmission into and out of the box.

5.9.2 Quantifying Beatnote

The problem with testing the detection scheme is NICE-OHMS produces a zero beat note when there is nothing to provide a phase-shift inside the cavity, and before we go looking for atomic phase shifts, the electronics should be tested. So instead, we operate at a modulation frequency of $\text{FSR}/2$ such that only the 2nd order sidebands on the light are transmitted through the cavity and the 1st order sideband get reflected. Now the relative phase ensures the beat-notes sum rather than cancel.

To estimate the signal size and scaling for a given beatnote, and measure the noise equivalent power, we slightly detune from $\text{FSR}/2$ so that the cavity transmission is non-degenerate and the power can be individually detected on a power-calibrated Thorlabs avalanche photo-detector by scanning the cavity length with the piezo, see figure 5.18.

The beat note equivalent power, the power that corresponds to the signal size if scaled by the detector responsivity, can be described for the $\text{FSR}/2$ modulation case as:

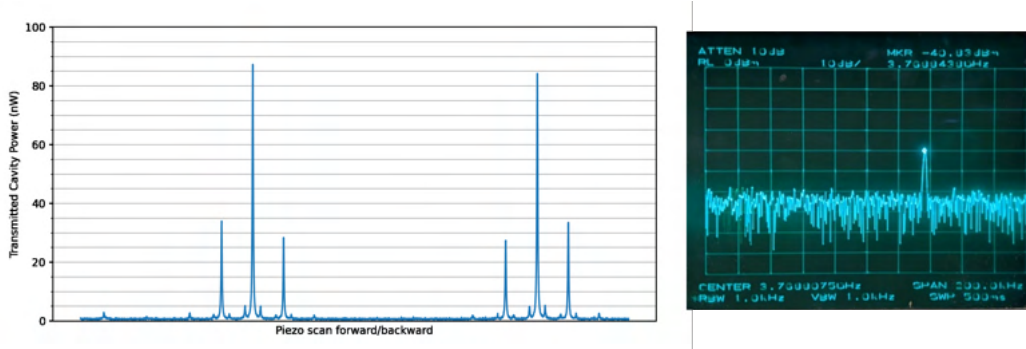


Figure 5.18: **Transmitted Cavity Power with Sweep Piezo.** Left: The optical triplet power in transmission is shown for a cavity piezo sweep. Two triplets are visible due to a forward and backward scan. The imbalance between lower and upper sideband is due to RAM. Extracting the lower sideband, carrier, and upper sideband power is used to quantify the estimated beat signal. Note: only for this illustration, the ± 2 lower and upper sidebands are slightly detuned from $\omega_{\text{FSR}}/2$. Hence, the degeneracy is broken, and transmission peaks do not overlap. Right: Resulting beatnote signal on spectrum analyzer with 1 kHz bandwidth.

$$P_{\text{beat}} = 2\sqrt{P_{US}}\sqrt{P_C} + 2\sqrt{P_{LS}}\sqrt{P_C} \quad (5.2)$$

Where P_{US} , P_C , P_{LS} are upper sideband, carrier and lower sideband power respectively. From the spectrum analyzer SNR of 20 dB for 1 kHz detection bandwidth, and $P_{\text{beat}} = 209 \text{ nW}$, we find a NEP for this detector at 689 nm and 4 GHz of $100 \text{ pW} \cdot \sqrt{\text{Hz}}$. This is twice the NEP as quoted by the manufacturers to be $< 45 \text{ pW} \cdot \sqrt{\text{Hz}}$. The discrepancy is reasonable when considering power losses from coupling the transmitted cavity light into the detector fibre, and extra noise from the amplification chain.

5.10 Testing Microwave Electronics with FM Spectroscopy at Oven Nozzle

The highest density of cold atoms is right at the oven nozzle, given there is no other laser cooling in the experiment. This gave us an idea to test the FM spectroscopy with the microwave electronics and the detector at the oven

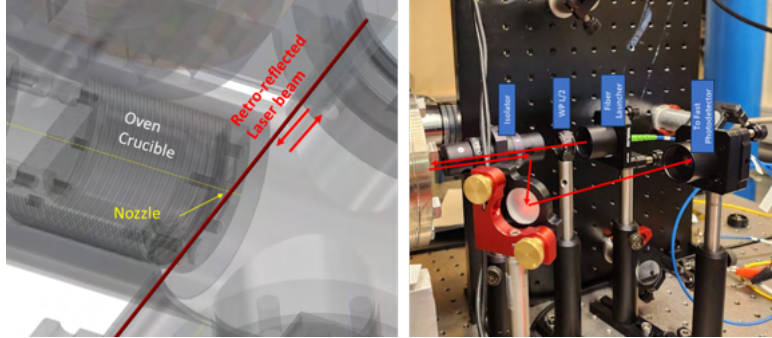


Figure 5.19: **Geometry of Oven FM Saturation Spectroscopy Measurement.** (left) A 3D CAD drawing of the retro-reflected laser beam intersecting the oven nozzle and (right) the launching optics including an isolator to send the retro-reflected beam to a fiber connected to the GHz photodetector.

nozzle, to ensure everything was working as expected and the frequency is indeed correctly shifted and no signs errors were made with AOM frequencies. To begin with, it would be easier to confirm a signal at the oven compared to measuring atoms in the cavity. Doing frequency modulation spectroscopy with sidebands at a microwave frequency is usually an unnecessary technical complication when there is no cavity, except for the one case where the sidebands are beyond the Doppler width of the atoms (see the spectrum out of the oven in figure 5.3), so the only signal from the atoms comes from the carrier. We anticipate to resolve a saturated feature. This is a test in preparation for NICE-OHMS on a cold beam and note there is no (intentional) fabry perot cavity, just a single back-reflection so effectively a finesse of 2.

As illustrated in figure 5.19, laser light at 689 nm on-resonance with the $^1S_0 \rightarrow ^3P_1$ transition of ^{88}Sr is brought to the oven through a polarization-maintaining single mode fiber. A frequency triplet is produced with a fiber coupled EOM at roughly 3.7 GHz, with about 25% of the total power in the sidebands. The light is launched with an aspheric lens $f=11$ mm, beam size=0.15 cm, into an optical isolator before reaching the entrance window with access to the oven nozzle. We use an isolator instead of a series of beam splitters to minimize optical losses. The laser beam is aligned roughly 0.5 cm from the nozzle and retro-reflected from the opposite window. There is 0.85 mW after the isolator before the window, 0.70 mW before the retro-reflection mirror. The returning retro-reflected beam of 0.34 mW is taken

from the rejection port of the isolator and injected into a fiber that is coupled to the fiber photodetector. The laser light is frequency swept with a sawtooth wavefunction at 60 Hz over a range of ± 2.5 MHz with an AOM further upstream at the laser board, see figure 5.8. The light is power stabilized with the same AOM due to significant fluctuations due to varying AOM efficiency during the sweep. The detected beat note (the signal) is demodulated by splitting off the original drive (the LO) and combining them on a mixer. The phase delay between the signal and LO is not a free parameter, so instead, it is tuned by varying the modulation frequency on the order of 1 MHz. We optimize the phase to yield a demodulated signal that has an average of zero i.e. dispersive-like. The demodulated signal is measured on an oscilloscope that is synchronized to the AOM sweep. 5000 averages are made of 10,000 points which corresponds to an integration time of 80 ms per point, resulting in figure 5.20.

The purpose is to find a signal that can indicate that the laser detuning is close to the $^1S_0 \rightarrow ^3P_1$ transition and that the microwave electronics operate as expected. The spectrum shows a saturated feature is more featured than expected, and the side bumps are not well understood. The saturated feature is about 600 kHz wide from peak to peak, and the signal-to-noise is 26 for an integration time of 80 ms per point.

We can use this to estimate a benchmark for a stabilization scheme using fm-spectroscopy at the oven nozzle. Taking values from figure 5.20 and using equation 1.1, $Q = 7.3 \cdot 10^8$, $\text{SNR} = 26$ at an integration time of 80 ms results in an estimated short-term stability of approximately $1.5 \cdot 10^{-11} / \sqrt{\tau / 1 \text{ s}}$. This is roughly an order of magnitude larger than similar simple beam spectroscopy methods [40]. The introduction of laser cooling and cavity-enhanced phase measurements should be able to beat this. If it cannot, it does not warrant the extra complexity.

5.11 Conclusion

The construction of the strontium beam machine is detailed, including the different parts of the experiment, the preparation of UHV parts, the oven, the magnetic coils including their geometries, the lasers with diagrams detailing the components, the cage optics for delivering light to the Zeeman slower and 1D MOT, the optical cavity alignment and gluing, the optical breadboard setup for NICE-OHMS detection, and characterizing the microwave electron-

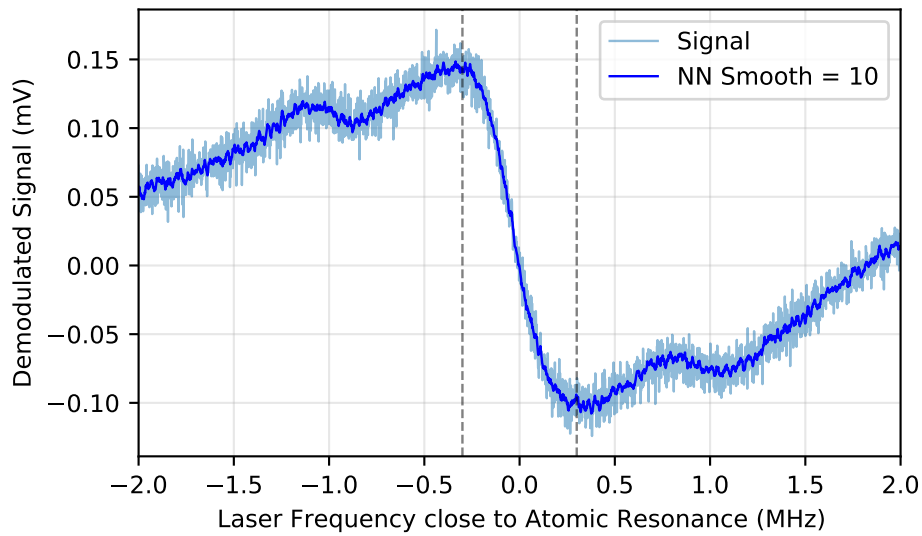


Figure 5.20: **Frequency Modulation Spectroscopy at Oven Nozzle on $^1S_0 \rightarrow ^3P_1$ Transition.** The signal for FM spectroscopy at the oven nozzle exhibits a typical saturated feature with an extra pair of dips offset symmetrically from the center. The origin of these dips is not understood. The signal size is normalized to the standard deviation, and the signal is also replotted with nearest-neighbour smoothing with 10 points to show the dips more clearly.

ics and fast photodetector. We finished with FM spectroscopy on the oven nozzle with the electronics built to confirm the electronics were correctly implemented. The characterization of the deflected atomic beam at the cavity chamber is carried out in the next chapter.

Chapter 6

The Strontium Beam Machine Characterization

With the beam experiment now built and operational, as well as the details given in the previous chapter, we want to characterize the atomic beam after deflection.

The angled 1D MOT has some useful degrees of freedom. It can be used as an atomic shutter by switching off the laser beam or stepping the frequency away from resonance. This is useful for making a time-of-flight measurement of the atomic velocities. The angled 1D MOT also vary the deflection angle over a small range by tuning the magnetic field quadrupole centre with compensation coils. This is useful for aiming the largest atomic flux through the centre of the cavity mode with high fidelity and, in the future, might be a handy degree-of-freedom to stabilize the atom number through the cavity.

The following sections will go into detail about characterizing the atom number, velocity, and deflection with compensation coils.

6.1 Overview

The 1D MOT CAD and photographs of the real implementation are shown in figure 6.1. The MOT coils running at 3.23 A produce a field gradient at the coil centre of $2.9 \text{ G} \cdot \text{cm}^{-1}$. The MOT coils barely warm at this low current, so no water cooling is used to avoid the risk of leaks and minimize vibrations from the flowing water. The Zeeman slower is running at 20 A.

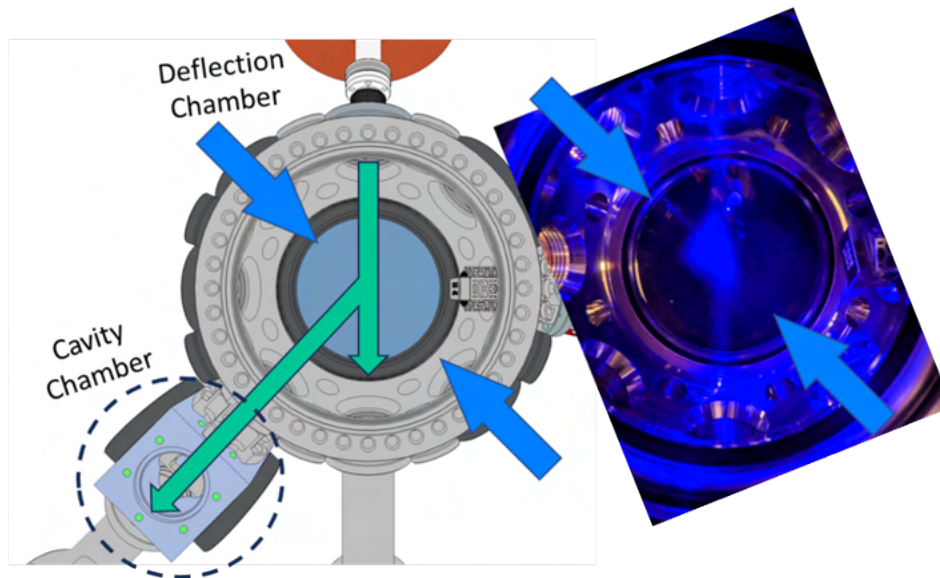


Figure 6.1: **1D Deflection MOT Chamber CAD and Laboratory Comparison.** The deflection chamber in perspective view is shown with blue arrows indicating the direction of MOT beams and green arrows indicating the atomic beam. The DN160 window at the deflection chamber and the DN40 window in the cavity chamber are omitted for clarity. The equivalent view in the experiment is shown right where the fluorescence can clearly be seen by eye/phone camera. The dim blue line vertically is residual atomic fluorescence from the Zeeman slower.

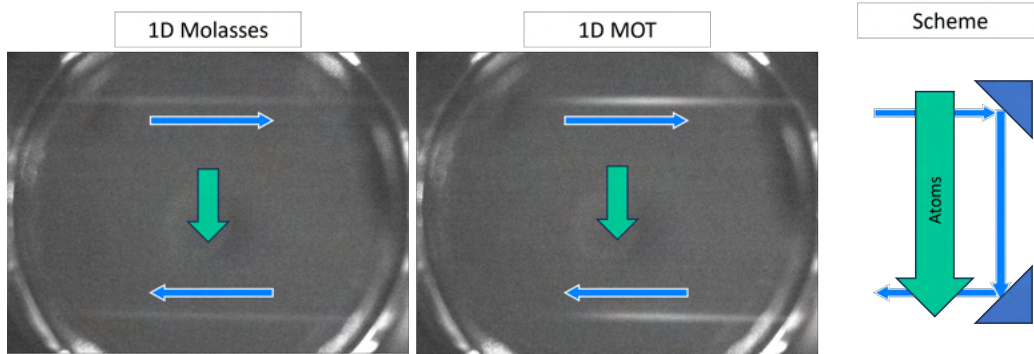


Figure 6.2: **Molasses vs MOT.** View from the top down into the cavity chamber. The horizontal arrows represent the direction of the retro-reflected probe beam at 461 nm, also shown in the scheme (right). There is a clear difference between fluorescence and, hence, the density of atoms when the MOT coils are off (left) versus on (middle). This shows the magnetic field allows the cooling light to compress the atomic beam. There is no line-of-sight from this view to the oven, so the atom beam can only arrive here by laser deflection. The small circle in the background is an out-of-focus screw hole on the optical table.

We could easily verify the deflected atomic beam’s presence by using on-resonance probe beams at 461 nm retro-reflected through the cavity chamber, see 6.2. Then, the parameters like laser polarization, power, alignment, MOT coil, and deflection coil current could be optimized.

6.2 Varying Deflection Angle with Compensation Coils

To characterize the pointing direction of the atomic beam, we implemented two pairs of compensation coils mounted with a separation close to the Helmholtz criteria around the deflection chamber, one pair along gravity “Gravity bias coils”, the second pair with an axis on the plane of atomic deflection “Deflection bias coils” (see previous chapter). We apply a current through the coil pair that provides a uniform constant offset field along the horizontal plane - the same plane as the deflection angle of the 1D deflection MOT. Varying this current, and thereby the centre of the magnetic

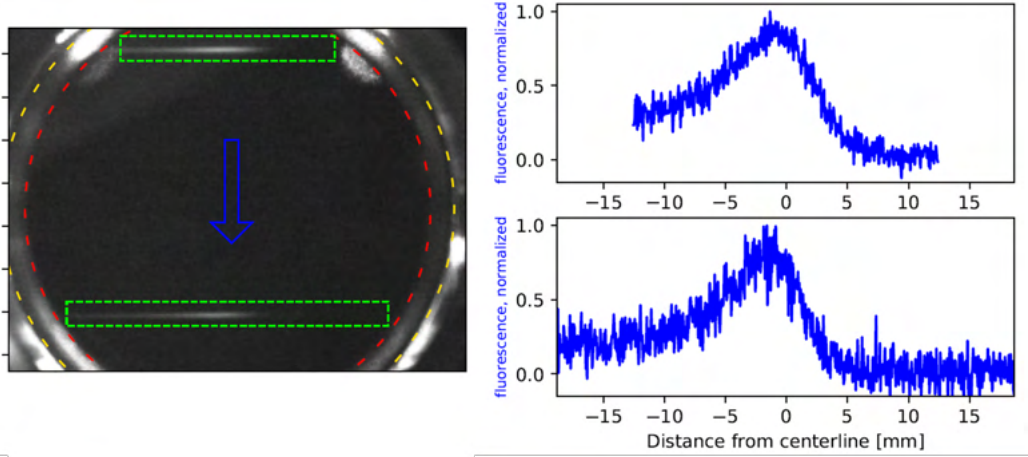


Figure 6.3: **Atom Deflection Measurement Setup.** Left shows the camera with atomic beam fluorescence, and right shows fluorescence profiles after background removal plotted versus the camera’s horizontal axis, scaled to position. The 2D box is compressed to 1D by summing vertical pixels. The red and yellow circles are the DN40 inner steel tubing of the 6-axis cube, and we use the average diameter of the two circles to estimate the pixel-to-position scaling. The atomic beam travels top to bottom just like in figure 6.2. Author: Jonathan Elsborg.

quadrupole, varies the deflection angle and translates the centre of the 1D deflection MOT. These measurements were made before the cavity was placed into vacuum because the optical access would be blocked by the cavity itself.

We set up an on-resonance probe laser beam at 461 nm in a double pass configuration at the cavity chamber. The first pass and its retro-reflection are translated by 3 cm using a right-angle retro-reflector to intersect the atomic beam at two different locations along the atomic beam propagation axis. A FLIRview camera is placed from above, pointing down along the axis of gravity through the cavity chamber (the cavity is omitted for now). The on-resonance probe intersecting with the strontium atoms reveals fluorescence on the camera, indicated by the dashed green boxes in the left sub-figure in figure 6.3. The top dashed green box is the forward pass, the profile is plotted in the top-right of figure 6.3, the retro-reflected (and dimmer because of probing power losses, not fewer atoms) beam is plotted bottom-right of figure 6.3.

The fluorescence profile along the camera’s horizontal axis shows an asymmetry; the right side corresponds to a larger deflection angle and has a steeper cut-off than the left side, which corresponds to a shallower deflection angle and a steady cut-off. This “tail” on the left side comes from the atomic velocities out of the Zeeman slower that are slightly too fast to be deflected nominally but still make it into the cavity chamber.

We can see the atomic beam moves by studying the fluorescence profile while changing the current in the deflection bias coils; see figure 6.4. The total fluorescence appears to be robust for all currents, meaning we are not ruining the efficiency of the MOT by applying the bias field. We smooth the profile with nearest neighbour averaging, find the position of peak fluorescence for various coil currents, and plot it in figure 6.4. A line of best fit produces a gradient of $dy_1/dI = 0.616 \text{ cm} \cdot \text{A}^{-1}$ for the lower beam (further away from the 1D MOT), and $dy_2/dI = 0.554 \text{ cm} \cdot \text{A}^{-1}$ for the upper beam (closer to the 1D MOT).

Using the distance from the 1D MOT centre to the cavity chamber, we can estimate the beam translation and beam angle for a change in current using small angle approximation and assuming linearity:

$$y = \theta \cdot L + c \tag{6.1}$$

Where y is the final position, θ is the deflection angle change from 45° , L is the distance from probe beam to 1D MOT, and c is a translation. Finding the partial differential with respect to the current I , we can solve for the change in angle per current $d\theta/dI$ and translation per current dc/dI :

$$\frac{dy}{dI} = \frac{d\theta}{dI}L + \frac{dc}{dI}, \quad \frac{d\theta}{dI} = \frac{(\frac{dy_1}{dI} - \frac{dy_2}{dI})}{L_1 - L_2} \tag{6.2}$$

Using $L_1 = 15 \text{ cm}$ and $L_2 = 18 \text{ cm}$, $d\theta/dI = 0.020 \text{ rad} \cdot \text{A}^{-1}$, and $dc/dI = 0.256 \text{ cm} \cdot \text{A}^{-1}$. For 15 cm , $L_1(d\theta/dI) = 0.3 \text{ cm} \cdot \text{A}^{-1}$.

6.3 Beam Detection with Camera

Now that we have placed the cavity into vacuum for these next measurements, we want to verify and optimize the atomic beam flux through the cavity. We prepare laser light of 461 nm with 0 MHz detuning from $^1\text{S}_0 \rightarrow ^1\text{P}_1$ transition in ^{88}Sr to probe the beam with maximum fluorescence. The laser beam

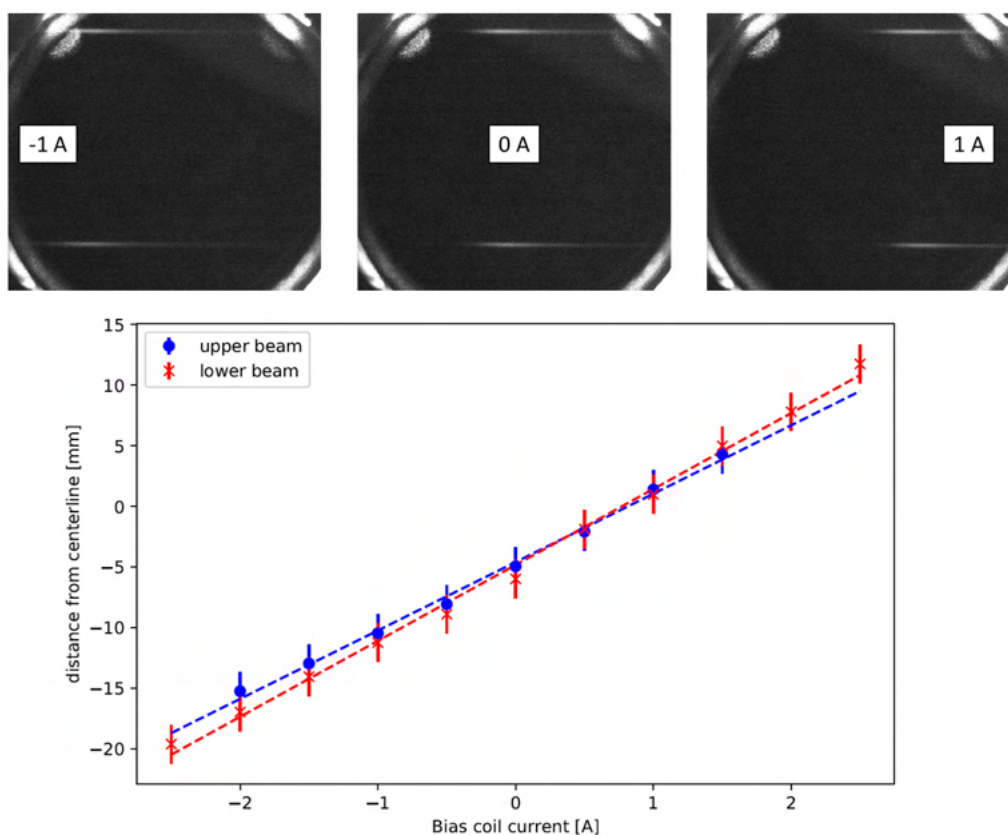


Figure 6.4: **Deflection MOT Tuning with Bias Coil.** Left shows a series of camera images at $[-1,0,1]$ A bias coil currents, the fluorescence (and therefore atomic beam) moves with respect to the static vacuum chamber around it. Right shows the peak plotted for both upper and lower beams, with the error-bars indicating half the size of the smoothing window used to remove noise, and a trend line from which the translation per current and angle per current are calculated.

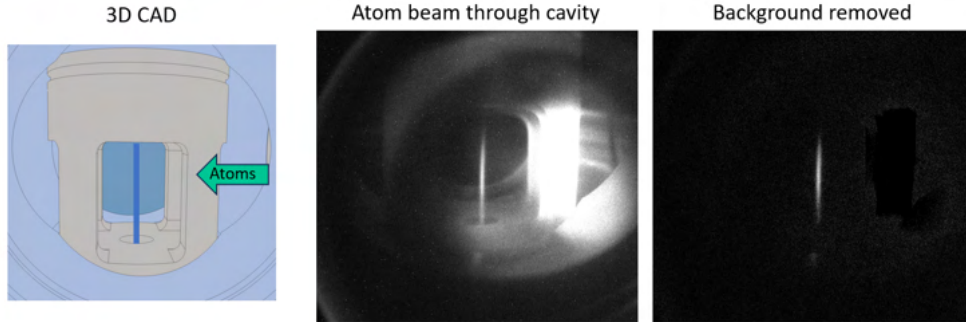


Figure 6.5: **Atom Beam Detection with a Camera.** The atomic beam transiting the cavity axis travels from right to left for both images. Left shows the CAD drawing in perspective view with the laser beam and atomic beam illustrated. Middle shows an unprocessed image showing the fluorescence from the 461 nm probe beam. The bright glowing region just right of the fluorescence is scattered light off the cavity spacer from the deflection chamber. Right shows a background removed image where only the fluorescence from the atoms remains.

transmits through the cavity because each cavity mirror only has 70% transmission for this wavelength. This beam is sent the opposite way through the cavity compared to the direction of the 689 nm locking and interrogation light (see 5.16), so the two laser beams can be very well overlapped, giving us confidence that atoms seen with the blue 461 nm light should also be seen by the 689 nm light resonant with the cavity.

In the perpendicular plane to the cavity axis, a monochrome FLIR camera with aperture size approximately 5 mm and focal length 30 mm, is pointed at the cavity axis. An exposure time of 0.2 s and 47 dB gain is required to see the weak 461 nm fluorescence of atoms transiting the cavity axis, but still provides an update rate of 5 Hz, responsive enough for comfortably optimizing the atom number. Figure 6.5 shows an example of an image taken with the camera. The cavity spacer is shown in more details in figure 5.10.

We can already place an upper estimate of the beam temperature along the cavity axis by taking the approximate FWHM of the beam intensity distribution along the cavity axis of 2 cm. Assuming ballistic motion over the 16.5 cm from the 1D MOT region, and a point source (which is not the case but useful for estimating an upper limit), and assuming that the atomic

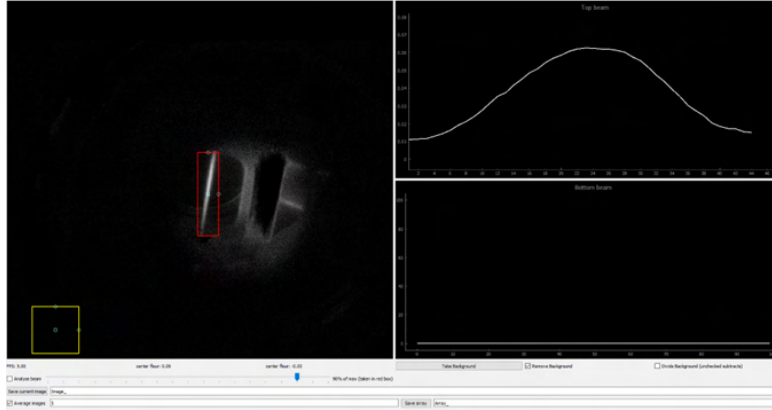


Figure 6.6: **Camera User Interface Programmed by Jonathan Elsborg.** Pictured is the user interface with averaging, background removal, and saving functionality. The left panel shows a live image with a red bounding box (yellow is not used in this case). The background is already removed from this signal, but slight fluctuations in laser power cause the scattered light off the cavity spacer to be visible again after a while. Top right panel shows the light intensity over x or y-axis. The bottom right panel shows the integrated pixel intensity in the bounding box over time.

beam is not being focused (which might be happening) and a beam velocity of $30 \text{ m} \cdot \text{s}^{-1}$, we find a $\Delta v_{\text{cav}} = 1.8 \text{ m} \cdot \text{s}^{-1}$ which corresponds to 3.4 mK. The Doppler limit is 0.7 mK and since the MOT beams operate at around 40 mW, we would not expect to reach this limit because the intensity is high.

The FLIRView camera software was useful in finding the right parameters and provided many options; however, it could not offer automatic features such as background removal and pixel cross-section plotting, and area summations. Jonathan Elsborg built a custom user interface in Python to do that so image processing could be done online. The GUI is shown in figure 6.6. As defined by a user-defined bounding box, the intensity variation along the x or y-axis of the camera is plotted, and the bounding box also defines the area to integrate over for an estimate of total number of photons arriving. These features helped the user improve the atomic density, making identifying small improvements that accumulate to make a significant change easier.

6.4 Atom Number and Velocities

The instantaneous atom number inside the cavity is the most critical parameter, relating to N in equation 4.1, so we need to estimate it. Counting atoms with the broad $^1S_0 \rightarrow ^1P_1$ transition is easier than with the $^1S_0 \rightarrow ^3P_1$ transition because the transition linewidth is larger than the Doppler width, and the scattering rate is very large, resulting in a large signal-to-noise.

We prepare absorption spectroscopy with the 461 nm light already transmitting through the cavity by directly detecting the change in power on the laser beam itself with a photodetector. In parallel, a second path is monitored that does not interact with the atoms for use as a measurement of laser intensity fluctuations and will be used for background removal. To toggle the atoms on and off, we place a Stanford Instruments shutter in the path of the MOT laser beam, which has an on-to-off switching time of around 1-2 milliseconds. The cavity is resonant for 689 nm but mostly transparent at 461 nm with a small transmission loss of 30% per cavity mirror. While the atomic beam is on, the Sr atoms scatter the 461 nm light and this is observed as a dip in transmission monitored by a photodetector. Switching off the MOT beams, switches the atomic beam off and the transmission on the photodetector rises again. The delay and transient of the absorption on the photodetector correspond to the velocities of the atoms traversing the probe laser, shown in figure 6.7.

In both signal and background, there are oscillations with a frequency of approximately 800 Hz, which also appear to be coherent with the triggering of the sequence every 1 s, even after 20 averages. The origin of these oscillations could be vibrations traveling through the table at a frequency that is a perfect multiple of the triggering rate, like a fan in a current supply or synthesizer. Alternatively, it could be the action of the clicking sound of the shutter that knocks the laser optical breadboard, causing it to vibrate at a characteristic frequency. This is likely exemplified by the sensitive coupling of the source laser into a single-mode fibre before reaching the experiment. These oscillations are on the order of 0.3 nW, which in relation to the total power of 15.1 μ W, corresponds to 2 parts in 10,000. Fortunately, the oscillations are efficiently canceled when the background trace is removed from the signal trace. We digitally scale the background trace to minimize the oscillations because the signal and background traces are taken on different photodetectors with different noise properties.

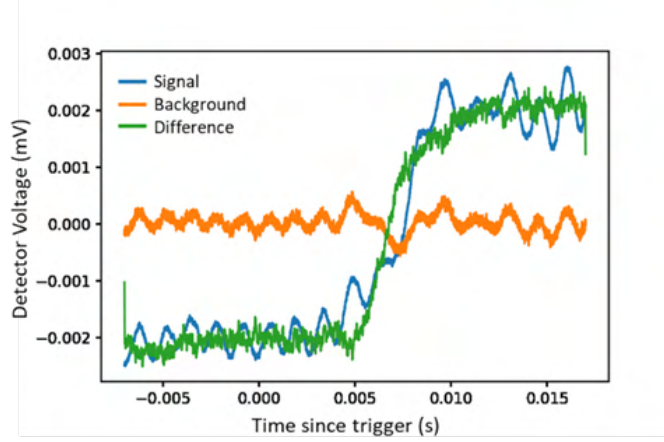


Figure 6.7: **Transient in Absorption Signal During Atomic Beam Shut-off.** Raw photo-detector output for signal and background with 20 averages, both containing oscillations that are then efficiently removed by taking the difference of the signals. MOT laser, and therefore atomic beam, is switched off at $t=0$.

Using just the peak-to-peak change in signal between beam off and beam on, we find the instantaneous atom number inside the cavity volume to be 7900(1700). Appendix B details calculations and error propagation. The primary source of the uncertainty is the ratio of the cavity waist radius versus the waist radius of the probing laser because the dimensions are very small and contribute twice to the uncertainty because they are used to calculate an area. The quoted atom number differs from day to day, and sometimes even hour to hour, due to fluctuation in laser power, and this fluctuation is not accounted for in the uncertainty calculation. Anecdotally, this atom number is closer to the best-case scenario, where all lasers were functioning nominally. However, there is still plenty of room for optimizations that have not been explored due to lack of time and stability issues. Significant improvements in atomic flux could be found in optimizing the 1D MOT detuning from atomic resonance, an extra optical molasses at the oven, or a redesign of the vacuum chamber to accommodate a shallower deflection angle.

Now, looking into the transients of the beam switch-off in figure 6.7, we perform a reciprocal transformation of the time axis and scale by 15 cm, which is the distance from the MOT to the cavity, to find the corresponding velocity of an atom. Then we take the differential with respect to velocity of

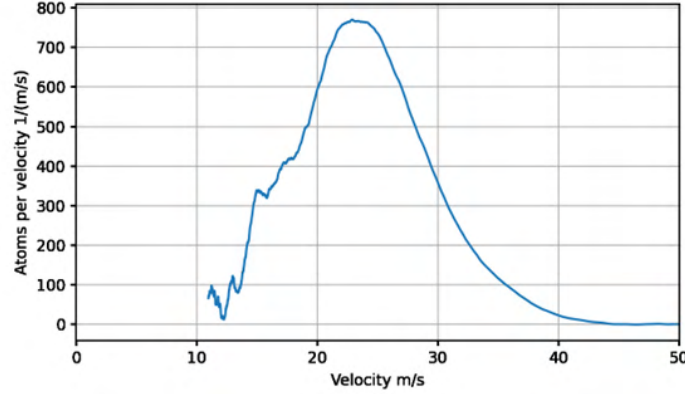


Figure 6.8: **Time-of-flight Atoms vs Velocity.** The velocity along the beam propagation direction is plotted versus the density of atoms per velocity. The area under the curve results in the total atom number.

the y-axis – equivalent to the atom number – to find a velocity density, see figure 6.8. The total atom number is the area below the curve bound by an upper and lower velocity. The distribution is remarkably narrow, with most atoms possessing a velocity between $15\text{-}35\text{ m}\cdot\text{s}^{-1}$. Using an average atom velocity of $23\text{ m}\cdot\text{s}^{-1}$, we find a flux to be $0.55(22) \cdot 10^9$ atoms/s, calculation detailed in appendix B.

6.5 Next Steps to Continuous Super-radiance

We have characterized the continuous beam of strontium, but the question remains: what more would be required to reach the regime for continuous super-radiance? Early on in the development of the beam machine, super-radiance was one of the main goals. However, as we realized it would be challenging to reach the phase-space density required to exceed the lasing threshold, the focus shifted to continuous NICE-OHMS. Although the details for continuous super-radiance were thoroughly investigated, they are outside the scope of this thesis, and the reader is advised to follow the references for more information on superradiance in the bad-cavity regime [74, 75, 25, 26, 76] and proposal of continuous superradiance on a hot beam [77, 78].

Mikkel Tang ran a simulation using his Monte-Carlo Jaynes-Cummings simulator with the parameters of the beam machine to produce a laser threshold plot in figure 6.9. We use the parameters outlined in table C.1. It's important to note this flux is the number of atoms in the excited state, so an additional pumping efficiency factor should be considered before comparing it against the achieved atomic flux quoted above. The results show that for stable lasing at 4 mK, the flux needs to be two orders of magnitude greater. We suffered from a lower-than-expected cavity finesse of 5000 where we originally targeted 22000. This loss in finesse was seen after placing into vacuum and baking out the vacuum chamber. This has the consequence that the required flux is almost $5\times$ larger.

Anecdotally through experience with the beam machine, a factor of at least $2\times$ higher flux could be achieved by fine-tuning the deflection MOT parameters like laser alignment positioning and laser detuning. Implementing 2D optical molasses at the oven could gain at least another factor of 2. Requiring a more invasive change of the vacuum geometry, a shallower deflection angle for the 1D MOT could be implemented to capture atoms with greater velocity. However, atoms with a large velocity will require long interaction distances to pump into the excited state, and a transit time broadening too high will also impact the superradiant laser.

The beam temperature along the cavity axis could be reduced with extra cooling along the cavity axis. With a stimulated emission-enhanced cooling technique like a SWAP molasses [35], significant cooling can be achieved in the 5 cm of optical access before the beam enters the cavity chamber. Based on approximate calculations and 10 mW of 689 nm cooling light, the 4 mK beam could be cooled to 40 μ K or less, bringing the threshold atomic flux lower.

Still, two challenges remain: 1) efficiently pumping the atoms into the excited state, 2) the excited state lifetime is on the same order at the transit time, meaning significant population is lost during the cavity mode transit. Point 2) can be remedied with a faster beam or a more tightly focused cavity mode volume.

6.6 Next Steps to Continuous NICE-OHMS

Compared to continuous super-radiance, continuous NICE-OHMS may still be competitive with the achievable linewidth compared to super-radiance

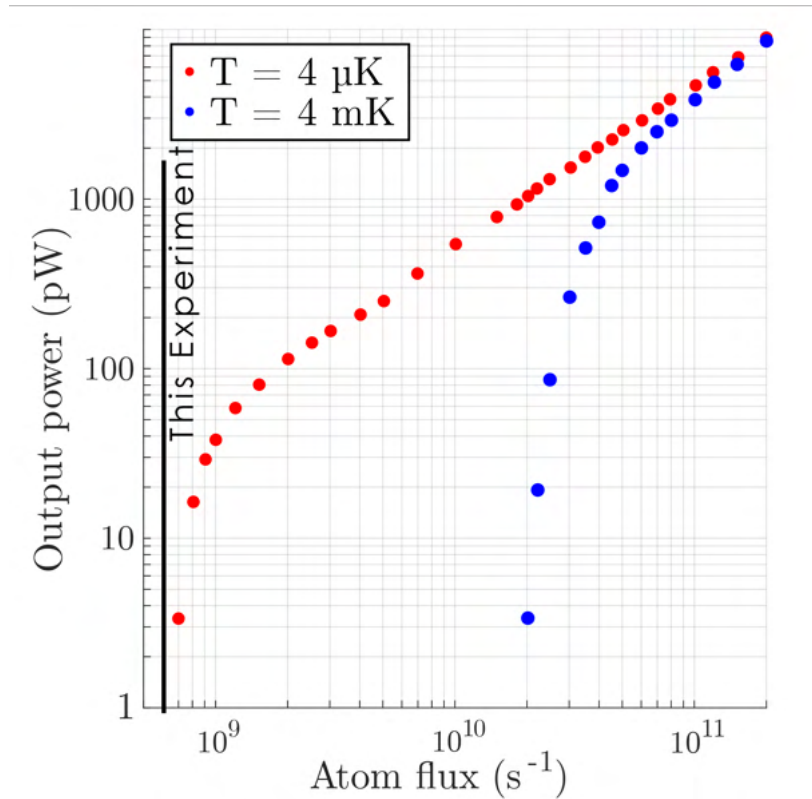


Figure 6.9: **Super Radiant Lasing Output Power for Varying Atomic Flux.** The theoretical super radiant output power is plotted against the atomic flux for two cavity-axis temperatures, 4 μK and 4 mK. The lasing power rises rapidly and joins a linear slope which relates to the maximum photons that can be emitted for a given atom flux. The cavity parameters used relate to the beam machine details in this thesis.

[20], and will be simpler to implement as it does not have a threshold and also does not need the additional infrastructure to pump the atoms into the excited state.

With the current flux and temperature, and taking the maximum phase shift in radians from figure 4.2 with a probing power of 10 nW and sideband power of 1 μ W, we could expect a maximum peak-to-peak saturated beat note power of 15 nW, and shot-noise limited linewidth at 1 s integration time of just over 1 kHz. Even though this linewidth is not very competitive in isolation, and other simpler beam spectroscopy techniques exist that do better [40, 39], it would be the first time NICE-OHMS is used on a continuous cold atomic beam for frequency metrology applications and a better shot-noise limited linewidth can be achieved with a higher atomic flux.

A great effort was made to measure the first signal with NICE-OHMS. However, we realized the main limitation was the optical losses through the triplet generating EOM and the optical cavity, which became lossy after baking out under vacuum. Starting with 15 mW, the EOM lost over 20 dB of power (and the specifications rated it to only lose 3 dB), and another 20 dB was lost in cavity transmission. Due to these losses, we are severely limited by detector noise. To worsen the problem, we found it challenging to find a photodetector with low enough noise equivalent power with a bandwidth of 4 GHz and good detection efficiency at red wavelengths. With our Newport 818-BB-45F detector, we would have needed roughly 3 mW of total power to overcome the detector noise, taking the noise-equivalent-power (NEP) of $100 \text{ pW} \cdot \text{Hz}^{-0.5}$ measured¹ in section 5.9.2. Just $10\times$ lower NEP would mean we could be shot-noise limited with 30 μ W of power. There are detectors at optical wavelengths with a NEP below $1 \text{ pW} \cdot \text{Hz}^{-0.5}$ (Menlo Systems APD210), but the bandwidth stops at 1 GHz.

6.7 Conclusion

We have demonstrated an atomic beam deflected by a 1D MOT with a flux of $0.55(22) \cdot 10^9$ atom/s traveling on average $23 \text{ m} \cdot \text{s}^{-1}$ into a region with an optical cavity that is protected from direct and blue scattered light from the Zeeman slower and MOT windows. The pointing of this beam can be

¹Unfortunately the NEP was specified incorrectly on the website by a factor of 1000 less than reality. We only discovered this after measuring and contacting them.

controlled with high fidelity by changing the current to the bias coils with no clear loss of atom number.

There is still plenty of characterization to be done, such as quantifying the dependence of atomic flux with laser power, laser detuning, and alignment. Anecdotally, there was a large sensitivity of the Zeeman slower on the atomic flux, which should be the focus of future improvements in deflected beam stability.

We discuss the next steps of the beam machine for frequency metrology. Before a NICE-OHMS measurement can be made on this atomic beam, a detector with lower noise while still offering 4 GHz bandwidth must be found.

Chapter 7

Cavity QED and Bi-stability

Taking the themes of cavity-enhanced saturation spectroscopy (Chapter 4) to their limits, the driven cavity system transitions from a linear to a highly non-linear regime. This non-linear regime is reached by increasing the atomic cloud phase space density, increasing the cavity finesse F , and keeping a narrow linewidth transition γ . In this regime, three solutions for the intra-cavity field exist, with two being stable and one dynamically unstable. This system exhibits strong hysteresis and is called the bi-stability regime. Carefully navigating the bi-stability regime promises to produce large signal-to-noise and narrow spectral features, $\Delta\nu$, that could be used to stabilize a frequency reference to very low fractional frequency uncertainties.

In this chapter, we will introduce the theory of cavity quantum electrodynamics required for the results in chapter 8 and introduce an analytical model that captures the mean-field behaviours of the bi-stability regime. Then, we briefly overview the literature on driven CQED systems for metrological applications.

7.1 CQED

Cavity quantum electro-dynamics (CQED) is the study of how the radiative properties of an atom change when placed inside an optical cavity. The circulating photons in the cavity repeatedly interact with the same atom, resulting in non-linear behaviours [79].

The strong collective coupling regime, when $NC > 1$, defines the crossover from the linear regime to the non-linear cavity QED regime and is the

product of the number of coupled atoms N and the single-atom cooperativity C :

$$C = \frac{4g_0^2}{\kappa\gamma} \quad (7.1)$$

Where γ is the atomic decay rate, and κ is the power¹ decay rate of the optical cavity, and g_0 is the single atom-cavity coupling rate which describes the rate of energy/information is exchanged between a single atom and a single photon in the cavity mode [79]:

$$g_0 = \sqrt{\frac{6c^3\gamma\omega_c}{w_0^2\ell\omega_a^3}} \quad (7.2)$$

Where c is the speed of light, ω_c is the cavity resonant angular frequency, w_0 is the cavity waist radius (see cavity equations in 5.2), ℓ is the cavity mirror spacing, and ω_a is the atomic resonance angular frequency. The physical interpretation of the single-atom cooperativity C is the fraction of photons emitted by an excited atom (in free space) into the solid angle of the optical cavity mode multiplied by the number of round-trips $F/2\pi$. The collective strong coupling regime is entered when $NC > 1$, so the desired coherent interaction is stronger than the geometric mean of the other dissipation rates.

The effective coupled atom number N in the cavity depends on the atomic cloud overlap with the cavity mode volume, the distribution of atoms along the standing wave (assuming a linear cavity architecture), and their temperature along the cavity axis. The atom-cavity coupling rate varies from zero to $\pm g_0$ at the center of an anti-node, so calculating the effective coupled atom number can be difficult, and fluorescence imaging can only give a rough estimate. Fortunately, there is a way to measure the coupled atoms using normal mode splitting.

Normal mode splitting (NMS) is the simplest phenomena expressed in a CQED system where the interaction between photons and atoms causes a splitting of the cavity resonance [81]. This splitting has a simple relationship quantified by the collective vacuum Rabi frequency:

$$\Omega_N = 2g_0\sqrt{N} \quad (7.3)$$

Since g_0 is known from other measurable quantities, by measuring Ω_N , a precise value for coupled atom number can be inferred, and we do this experimentally in chapter 8. However, it does not reveal information about the

¹Not to be confused with the electric field decay rate used in [80]

temperature of the cloud, and for now, we assume the Doppler width is much smaller than other dephasing rates.

This splitting is symmetric and centered around the atomic resonance only when the cavity offset relative to the atomic transition, $\Delta_{ca} = \omega_c - \omega_a$, equals zero. For non-zero values, the splitting is perturbed, leading to the commonly known picture of the avoided mode crossing shown in the bottom right of figure 7.1. As a function of laser-atomic frequency detuning, $\Delta_a = \omega - \omega_a$, the cavity transmission shows peaks at the locations traced by the dotted lines shown in the lower right panel of 7.1:

$$\Delta_{a,\pm} = (\Delta_{ca} \pm \sqrt{\Delta_{ca}^2 + \Omega_N^2})/2 \quad (7.4)$$

Diverging from the literature slightly, we opt to represent future avoided mode crossing figures with a different axis convention that is better suited for our purposes, shown in the bottom left of figure 7.1. In the experimental work presented in chapter 8, we are mostly interested in the case where the empty cavity is locked to the laser, $\Delta_c = 0$, close to the atomic resonance of $^1S_0 \rightarrow ^3P_1$ transition. The line that represents $\Delta_c = 0$ in the conventional axis is the diagonal line $\Delta_{ca} = \Delta_a$, but a horizontal line in our new axis. Additionally, the only variable parameter is Δ_a , so it makes sense to put this on the x -axis. This change in axis constitutes a shear in x followed by a 90° anti-clockwise rotation, seen by comparing the lower panels in figure 7.1.

In the new axis, the normal mode peaks are now represented by a single solution equation shown by the dashed line in the lower left panel of figure 7.1:

$$\Delta_{c, \text{peak}} = \Delta_a - \frac{Ng^2\Delta_a}{\Delta_a^2 + \frac{\gamma^2}{4}} \quad (7.5)$$

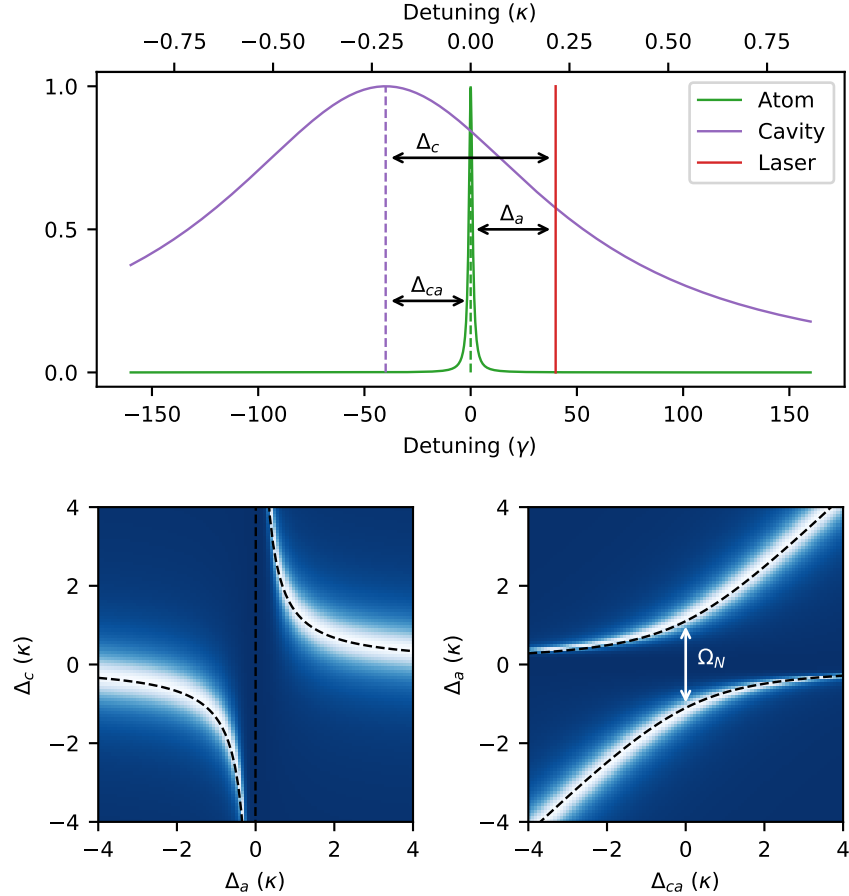


Figure 7.1: **Normal Mode Splitting and Axis Convention in Units of κ .** (Top) The cavity, laser and atomic frequency offsets are shown together with cavity and atomic linewidth matching those from the pulsed machine. (Bottom) A comparison between the two avoided mode crossing representations where bright blue is high transmission, and dark blue is low transmission. (Bottom left) Avoided mode crossing with $\Delta_c(\Delta_a)$ on the $y(x)$ -axis. (Bottom right) The same avoided mode crossing plotted with $\Delta_a(\Delta_{ca})$ on $y(x)$ -axis that is found more frequently in the literature.

7.2 Saturation Induced Bi-stability

Until now, we have only considered the low saturation limit where the circulating intra-cavity power is low compared to the saturation intensity of the atomic transition. In this case and for large normal mode splitting, power is rejected from entering the cavity at atomic resonance, as can be seen in figure 7.1 where there is *almost* zero transmission for $\Delta_a = \Delta_c = 0$. However, zero transmission is not truly zero since the wings of the normal modes allow a small fraction of light to leak into the cavity. This small fraction is typically scattered by the atoms. However, if this power is enough to saturate the atoms, the atomic ensemble is *bleached*, and the normal mode splitting is destroyed, suddenly yielding full transmission. This is the nature of the saturation induced bi-stability regime where two stable solutions exist based on the same cavity input power 1) nearly full cavity transmission if the atoms are saturated, or 2) nearly full reflection if the atoms are not saturated. Which of the two stable solutions for the intra-cavity field is realized during a scan of parameters (input power, atom detuning, atom number, etc.) depends on the history of the system.

Figure 7.2 plots the cavity transmission relative to increasing input power. On the x-axis, we plot both the cavity pump rate η in units of κ , and also the saturation parameter s :

$$\eta = \sqrt{\frac{2\pi P_0 \kappa}{\hbar\omega}} \quad (7.6)$$

$$s = \frac{\eta^2}{\kappa^2} s_1 \quad (7.7)$$

Where P_0 is the bare cavity input power assuming no losses and s_1 is the saturation parameter for a single intra-cavity photon $s_1 = 8g_0^2/\gamma^2$. We plot both values because s links better to the equations that define the bi-stability boundaries and scales linearly with power; however, it is not technically correct to use this parameter because the atom saturation depends on the intra-cavity power, which depends on the history and dynamics of the system. Therefore, we also plot η because this is frequently used in the literature and is the input parameter pumping the cavity. The cavity transmission at $\Delta_a = \Delta_c = 0$ enters a bi-stable regime when the cavity pump satisfies the inequality $s_- < s < s_+$ illustrated by the shaded region where $s_- = CN(1 + \sqrt{3/2})$ and $s_+ = (CN)^2/16$ [80]. Inside this region allows two stable solutions (solid line)

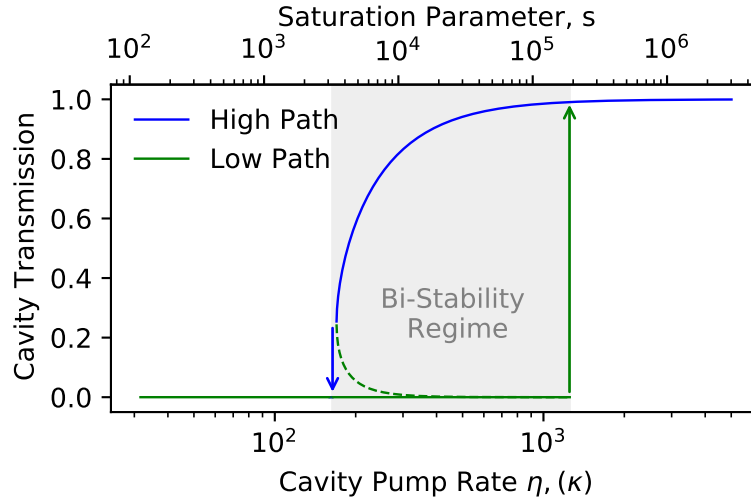


Figure 7.2: **Bi-Stability.** Using relevant parameters for the beam machine (see table C.1) and $3 \cdot 10^6$ coupled atoms, the solutions to the cavity transmission are shown, and the region with multiple intra-cavity solutions is bound by a grey box. This phenomenon was first experimentally shown in [82].

and one unstable solution (dashed line) (figure 7.2). The unstable solution is dynamically unstable, so it is unlikely to be realized as a steady-state solution in a real system with noise. Still, we include it for completeness here and in future plots.

The bi-stability regime physically expresses itself as hysteresis. When the cavity pump rate starts below s_- and ramps up, the low transmission solution is taken (denoted Low Path) up until s_+ where the system jumps to the high transmission solution indicated by the arrow. The same in reverse; if the cavity pump rate starts high (denoted High Path) and the atoms are saturated, decreasing the power until below s_- causes the cavity transmission to drop low.

We follow an analytical model presented by Rivero et. al. [80] to find the solutions for the complex intra-cavity field in the bi-stable regime so we can extract both transmission and phase for the bi-stability regime and also extract these values for various Δ_a and Δ_c . The model starts from a Dicke Hamiltonian for N atoms interacting with two counter-propagating modes

in a ring-cavity²:

$$\begin{aligned}\hat{H} &= \hat{H}_{\text{field}} + \hat{H}_{\text{pump}} + \sum_{j=1}^N \left(\hat{H}_{\text{atom}}^{(j)} + \hat{H}_{\text{atom:field}}^{(j)} \right) \quad (7.8) \\ \hat{H}_{\text{field}} &= -\sum_{\pm} \Delta_c \hat{a}_{\pm}^{\dagger} \hat{a}_{\pm} \\ \hat{H}_{\text{pump}} &= -\sum_{\pm} i\eta_{\pm} \left(\hat{a}_{\pm} - \hat{a}_{\pm}^{\dagger} \right) \\ \hat{H}_{\text{atom}}^{(j)} &= -\Delta_a \hat{\sigma}_j^+ \hat{\sigma}_j^- \\ \hat{H}_{\text{atom:field}}^{(j)} &= g \sum_{\pm} \left(\hat{a}_{\pm} \hat{\sigma}_j^+ e^{\pm ikz_j} + \hat{a}_{\pm}^{\dagger} \hat{\sigma}_j^- e^{\mp ikz_j} \right)\end{aligned}$$

Here, $\hat{a}_{\pm}^{\dagger}, \hat{a}_{\pm}$ are the photon field operators, and $\hat{\sigma}_j^+, \hat{\sigma}_j^-, \hat{\sigma}_j^z$ are the Pauli matrices applied to the j -th atom. Separating the cavity field \hat{a}_{\pm} and pump directions η_{\pm} into forward and backward direction \pm is unique to a ring cavity, and the assumption is made later that the cavity is only driven from one side. In a linear cavity, both directions are pumped equally (assuming identical mirrors), and the freedom to choose between pump directions does not exist. We will discuss the validity of applying a model based on a ring cavity to a linear cavity system later.

The only dephasing rates included are the atomic decay rate $\hat{\sigma}_j^- : \gamma$ and cavity field decay rate $\hat{a}_{\pm} : \kappa$. The full stationary solutions and assumptions are detailed in [80]. We arrive at a complex cavity field amplitude taking the mean field which depends on several parameters:

$$\langle \hat{a} \rangle = a(\eta, N, \Delta_c, \Delta_a) \quad (7.9)$$

We use this to define proxies for the complex cavity transmission T and phase θ using the equations:

$$T = \text{mod}(a) \quad (7.10)$$

$$\theta = \text{arg}(a) \quad (7.11)$$

²We discuss the validity of applying a model based on a ring-cavity to a linear cavity in section 8.4.1.

With this model, figure 7.3 shows the avoided mode crossing figures where the cavity pump rate is increased over the bi-stability regime. A transmission window emerges as the cavity pump rate rises, increasing in width until the atoms are saturated so much that their presence is washed out at $\eta = 5000 \kappa$. The subsequent rows show cavity transmission and cavity phase for the two different paths in the detuning parameter space, $\Delta_c = 0$ for the second and third rows, $\Delta_c = \Delta_a$ for the fourth and fifth rows. The reader should be familiar with the NMS shown in the fourth row. The emergence of a central peak and eventual morphing into one peak through saturation has been explored in [80].

For chapter 8, we are interested in the cross-section $\Delta_c = 0$, which represents the cavity locked to the laser and sweeping the laser over atomic resonance. The individual normal modes are not visible in this choice of detuning path, but their contribution is still seen as a wide dip in transmission. At the center of the dip, the same saturated peak emerges by increasing the cavity pump rate. The spectral width of the saturated peak follows [80]:

$$|\Delta_{a,\text{sat}}| = \frac{1}{2} \sqrt{\frac{\Omega_\eta^2}{2} - \frac{\gamma^2 CN}{4}} \quad (7.12)$$

Here, Ω_η is a Rabi frequency analogous in form to the normal mode splitting, but the number of atoms is replaced by the number of intra-cavity photons for a bare cavity n .

$$\Omega_\eta = \frac{2g_0\eta}{\kappa} = 2g_0\sqrt{n} \quad (7.13)$$

The phase exhibits a π -step at atomic resonance at $\eta = 25 \kappa$, which is likely inaccessible due to no cavity transmission. However, with a larger cavity pump rate, the saturation-induced transmission window emerges with multiple solutions for the transmission and phase close to $\Delta_a = 0$. The model does not give any insight into which solution is taken by the cavity transmission, but this is investigated experimentally in chapter 8.

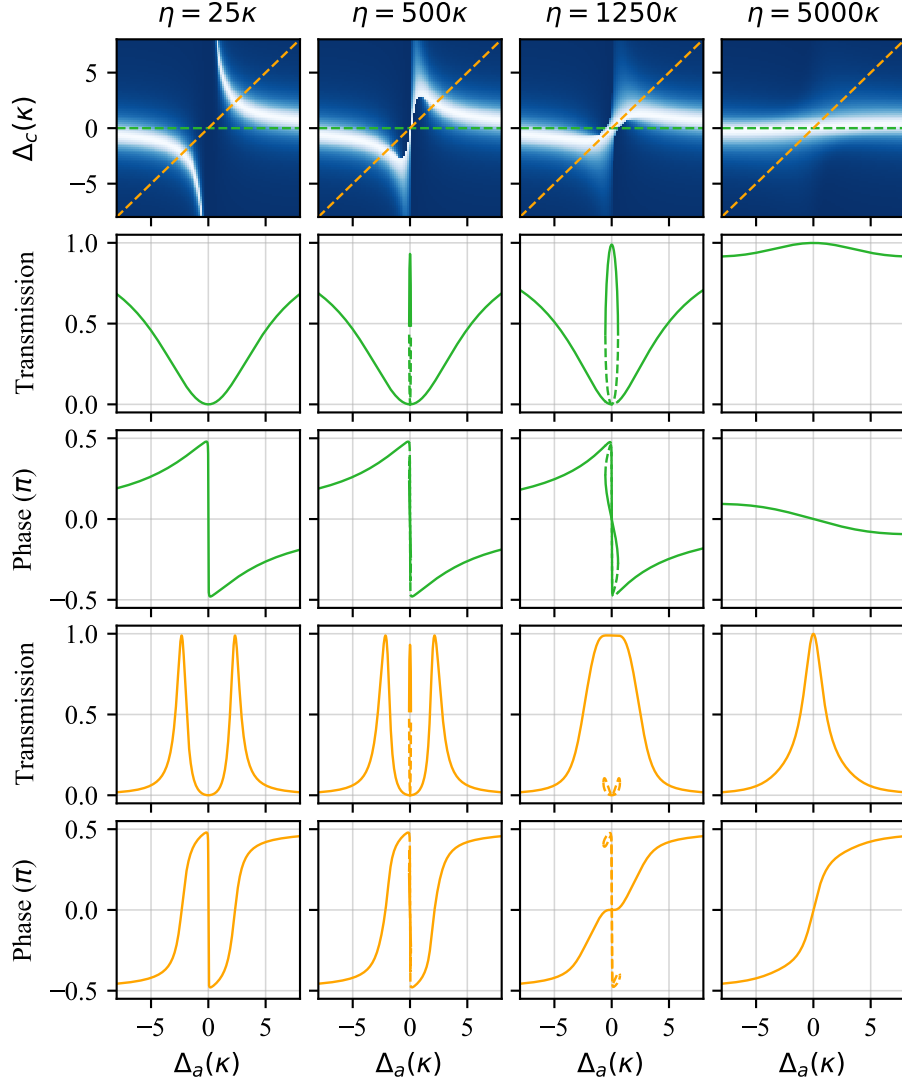


Figure 7.3: **NMS Unsaturated to Saturated Cross-over in Units of κ .** For a coupled atom number of 3 million, four rows are shown for different cavity pumping rates, $\eta = 25, 500, 1250, 5000 \kappa$. The left column shows the transmission for Δ_a vs Δ_c , where bright/white is high transmission. The horizontal dashed line in green represents the laser-cavity locked scan, and the transmission and phase are plotted in the 2nd and 3rd rows. The diagonal line in yellow represents the laser tuned while cavity locked to atomic resonance $\Delta_{ca} = 0$, and transmission and phase are plotted in rows 4 and 5.

7.3 Driven CQED Enhanced Clocks

The bi-stable regime was first studied in 1976 as a possible all-optical logic gate [83] because the cavity has memory of its previous state. In an atomic-cavity system, the memory of these gates is short-lived due to the atom or cavity lifetime. The saturation window is usually suppressed in the good-cavity limit, where the atomic decay rate is much larger than the cavity decay rate due to strong resonant atomic absorption; however, when the atomic linewidth is narrower than the cavity decay rate the saturation window becomes visible (as seen in figure 7.3) and this regime is known as the bad-cavity limit, $\kappa \gg \gamma$.

The extreme non-linearity exhibited by these atom-cavity systems is typically very sensitive to initial conditions. A system that produces a strong response to a small change in input parameters sounds like an excellent frequency discriminator, provided that the non-linearity is centered or triggered by the atomic resonance. In reference [19], a study is made on an ensemble of atoms trapped in the motional ground state of an optical lattice inside a cavity, and they show that quantum bi-stability exists for a certain range of cavity input laser powers. Driving the cavity at input powers above the bi-stability regime, they anticipate state-of-the-art achievable shot-noise limited linewidths of mHz to μ Hz at 1 Hz integration time based on achievable atom numbers and cavity finesse in standard CQED experiments. They note that the best operation would be inside the bi-stability region, but here, the signal would not be stable enough to use as an error signal for a frequency reference due to hysteresis.

Tieri et al. [84] build on Martin et al. [19], and the simulations are taken further to incorporate Doppler broadening, which lifts the bi-stability condition and allows all cavity input laser powers to be used while maintaining excellent linewidth capabilities. The remaining narrow feature is fully described by saturated spectroscopy, and a CQED consideration is no longer required. This leads to the conclusion that large atomic temperatures (temperatures corresponding to Doppler widths much greater than the atomic transition linewidth, $\Gamma_D \gg \gamma$) are necessary to navigate the bi-stability and to achieve a state-of-the-art ultra-coherent laser based on a saturated feature. The paper suggests that for certain regimes, there may not be a need for sub- μ K atomic temperatures achieved in optical lattices, contrary to the current direction of the state-of-the-art atomic clocks extremely low tem-

perature clouds are used to load optical lattices to reach the Lamb-Dicke regime.

Barberena et. al. [20] rigorously conclude a driven CQED system based on a high collective-cooperativity in the bad cavity regime could be competitive with the limits of a super-radiant laser. They consider both quadratures of the optical light field exiting the optical cavity and include the effects of frequency measurement and feedback on the system.

7.4 Conclusion

We have presented a basic introduction to the driven CQED system that will be experimentally explored in chapter 8. We start with a mean-field description that can describe the overall features of saturation-induced transparency and bi-stability. We take specific care in identifying and presenting the unconventional choice of tuning Δ_a while keeping $\Delta_c = 0$, but it is important to help understand the work in the next chapter.

A macroscopic model that explains what is happening at the atomic level and the role of collective phenomena is still lacking. Additionally, further work to understand the nature of the π -step in phase is required to understand what parameters it depends on. We leave this to future work.

Chapter 8

Exploring the Bi-stability Regime with Quadrature Detection

The degrees of freedom for improving the performance of a frequency standard are increasing the atom number N , reducing the atom cloud temperature Γ_D , and surrounding the atoms by an optical cavity to increase the interaction length by the finesse. Improving all these metrics at once is met with new limitations, such as bi-stability that hinders stable clock operation. To explore the bi-stable regime and generate an error signal for stabilizing a clock laser, we *emulate* continuous spectroscopy on a pulsed Sr machine by dropping a cloud of atoms through the cavity mode and observing the atom-cavity dynamics in a timescale where the atom cloud is quasi-stationary in the cavity. We also employ a versatile variation of NICE-OHMS detection where one of the sidebands is resonant with the atoms instead of the carrier, which retrieves a large signal-to-noise and allows both quadratures of the light field to be measured to capture more information about the atom-cavity dynamics.

We extract key parameters from the data that make a link to the metrological potential of this system as a frequency reference.

8.1 Overview

The pulsed experiment used here has produced results in 2023 and 2024 on the study of quasi-continuous superradiant lasing on the $^1S_0 \rightarrow ^3P_1$ transition [21], and a study of super-radiance enhanced Ramsey spectroscopy [85]. In-depth details about the experiment are given in the PhD theses of Sofus L. Kristensen [86] and Eliot Bohr [71]; however, the measurement scheme utilized in this chapter is unique compared to prior work on the pulsed machine, and a summary is illustrated in figure 8.1. A cloud of ^{88}Sr atoms cooled and trapped in a 689 nm narrow-band MOT prepares up to 50 million atoms at several μK temperatures. This cloud of atoms is positioned just above the mode of an optical cavity. Once the MOT trapping light is turned off, the atoms free-fall through the cavity.

Laser light stabilized to a ULE cavity is used to probe the cavity. The laser noise and drift in frequency are on a scale much smaller than the dominant rates of the atom-cavity, such as γ and κ . The probing light polarization is aligned along the quantization axis defined by a small bias magnetic field B generated by a pair of Helmholtz coils. We change the laser frequency by tuning the frequency to the acousto-optical modulator, ω_{AOM} , providing direct control of Δ_a .

We opt for a measurement scheme that resembles NICE-OHMS (described in chapter 3) but differs because the carrier is detuned below atomic resonance by $-\omega_{\text{FSR}}/2\pi = 780 \text{ MHz}$. Instead, the +1 sideband probes the cavity close to atomic resonance; see figure 8.2. The EOM modulation frequency can differ from ω_{FSR} by ω_m depending on the use case, with more details in the following sections. Using this measurement scheme means the beat note is at a high frequency, so it can efficiently minimize common noise sources such as $1/f$ noise and electronics noise in the detection, and both real and complex parts of the beat note can be tracked, allowing reconstruction of the complex cavity transmission. We also have access to a large dynamic range of the sideband input powers, controlled by the rf-power driving the modulation into the EOM, equivalent to the cavity pump rate η . Additionally, η can be changed over a large range without sacrificing the size of the cavity-laser error-signal as the majority of this error-signal comes from the carrier. This remains true as long as the carrier is not depleted i.e. for modulation index β below 1.5. This modulation index is not exceeded in this work.

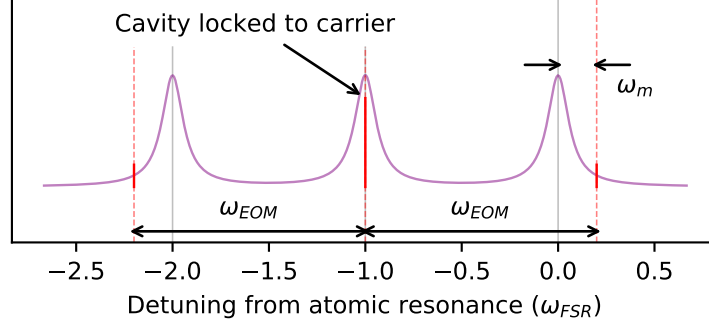


Figure 8.2: **Generalized Measurement Scheme.** The optical triplet are generated with a frequency $\omega_{EOM} = \omega_{FSR} + \omega_m$ and the blue sideband is close to resonance with the $^1S_0 \rightarrow ^3P_1$ transition. This figure is important for figures 6.5 and 8.7.

Like NICE-OHMS, two beat signals are detected on the fast photodetector with the same frequency, one from the left optical pair and one from the right optical pair. Without the presence of atoms and avoiding the situation where $\Delta_c = \omega_c - \omega_L \neq 0$, achieved by stabilizing the cavity to the laser¹, and simultaneously $\omega_m \neq 0$, no resulting beat note is detected. We represent the resultant beat note in the photocurrent as a complex phasor C . In the case of an empty cavity:

$$C(N=0) = t_{FP}(\Delta_c) t_{FP}^*(\Delta_c - \omega_m) - t_{FP}^*(\Delta_c) t_{FP}(\Delta_c + \omega_m) \quad (8.1)$$

Where the Fabry-Pérot complex amplitude transmission coefficient t_{FP} is:

$$t_{FP}(\Delta_c) = 1 - \frac{\Delta_c(\Delta_c + i\kappa/2)}{(\kappa/2)^2 + (\Delta_c)^2} \quad (8.2)$$

The beat becomes non-zero when atoms perturb the +1 sideband. We replace the bare cavity amplitude transmission coefficient with the complex cavity amplitude from the analytical solution to the Dicke model a , which

¹We note that now there is ambiguity in the definition of the laser frequency ω_L since there is a frequency triplet. So we rely on $\omega_{EOM} \approx \omega_{FSR}$ and the periodicity of the cavity modes to use the same Δ_c for all three lasers.

depends on the cavity pump rate η , coupled atom number N , cavity-laser detuning Δ_c , and atom-laser detuning Δ_a :

$$C(N > 0) = t_{FP}(\Delta_c) t_{FP}^*(\Delta_c - \omega_m) - t_{FP}^*(\Delta_c) a(\eta, N, \Delta_c + \omega_m, \Delta_a) \quad (8.3)$$

We note that for no atoms in the cavity $N = 0$, $a(\eta, 0, \Delta_c + \omega_m, \Delta_a) = t_{FP}(\Delta_c + \omega_m)$. A detector with high bandwidth measures the phasor at the beat frequency $\omega_{EOM} = \omega_{FSR} + \omega_m$. The beat note in the photocurrent i_{PD} is proportional to the sum of the real $\Re\{C\}$ and imaginary $\Im\{C\}$ parts of C :

$$\begin{aligned} i_{PD} \propto & 2J_0 J_1 \Re\{C\} \cos(\omega_{FSR} + \omega_m) \\ & + 2J_0 J_1 \Im\{C\} \sin(\omega_{FSR} + \omega_m) \end{aligned} \quad (8.4)$$

Where J_0 and J_1 are the Bessel function coefficients of the first kind. Through standard I-Q detection scheme shown in figure 8.1, we define I and Q with a global phase rotation θ_0 and additional scaling factor A_1 :

$$\begin{aligned} I &= A_1 2J_0 J_1 \Re\{C\} e^{i\theta_0} \\ Q &= A_1 2J_0 J_1 \Im\{C\} e^{i\theta_0} \end{aligned} \quad (8.5)$$

This global phase is a random but constant value that comes from the difference in path lengths between source to mixer and source to EOM. Finding $\theta_0 = 0$ is not straightforward but also not necessary because it falls out of the equation for amplitude and is a constant offset in the argument:

$$(I + iQ)/2J_0 J_1 A_1 = C e^{i\theta_0} \quad (8.6)$$

We use this general derivation for the measurement scheme for our atom-cavity system for the rest of this chapter. Next, we quantify the EOM driving power and how it relates to η , J_0 , and J_1 in the next section.

8.1.1 Modulation Index Calibration

The Jenoptik EOM producing the sidebands for the optical triplet is driven by a home built DDS board and minicircuits RF amplifier. The DDS control

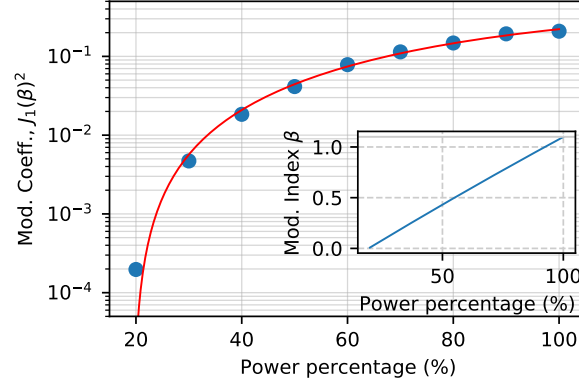


Figure 8.3: **DDS Output RF Power Units Calibrated to Sideband Modulation Index Beta.** The arbitrary unit of power percentage is calibrated to the measured dotted points by fitting a 2nd order polynomial. The resulting fit is plotted with the bold line, and also shown again in the inset. The fit is only required to be 2nd order and not 1st order to capture the value for power percentage of 20%.

software can change the DDS output power based on an input value quantified in arbitrary units of percent. We measure the power percentage that corresponds to the modulation index, β , and plot the fit in figure 8.3.

The sideband power is measured by detuning the EOM frequency by more than two times the cavity FWHM so during a piezo sweep of the cavity, the sidebands are no longer overlapped and can be resolved individually. A peak finding code identifies the peak voltage. With the voltage-to-power conversion of the photodetector, we can deduce the power in the sideband and the carrier for a given DDS input value.

For a total cavity input power of $10 \mu\text{W}$, we can choose a sideband power anywhere between $2 \mu\text{W}$ to 2nW .

8.2 Finding the Turning Point of a Falling Atom Cloud

As detailed in chapter 7, the lower power threshold for bi-stability scales with the collective cooperativity linearly and upper threshold scales quadratically, and since we are dropping a cloud of atoms through the cavity, the effective number of coupled atoms changes rapidly on a 10-millisecond timescale. The aim of this section is to:

1. quantify the effective number of coupled atoms over time $\Omega_N(t)$,
2. quantify the spread of atom number between individual MOT realizations,
3. motivate a region with minimum atom number variation for a laser-cavity sweep to emulate steady state dynamics.

We employ a technique that, in hindsight, is similar to a method used in [87] where the normal modes are tracked by an off-cavity-resonance sideband. Figure 8.4 shows this measurement's optical triplet configuration relative to the modes of the bare cavity. In the presence of atoms, the cavity mode is split due to normal mode splitting, which perturbs the blue sideband. The requirements for a reliable measurement are that the normal-mode splitting is on the order of the cavity linewidth κ , and the sideband power is low to avoid saturating and heating the atoms during their cavity transit. The cavity lock is maintained by the carrier and ensures the cavity resonance is locked to atomic resonance, so $\Delta_{ca} = 0$.

The total probing power is $8.6 \mu\text{W}$ and 14 nW is modulated into each sideband. The EOM drive frequency is set to $\omega_m = 1.12\kappa = +0.9 \text{ MHz}$. The red MOT is filled above the cavity (as shown in figure 8.1) and at $t = -2 \text{ ms}$, the red MOT light is switched off and the cloud is dropped through the cavity mode. Figure 8.5 shows I and Q during an atom cloud transit. At $t = 0 \text{ ms}$, I and Q are non-zero, meaning there are already some atoms in the cavity.

We opt to only fit the in-phase signal I and the resulting fit parameters are used to infer Q and a good agreement can be seen by eye. We model the change in coupled atoms with a simple Gaussian with peak atom number N_{peak} , with the time of peak atom number t_{peak} , and Gaussian full-width at half-maximum w_{FWHM} , namely:

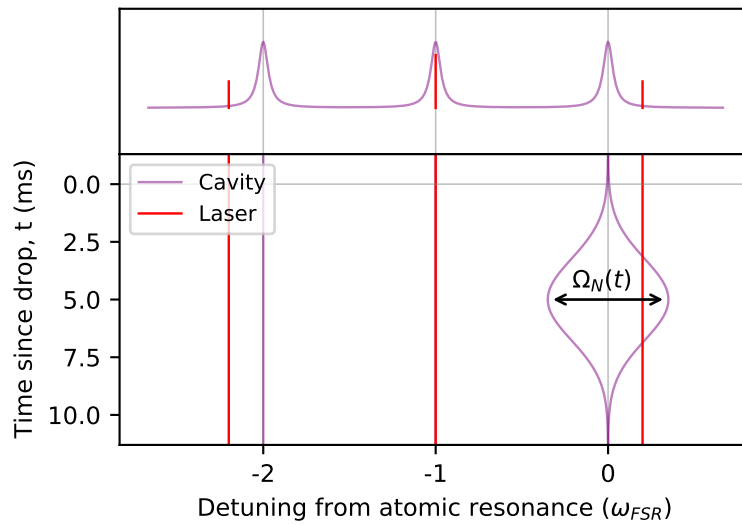


Figure 8.4: **Atom Number Measurement Scheme.** Like the scheme seen in figure 8.2, an optical triplet is produced, where now the EOM drive frequency is slightly higher than the cavity FSR, and the sideband near-resonant to the atoms will be sensitive to the splitting of the dressed cavity modes without excessive heating because the interaction is off-resonance. The sideband power is enlarged for clarity, but the actual power in the sideband is close to $1/1000$ the power in the carrier.

$$N(t) = N_{\text{peak}} \exp \left\{ - \left(\frac{t - t_{\text{peak}}}{w_{\text{FWHM}}} \right)^2 \right\} \quad (8.7)$$

The resulting beat note can be represented as a phasor from equation 8.3, and simplified for $\Delta_{ca} = 0$ so $\Delta_c = \Delta_a$ to:

$$C = t_{FP}^*(-\omega_m) - a(\eta, N(t), \Delta_c = \omega_m, \Delta_a = \omega_m) \quad (8.8)$$

We can use the analytical Dicke model here because we are at very low cavity pump rates so saturation-induced bi-stability is not expected or observed. We then only further fit the scaling factor A_1 and global phase θ_0 as in equation 8.5 and repeated here:

$$I = A_1 2J_0 J_1 \Re\{C\} e^{i\theta_0} \quad (8.9)$$

In total, only five fitting parameters are used to describe the entire data, which it does very well as seen by the data and fit line perfectly overlapping in figure 8.5, except for the top of the quadrature signal, which is not fully understood. This fit quality is also reflected in the many other traces taken but not pictured. We do not fit any arbitrary offsets because this can over or underestimate the peak atom number, but there might be a small offset present due to an imbalance in the sidebands.

A well-chosen value for $\theta_0 \approx 0$ a priori means the I and Q signals closely resemble the real $\Re\{C\}$ and imaginary $\Im\{C\}$ parts of C , and can also be understood as relating to the transmissive and dispersive parts of the atom-cavity transfer function. The maximum transmission arises when the vacuum Rabi frequency has shifted the cavity resonance directly onto the sideband, $\Omega_N/2 = 1.15 \kappa$, equivalent to $1.07 \cdot 10^6$ atoms, as indicated by the horizontal and vertical lines. This also aligns with the region with the largest gradient in dispersion.

With this method of tracking the atom number, we take statistics over 30 individual MOT realizations for constant experimental parameters in figure 8.6. There is a spread of coupled atom trajectories in the cavity between MOT realizations where the peak atom number is found to be $1.51(11) \cdot 10^6$ atoms. We find an interesting correlation between the time of peak atom number and peak atom number indicated by the green circles labeled as peaks in figure 8.6. This means that the more atoms that are loaded into the red MOT, the more the centre of mass changes, such that the peak atom number arrives later. We know that the atoms are so cold that they sag due

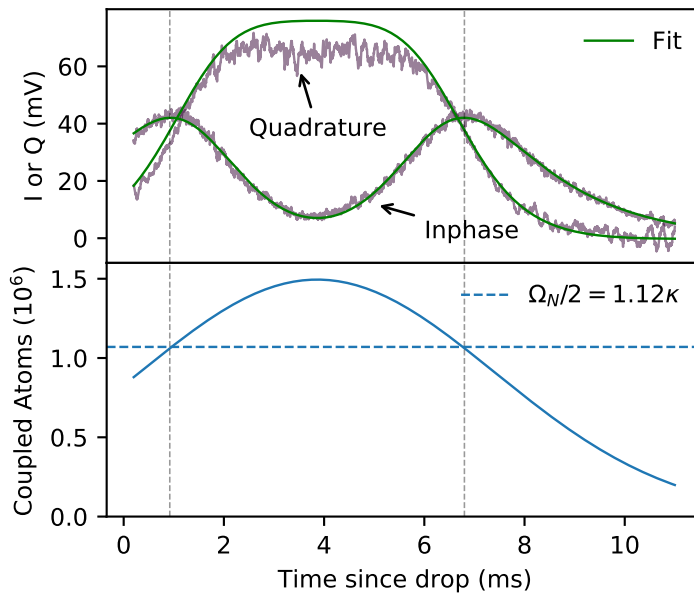


Figure 8.5: **Tracking Coupled Atom Number.** (Top) The inphase I and quadrature Q are plotted for the transit of an atom cloud through the cavity. The fit is shown against the data, although is only applied to I and Q is inferred from the fitting parameters. (Bottom) The corresponding atom number is represented as a Gaussian profile. The model fit is very good, and the signal-to-noise is high (data is from a single realization), supporting the strength of this measurement technique.

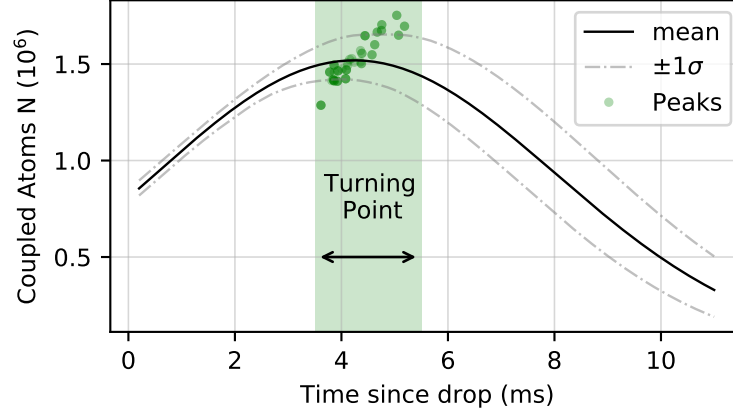


Figure 8.6: **Atom Number Analysis.** The distribution of atom trajectories through the cavity mode in terms of effective coupled atoms and the boundaries are defined by percentile corresponding to $\pm 1\sigma$. The mean peak atom number is 1.51(11) million atoms. The peak atom number and time of peak atom number show a clear linear correlation. The turning point indicates a promising quasi-stable region to perform the sweep illustrated in figure 8.7.

to gravity into a crescent shape in a single-frequency red MOT, as pictured in figure 8.1. It could be that we see the atoms stacking on themselves, and this structure prevails after the red MOT has been switched off and the atom cloud has dropped. This is just speculation for now. The atom number Gaussian FWHM $w_{\text{FWHM}} = 7.0(3)$ ms.

From figure 8.6 we can identify a region around 4 and 6 ms that has the turning point of the average MOT realization, however, this region also the largest spread in atom number between MOT realization. We account for this by taking 10 traces, one for each MOT realization. This will reveal if any dominant features come from the peak atomic number fluctuations².

²It appears that the peak atom number fluctuation does not dominate the phenomena studied later in the chapter.

8.3 Exploring Bi-stability for Different Cavity Pump Rates

Switching to an EOM drive rf-frequency equal to the ω_{FSR} so $\omega_m = 0$, we scan the laser over atomic resonance in the 4 to 6 ms region as identified in figure 8.6 at the coupled atom number turning point. The sweep across resonance is done with a saw-tooth wavefunction, shown in figure 8.7. The atomic cloud is dropped at $t = -4$ ms, and the EOM drive is switched on at $t = 0$ ms, while at the same time starting to sweep the laser Δ_a by ω_s while the cavity follows, trying to keep $\Delta_c = 0$.

The cavity has only a finite servo bandwidth to follow the laser, so there will be a lag, as illustrated in figure 8.7. To characterize the extent of this cavity lag, we monitor the error signal during a sweep and calibrate it to the cavity linewidth. The results are plotted in figure 8.8. There is a significant oscillation, likely to be the piezo resonance frequency, and a clear offset between the zero-lock point, which switches signs depending on the scan direction. This is expected without a feed-forward signal. A constant offset on Δ_c that flips sign based on the direction of tuning has the effect of a forward and backward scan forming a loop in the $\Delta_c(\Delta_a)$ plot, shown as an inset in figure 8.8. Since the change in $\Delta_c < \omega_s/50$, in other words, the loop area is very small, we will treat it as negligible for now but stay aware that asymmetry from forward and backward scans could be due to the small switching sign of Δ_c .

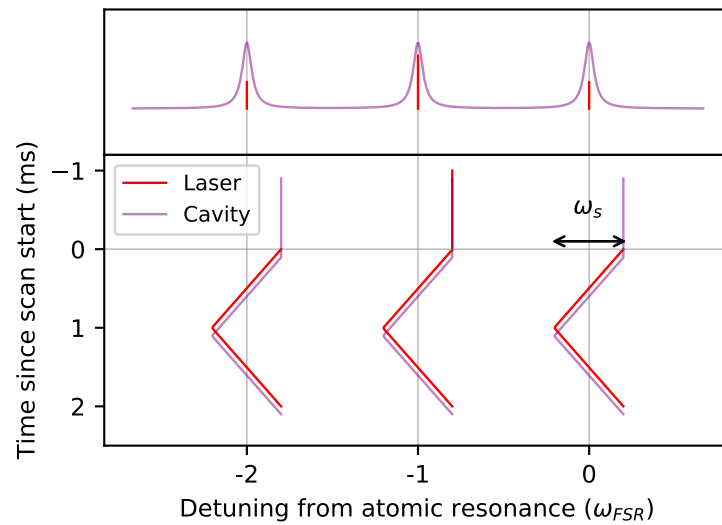


Figure 8.7: **Laser Sweep Measurement Scheme.** (Top) Optical triplet in red and bare cavity resonance in purple relative to atomic resonance. (Bottom) The laser sweep scheme going down then up in frequency is shown where the EOM drive is switched on at the same time as the sweep starts. The cavity lags behind the laser during the sawtooth sweep, which is illustrated here to first order as a constant offset, but studied in more detail in figure 8.8. The scan range is ω_s .

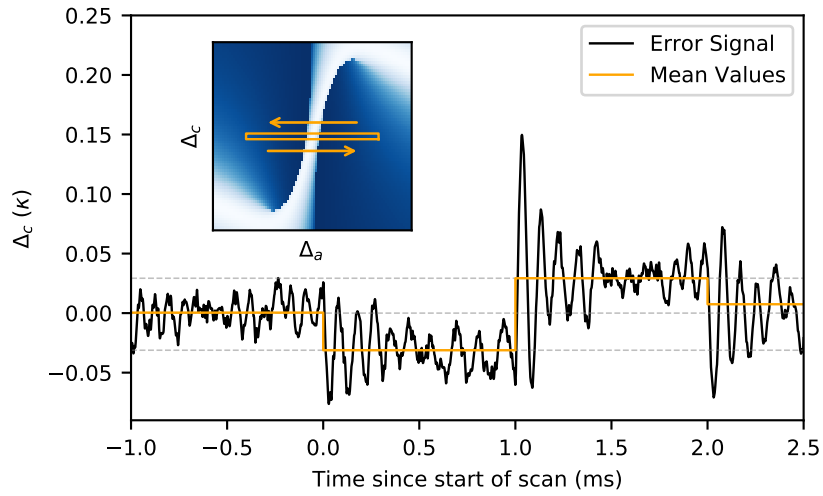


Figure 8.8: **Error Signal Dynamics During Sweep.** (Top) The error signal of the cavity lock is tracked during a forward and backward saw-tooth sweep illustrated in figure 8.7. The start and turn-around of the saw-tooth function at $t = 0$ ms and 1 ms are both lead with a kick to the error-signal. The mean value is plotted for each region of interest $t < 0$ ms, $0 < t < 1$ ms, $1 < t < 2$ ms and $t > 2$ ms and the same mean values are shown to trace a loop in the $\Delta_c(\Delta_a)$ inset plot.

8.3.1 Bi-stability Spectra

The MOT cloud is tuned to prepare a peak atom number of roughly $3 \cdot 10^6$ inside the cavity mode, placing the system comfortably in the strong collective coupling regime $CN = 1320 > 1$. This collective coupling number is in the ballpark of an achievable continuous beam machine [42].

The laser is frequency swept over atomic resonance by $w_s = 4\kappa$ where atomic resonance is roughly centered in the scan, first scanning down in frequency followed by up in frequency, taking in total 2 ms as shown in figure 8.7. This was the largest ω_s that could be used before the cavity lock started to become unstable. The resulting beat note can be represented as a phasor from equation 8.3, and simplified for $\Delta_c = 0$ and $\omega_m = 0$ to:

$$C = 1 - a(\eta, N, \Delta_c = 0, \Delta_a(t)) \quad (8.10)$$

This relates to I and Q by:

$$C = (I + iQ)e^{-i\theta_0}/J_0J_1A_1 \quad (8.11)$$

The phasor C currently has an offset in complex space, which is removable analytically, but considering the theme of this work is to look for an error signal to stabilize a laser, there needs to be a way to transform C into an error signal with electronics. This would require prior knowledge of the global phase and scaling factors. Therefore, we opt for plotting one minus the absolute or modulus of C , which drops θ_0 and the argument of C , which drops the scaling factors $J_0J_1A_1$:

$$\begin{aligned} 1 - |C| &= 1 - \sqrt{(I + iQ)(I - iQ)e^{-i\theta_0+i\theta_0}}/J_0J_1A_1 \\ &= 1 - \sqrt{(I^2 + Q^2)}/J_0J_1A_1 \end{aligned} \quad (8.12)$$

$$\begin{aligned} \arg(C) &= \arg((I + iQ)e^{-i\theta_0})/J_0J_1A_1 \\ &= \arg(I + iQ) - \theta_0 \end{aligned} \quad (8.13)$$

We can think of $1 - |C|$ as the transmission and $\arg(C)$ as the phase, but these are not exactly the same as the pure transmission and phase as in equations 7.10 and 7.11. The pure transmission and phase are wrapped up in the equations but can still be extracted; it just depends on what is more interesting to study.

The results for the argument and absolute of C are shown for a range of cavity pump rates between $\eta = 341\kappa$ and 1581κ in figure 8.9. This was the range where the most interesting dynamics were seen. The scan direction is indicated by an arrow on the first column, separating the first and second rows as down scans and the third and fourth rows as up scans.

A central saturation window can be seen gradually widening with increasing η . Studying the data reveals a rich amount of details. Finding a complete model to describe all aspects of the data, including quantum coherences and mechanical back-action, is outside the scope of this work, but a numerical model is under development for future work. However, the mean-field analytical model plotted with the data is successful at predicting the general features like saturated peak width, shape, and their dependence on power.

We now walk through several features of interest in figure 8.9. The model shown in column 1 ($\eta = 341\kappa$) exhibits a sharp feature that is not reflected in the data. This could be due to the sweep rate of $4000 \kappa \text{ s}^{-1}$ is faster than the time it takes the atoms to become saturated. For increasing η , especially for the down scan, the lobes in the phase are not symmetrical, which indicates that the atoms have not had time to saturate. Increasing η further recovers most of the symmetry.

The down and up scans have several asymmetries, and the origin could be a combination of different effects resulting in hysteresis. The primary difference between an up scan and a down scan is the order in which red-detuned and blue-detuned light interacts with the atoms. The flip in sign of the detuning flips the sign of the dipole force from attractive at the anti-nodes to repulsive. In the case of a low starting temperature below the temperature limit of cavity cooling determined by the linewidth of the cavity, and at high saturation, we anticipate that both blue and red detuned light will heat the atomic cloud. However, the dipole force will be significant due to the resonance enhancement of the light, possibly altering the center of mass motion of the atom cloud as it transits through the cavity. For example, if the dipole force acts to pin atoms at the anti-node sites, this could momentarily enhance the coupled atom number beyond that predicted in figure 8.6. Future work will investigate the heating of the atomic ensemble during a laser sweep. Since we chose to take the down and up scans consecutively, the atomic cloud is heated during the down scan, reducing the effective coupled atoms in the cavity for the up scan. If we estimate $1/5$ of the sweep to be the interaction time when the laser frequency is close to atomic resonance, then $200 \mu\text{s}$ heating corresponds to approximately ten recoils. This does not

consider heating from stimulated emission effects along the cavity axis, which might be larger, especially if the atom ensemble radiates collectively. However, looking back at figure 8.9, the same mean-field model is overlaid with the same coupled atom number for down and up scans, suggesting that loss of atoms due to heating is not the dominant effect altering the lineshape, compared to the cavity pump rate.

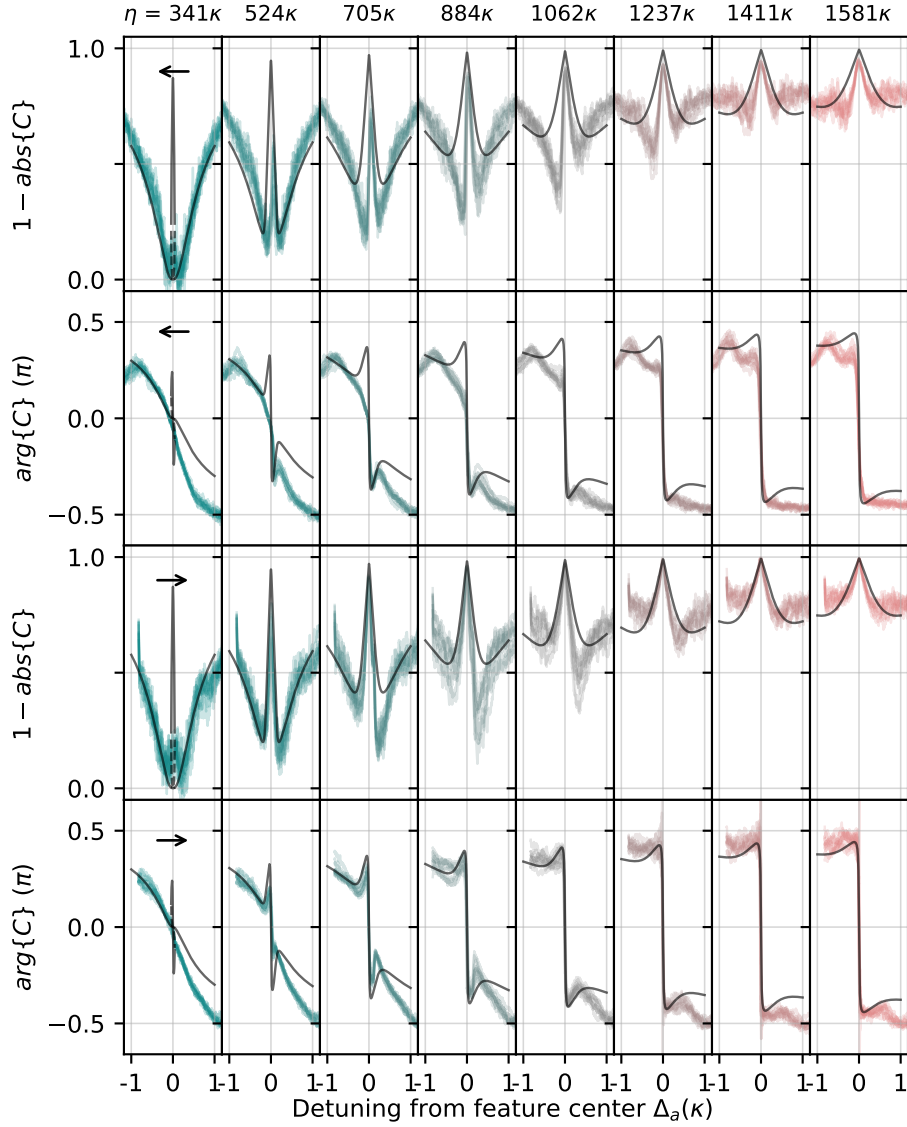


Figure 8.9: **Transmission and Phase vs Power for 3 Million Coupled Atoms.** Both absolute and argument of C are plotted for varying cavity pump rates. 10 traces are plotted for each pump rate, showing the reproducibility even with atom number fluctuations. The top two rows represent the down scan, and the bottom two row the up scan, also indicated by arrows on the first column. The black solid line is the mean-field model prediction fit by eye by *only* adjusting the atom-cavity coupling rate to $g_0/3$.

8.4 Quantitative Analysis

We now look closer at a single trace for the argument and magnitude of an up scan at $\eta = 1237$ in figure 8.10. We again plot the model prediction to show how well it predicts the gradient of the π -step in phase. The inset shows the spread of phase zero-crossings $\Delta_{a,0}$ and peak transmission crossings $\Delta_{a,\max}$ for all cavity pump rates above $\eta = 884\kappa$, i.e. 50 traces. The standard deviation of $\Delta_{a,0}$ is 1.9γ . The range of $\Delta_{a,0}$ between $\pm 5\gamma$ is larger than what can be attributed to noise because some traces make the π -step early or late, which is not well understood. We also note that the frequency scaling is extremely precise because it is determined by an AOM, but the frequency axis offset has been manually set to zero to the center of the saturation feature. This is fine if the shift is constant, as it can be accounted for, but further experimental investigations are required to verify the relation of zero to the natural atomic transition frequency.

Notably, $\Delta_{a,0}$ and $\Delta_{a,\max}$ correlate very well, indicating that the peak in transmission corresponds to the center of the π -step in phase. This is *not* the case for the down scan (not pictured), hinting at a fundamental difference between an up and down scan.

For now, we relax the obvious limitations of this atom-cavity system, such as heating and dynamics of the transiting atomic cloud as done in [19, 84, 51, 20], and quantify how well this signal could stabilize a laser as a frequency reference. We find an average gradient of $\delta\phi/\delta\nu = 0.037(8)$ rad \cdot kHz $^{-1}$, and sideband input power of $P_{\text{in}} = 179$ nW. Using equation 4.7 and written out again below, and a detection quantum efficiency of $\eta_D = 0.1$, we find a shot-noise limited linewidth after 1 s integration time of 25 mHz. This is an impressive value and consistent with the predictions in [19].

$$\Delta\nu = \frac{\pi}{2\eta_D P_{\text{in}} \left(\frac{\delta\phi}{\delta\nu}\right)^2} \quad (8.14)$$

Assuming that the only noise source comes from the shot-noise is a little unfair and we can estimate the performance in a different way using the stability equation 1.1. This allows us to incorporate the visible noise in the signal in figure 8.10. Although the step is slightly narrower, we conservatively estimate $\Delta\nu \approx 5\gamma/2\pi$, so $Q = 1.2 \cdot 10^{10}$. We estimate the SNR ≈ 5 because the fluctuations close to resonance appear to increase in size. The integration

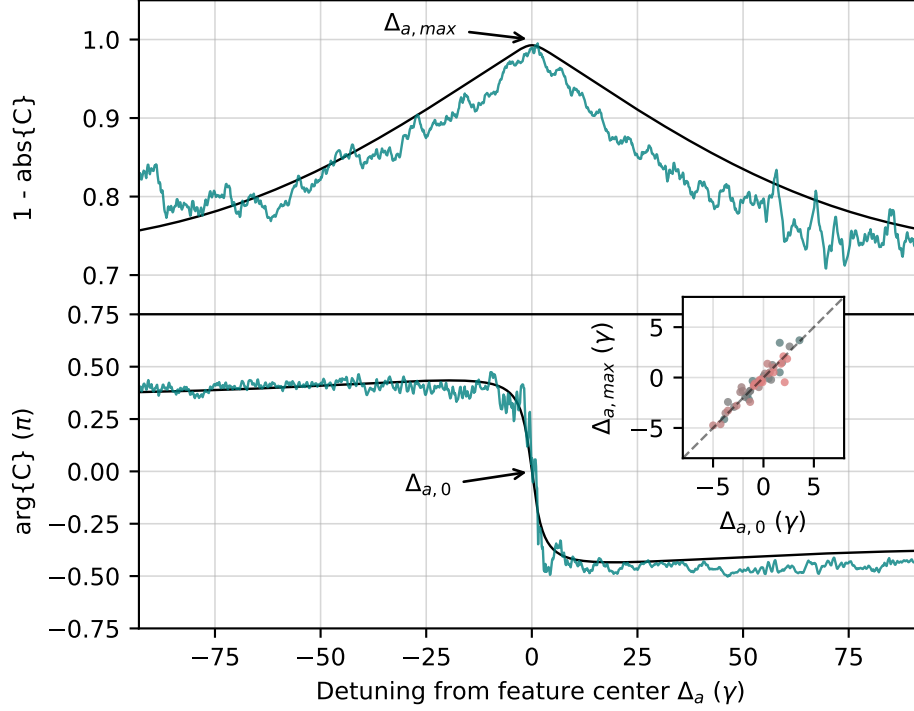


Figure 8.10: **Single Trace and Frequency Crossings in Units of γ .** A single trace for an up scan at $\eta = 1237\kappa$ is isolated from figure 8.9 to study the behaviour close to the saturation window. The inset shows the phase zero-crossings $\Delta_{a,0}$ and peak transmission crossings $\Delta_{a,max}$ plotted for 50 traces.

time is $5\ \mu\text{s}$, which takes into account the sampling rate³ of 200 kHz. This results in an estimated short-term clock stability of $3.7 \cdot 10^{-14} / \sqrt{\tau/1\ \text{s}}$ assuming continuous clock operation, comparable to similar schemes [39]. More work is required to demonstrate this stability practically and better understand the scaling and ultimate limits.

³We sample at 4 MHz but smooth with a nearest-neighbour filter where the closest 20 points are averaged to one point.

8.4.1 Discussion on the Validity of the Model

The mean-field model used here from [80] is based on a ring-cavity and only driven from one side. This differs in important ways to the setup and experiment shown above which is a linear cavity. Yet the model is surprisingly successful at describing the data, but only when the cavity coupling g_0 is divided by 3. If we can assume that this factor is not a consequence of physicist error by factors of 2 or π , there are a few physical differences between a linear and ring cavity that could account for the extra factor of 1/3. For an atom in a ring cavity, it will only see one photon per round trip, but a linear cavity sees two photons with opposite direction per round trip. This creates a standing wave in a linear cavity meaning the atom-cavity coupling differs from 0 to $\pm g_0$ depending on whether it is on a node or antinode, whereas a ring-cavity sees a mostly uniform g_0 . Linear cavities exhibit hole burning at zero-detuning, otherwise known as the Lamb dip, but the ring cavity would not see a lamb dip. One would then anticipate that the linear cavity architecture could benefit from Doppler-free properties.

8.5 Conclusion

We characterize the strontium pulsed machine and identify a quasi-continuous regime where the atom number is instantaneously stable to study bi-stability. This quasi-continuous regime was found by tracking the cavity-coupled atom number during the transit of the atom cloud through the cavity mode by off-resonant probing the dressed cavity modes.

With the available 2 ms window of quasi-stable coupled atom number, we use an FM-spectroscopy approach that resembles NICE-OHMS to extract the full complex cavity transmission and study this during sweeping of the laser while the cavity follows the laser with a PDH piezo lock. The resulting signal has very good signal-to-noise and we can adjust the probing power with high precision over a large dynamic range.

For a range of cavity pump rates, we plot values related to the complex cavity transmission for 3 million cavity-coupled atoms. Using a model intended for a ring-cavity geometry, we show it can describe most of the steady-state features of the data by only tweaking the cavity coupling rate by a factor of 1/3. We discuss this factor could be well justified due to the differences between a ring and linear cavity. We cannot rule out that this

factor of $1/3$ comes from a calculation error, but anyway, a complete model for a linear cavity will be developed in future work.

Parameters interesting for the discussion of this technique as a frequency reference are extracted like the spread of frequencies and phase gradient, which gives an insight into a minimum achievable linewidth for laser stabilized to a driven cavity QED system continuously replenished with a cold atom beam.

Chapter 9

The Dissipative Ring Trap Concept

In a slight tangent to the previous chapters, we consider and simulation a novel ring trap using radiation pressure forces. Generating a continuous high phase-space density beam of neutral atoms is a common challenge in the field of ultra-cold atoms and is a theme in all of the topics of this thesis. As we discovered in the construction of our own beam machine in chapter 5, reaching high continuous atom fluxes in a small form factor can be challenging. A robust and compact device to generate such an atomic beam could enable extremely sensitive sensors to be realized in an application deployable form factor. Here, we present the concept and a numerical simulation for producing a high phase-space density beam in a compact form factor.

The Atom-Recycling Continuously Magneto-Optical Trap (Arc MOT) is a concept that is an extension of a regular MOT, but the beam of laser-cooled atoms is guided along a path that loops back on itself like a ring. The atomic beam continuously revolves around the ring with the potential of reaching a circulating phase-space density comparable to a MOT. However, since the beam is in motion, a dark gap can be introduced in the beam path to access the atoms by a probe laser beam for continuous frequency stabilization without perturbation from the MOT light.

9.1 Concept

The device has two parts: the light delivery optics and the magnetic field generation. The first part is a precision-machined inverse-conical shaped mirror that reflects a single donut-shaped laser beam into a plane, see illustration figure 9.1 e). The donut-shaped beam profile can be created with axicon optics¹. The nature of the conical mirror ensures the laser light arrives from six different directions with the correct polarization generated from a single laser beam, see figure 9.1 b). This configuration ensures the laser radiation pressure cools and compresses the atomic beam into a point while allowing free motion along the ring. A pyramid MOT uses a similar scheme using just one laser beam to generate six laser axes to form a conventional 3D MOT [88].

The second part of the device is a magnetic field that shifts the Zeeman levels of the atoms to provide a laser light force that varies with the atom's position relative to the zero-magnetic field point, like a conventional Magneto-Optical Trap (MOT). This could be achieved with a quadrupole magnetic field in the shape of a ring created by two pairs of concentric but flipped anti-Helmholtz electromagnets or also with permanent magnets, see figure 9.1 c).

The whole device is under high/ultra-high vacuum to minimize the circulating atoms collisions with the atmosphere. The atomic beam can be introduced into the ring in several different ways, for example, from above or a small hole drilled into the mirror. Optical access to interact with the atoms can also be achieved in several ways. One way could be cutting out a small 'sector' of the mirror and letting the circulating atoms travel ballistically over the gap, where they can be briefly interrogated with another laser beam. A 10° sector is considered in the simulations later in the chapter.

Figure 9.1 provides an example geometry for the Arc MOT, and specific proportions will vary depending on the atom, transition, and application.

Similar schemes with the goal of realizing a compact ring trap have been attempted in [89, 90, 88] and [91] but without the unique conical mirror arrangement detailed here. However, conical mirrors have been used to focus atomic beams and make compact MOTs but without the idea of a stable circulating cloud created guided by the unique magnetic field geometry.

¹Axicon optics use special mirrors or lenses with conical surfaces and tends to produce a ring-shaped distribution of light.

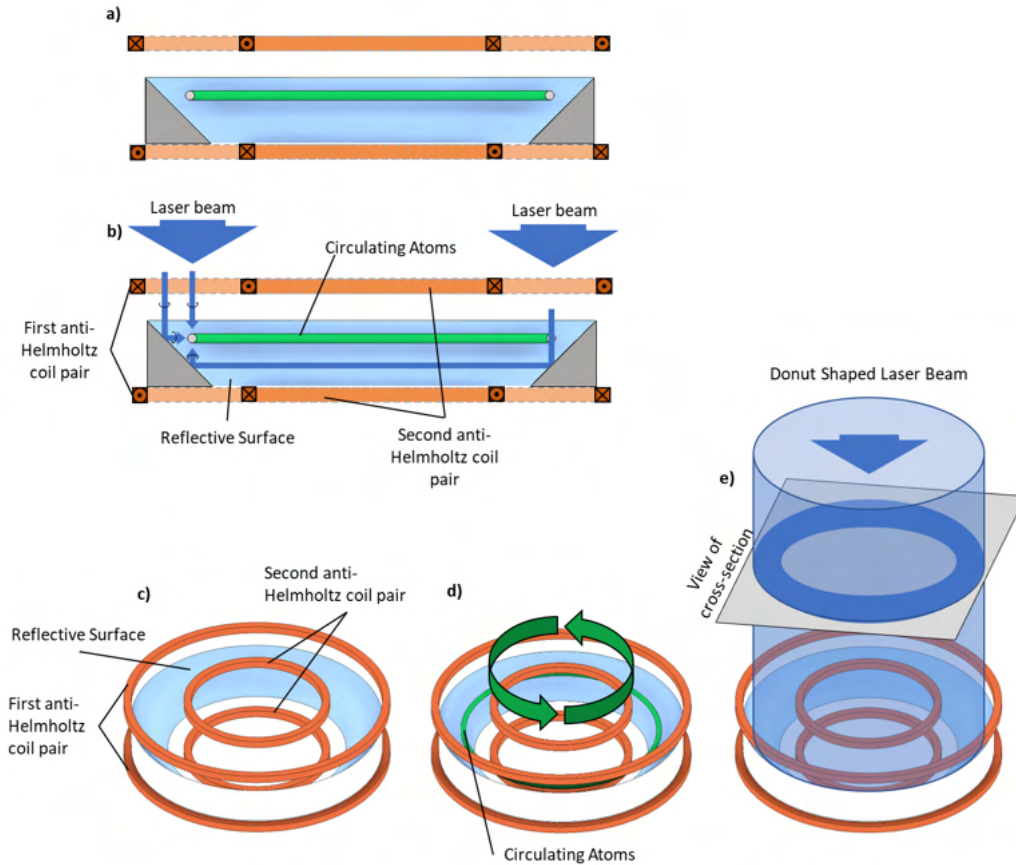


Figure 9.1: **Arc MOT Illustration.** The specifics will vary depending on the chosen atom and cooling/interrogation transitions. Figure a) is a cross-section of the mirror and coils, the direction of current flow in the coils depicted with crosses and dots, b) is an annotated version of a) with arrows illustrating the path of the laser beams. We omit the 4th beam acting “outward” because this is not required for compressing the revolving atom ring, but it is still there. c) is a 3D oblique view with annotations, d) shows the circulating ring of atoms, e) shows the donut-shaped laser beam required to illuminate the Arc MOT.

9.2 Preparing the Simulation

To simulate the Arc MOT, we use the PyLCP python package [92]. We need to define the magnetic vector field, the four laser beams with their corresponding k-vector, intensity, and polarization for every given point in a 3D cylindrical space. We use ^{88}Sr and the $^1\text{S}_0 \rightarrow ^1\text{P}_1$ transition at 461 nm with $\gamma/2\pi = 30$ MHz linewidth. In our mean-field simulation that takes an average force per atom, we neglect:

- Optical density approaching >0.1 , which affects light that passes twice through the ring of atoms.
- Light and magnetic field irregularities from limits of practical implementation, e.g., imperfect optics, imperfect alignment, stray magnetic fields, etc.

If the optical density is large enough to cause an issue, that means we are already approaching the atomic density of a conventional 3D MOT, and the Arc MOT would be a huge success. Alternatively, the optical depth problem can be navigated by changing to a less abundant (but perhaps more useful or interesting) isotope to reduce the flux, like ^{87}Sr .

To aid in the description of the various equations to describe the Arc MOT, we will switch between cylindrical and Cartesian coordinate systems:

$$r_{\text{cylindrical}} = \begin{bmatrix} \rho \\ \theta \\ z \end{bmatrix}, \quad r_{\text{cart}} = \begin{bmatrix} x \\ y \\ z \end{bmatrix} = \begin{bmatrix} \rho \cos \theta \\ \rho \sin \theta \\ z \end{bmatrix} \quad (9.1)$$

The magnetic quadrupole ring geometry can be approximated by:

$$B(r) = \alpha \begin{bmatrix} (\rho - r_{\text{ring}}) \cos(\theta) \\ (\rho - r_{\text{ring}}) \sin(\theta) \\ -z \end{bmatrix} \quad (9.2)$$

Where α is the field gradient, r_{ring} is the 0-field ring radius, see the illustration in figure 9.2. This model is a simplification, especially in the centre of the Arc MOT, but should be sufficient to capture the main details of the Arc MOT.

The conical mirror will act to focus the laser beam onto its axis of symmetry, meaning there is a varying laser intensity on the plane perpendicular

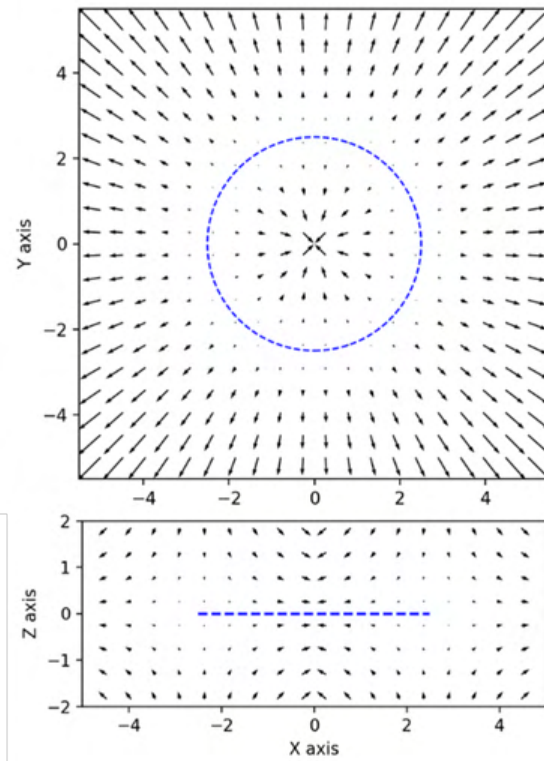


Figure 9.2: **Magnetic vector field in $x-y$ and $x-z$.** The arrow direction and magnitude represent the projection of the B-field field onto the $x-y$ ($x-z$) plane at the cross-section where $z = 0$ ($y = 0$), and the dashed blue line indicates the zero B-field ring whose radius is defined by r_{ring} .

to z . We can group the laser field into four separate fields, the first two are *upward* and *downward*, and they point along the z -axis fields and can be described by:

$$s_{downward}(r) = s_{upward}(r) = s \quad (9.3)$$

$$k_{downward}(r) = -k_{upward}(r) = \begin{bmatrix} 0 \\ 0 \\ -1 \end{bmatrix} \quad (9.4)$$

Where s is the laser intensity defined in units of the saturation parameter. Laser fields *inward* and *outward* point towards and away from the z -axis and are described by:

$$s_{inward}(r) = s_{outward}(r) = s \frac{r_0 + z}{\rho + e} \quad (9.5)$$

$$-k_{inward}(r) = k_{outward}(r) = \begin{bmatrix} \cos(\theta) \\ \sin(\theta) \\ 0 \end{bmatrix} \quad (9.6)$$

Where r_0 , illustrated in figure 9.3, is the mirror radius at $z = 0$ and e is a small arbitrary number to prevent the focal point in the cone centre going to infinite and avoiding divide by 0 errors in the simulation. Finally, we implement boundary conditions that restrict the laser field into a realistic geometry, described in table 9.1. With this implementation, if an atom hits a mirror edge, the atom will see a sudden drop in laser intensity and become lost to the Arc MOT. We also implement a *notch*, a sector cut-out that could be used to interrogate the atoms during circulation in the ring.

A map of the laser intensity, including the boundary conditions, is shown in figure 9.3 with example values for r_0 , z_0 , and θ_0 that are the same used for the simulation.

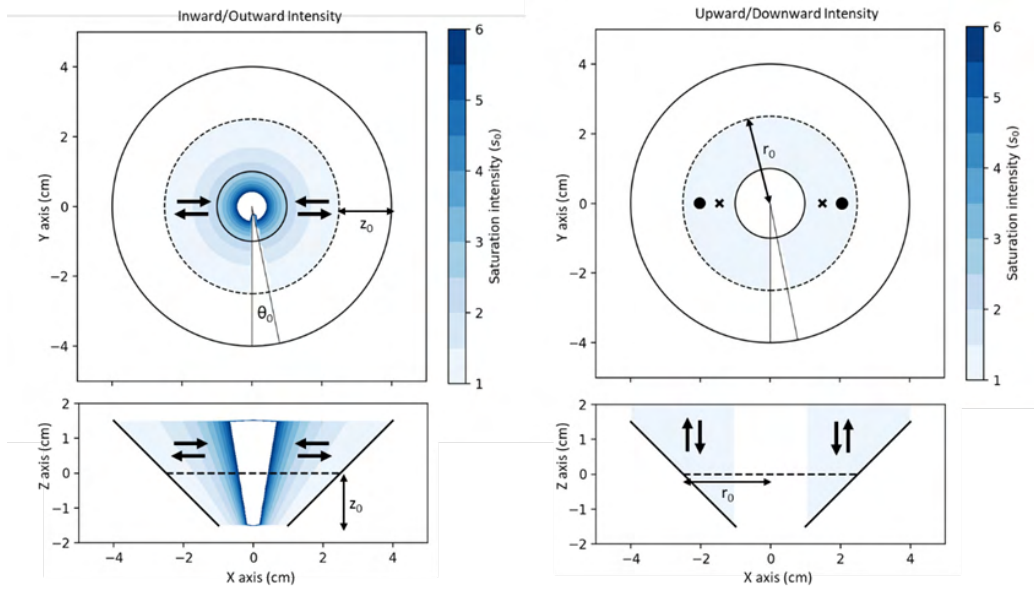


Figure 9.3: Laser Intensity Map. The left pair of subfigures shows the focusing inward/outward laser intensity field for (top) x - y at the cross-section $z = 0$, and (bottom) x - z for the cross-section $y = 0$. The right pair of figures shows the same intensity plots but for the upward/downward laser beams. Bold arrows are used as an aid to show the k -vector of the laser. Large laser intensities close to the centre are omitted and shown in white. The bold black lines indicate the outlines for the axicon mirror. The mirror radius $r_0 = 2.5$ cm, indicated with black dashed circles/lines on all figures and $z_0 = 1.5$ cm which defines the height of the mirror and inner and outer diameter. The notch represents by θ_0 is about 10° and seen as a missing sector of the mirror.

Boundary Condition	Value
$\rho < r_0 - z_0$	
$\rho > r_0 + z_0$	$s_{downward}(r) = s_{upward}(r) = 0$
$\rho > z + r_0$	
$z < z_0$	
$z > z_0$	$s_{inward}(r) = s_{outward}(r) = 0$
$\rho > z + r_0$	
$\theta > \theta_0$	$s_{inward}(r) = s_{outward}(r) = 0$ $s_{downward}(r) = s_{upward}(r) = 0$

Table 9.1: **Boundary Conditions for Arc MOT.** The first 6 boundary conditions come from the conical mirror, and the last boundary condition depending on θ is an additional gap in the conical mirror for interrogation of the circulating atoms. z_0 defines half the height of the conical mirror; see figure 9.3

9.3 Static Reference Frame Simulation

Setting the magnetic field gradient α to be $40 \text{ G}\cdot\text{cm}^{-1}$ and using a laser intensity equivalent to the saturation parameter of 0.1, laser detuning -0.7γ , we can start to study the dynamics of atoms in the ring shown in figure 9.4. We inject 9 atoms with velocities between 10 and $90 \text{ m}\cdot\text{s}^{-1}$ into the Arc MOT from the starting position $[-1.5, -3.5, 0.5] \text{ cm}$ and follow their trajectory as they enter the interaction region. A slight offset in z is added to observe the compression in z . Only once the atom enters the region of $\rho < r_0 + 0.5$ do they feel any radiation pressure.

In the top-left sub-figure of figure 9.4, the atomic beam is separated into different orbits depending on their initial velocity entering the Arc MOT, and slower velocity atoms tend towards an orbit closer to the zero-field radius r_{ring} . This clearly reflects the nature of orbits that for a constant acceleration, the orbital radius must change for a higher velocity. At $r_{\text{ring}} = 0$, there is no Zeeman shift, and therefore, inward and outward radiation pressure are balanced, and there is no net acceleration, so only zero-velocity atoms can exist at $\rho = r_{\text{ring}}$. In the top-right subfigure, we see faster atoms also orbit at a higher period.

Some atom velocities greater than $60 \text{ m}\cdot\text{s}^{-1}$ are not caught in the trap and are seen with trajectories heading outside of the Arc MOT. This is also seen in a regular 3D MOT because the Doppler shift of the atom is larger than the detuning -0.7γ .

The compression in the z -axis is completed by the 3-4 period and the time this takes is shared by all the atoms.

The notch has a minimal effect on the circulating atoms, but it does provide a slight acceleration each period, which can be seen by the thickening of the overlapping trajectories of the outermost orbit, and will eventually hit the edge of the mirror. An acceleration or deceleration after each period can be very useful for keeping atoms in the ring if there happens to be momentum loss or gain from other mechanisms and is an important subject for future investigations. It also raises interesting possibilities of producing an orbit-dependent acceleration or deceleration, which could be a method to compress all atoms into one orbital radius. Then, the velocity distribution of the circulating atoms would be very uniform or monochromatic².

²We term monochromatic here by borrowing the analogy of narrow-spectral spread and applying it to a narrow longitudinal velocity spread.

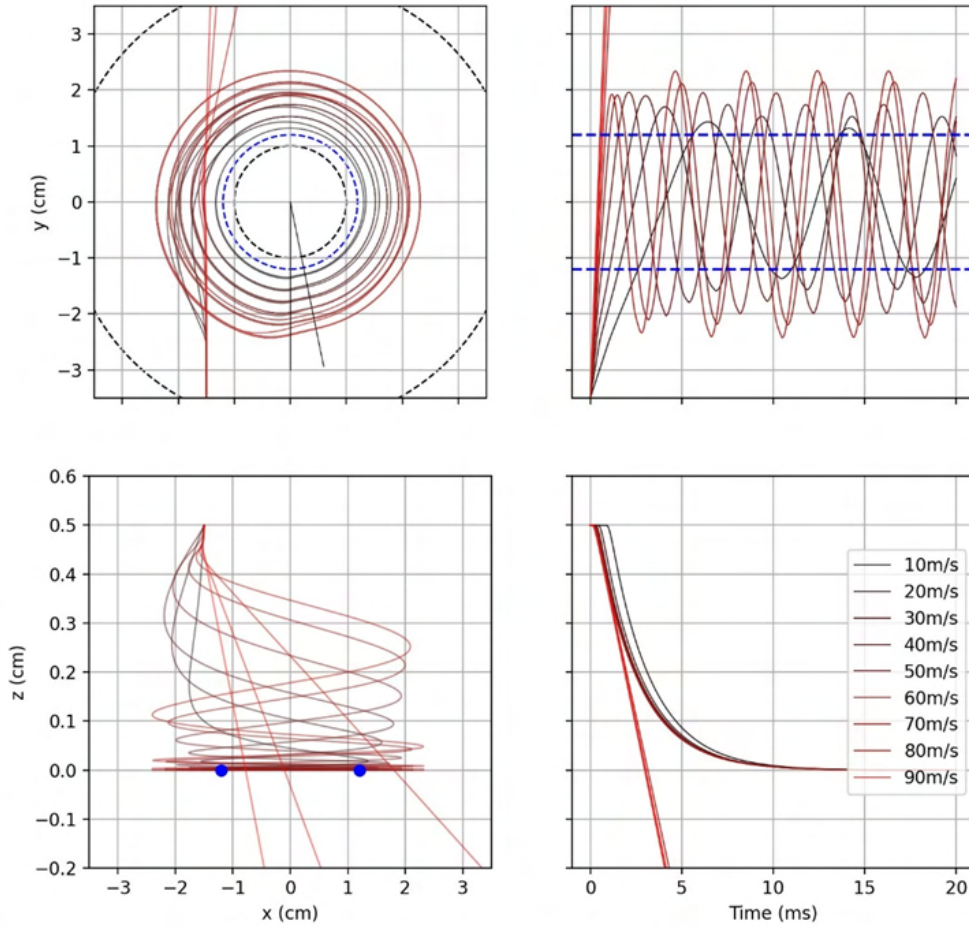


Figure 9.4: **Rotating Atoms in Arc MOT Simulation.** The trajectories of atoms entering the Arc MOT are plotted in $x-y$ ($x-z$) space top-left (bottom-left), and the y (z) versus time is plotted top-right (bottom-right). The blue points and dashed lines represent the radius of the zero B-field equivalent to $r_{\text{ring}} = 1.2$ cm. The black dashed lines represent the axicon mirror edges projected onto the $x-y$ plane.

9.4 Conclusion

The Arc MOT could be a compact method of storing atoms in a circulating ring. The main novelty is the ability to introduce a break in the mirror optics while maintaining the circulating atoms in the MOT and allowing probing of atoms in a relatively dark space. How dark this region can get, and the impact of the MOT magnetic field is a topic for further investigation. The simulations validate the underlying principle is sound with idealized geometry, and future simulations should investigate loss mechanisms, transitions between orbits in the ring, the effect of varying the magnetic field during the circulating ring, and the ultimate phase-space densities achievable. We also do not investigate interrogation methods in the notch region, but this is clearly interesting for cavity-enhanced and continuous interrogation methods like NICE-OHMS and super-radiance.

The Arc MOT geometry could be compressed further for better optical access by considering a custom Fresnel mirror such as the one in reference [93].

Chapter 10

Conclusion and Outlook

We have taken a broad look and set the foundation of cavity-enhanced phase measurements on atomic clouds, both in the low atom number (linear) and high atom number (non-linear) regimes.

NICE-OHMS is understood to be a powerful method for making concentration measurements of low-density species of atoms or molecules, typically on transitions with broad linewidths. However, it is still an open question whether NICE-OHMS is suitable for frequency metrology on narrow linewidth transitions and if it can fully benefit from the enhanced interaction length afforded by the finesse of the cavity. These questions will be answered by the next generation of PhD students working on the beam machine.

We have raised several challenges regarding the use of NICE-OHMS for frequency metrology. Cavity optical losses can diminish the benefit of the cavity finesse on the sensitivity of the measurement. The large power enhancement in the cavity leads to large intra-cavity intensities and we propose a solution to operate with Carrier-Depleted NICE-OHMS. The sidebands are also resonantly enhanced, and the AC stark shift from the ± 1 and ± 2 sidebands can become larger than the transition linewidth. A constant shift is completely acceptable for a clock and can be systematically accounted for; however, since the linear cavity produces a standing wave, the AC-stark shift varies periodically. More study is required to understand how this periodically varying AC-Stark shift affects the center of the Doppler-free saturation feature.

An atomic clock based on an atomic beam has the potential to evade Dick noise, which currently limits the stability of the best optical neutral atomic clocks. To avoid this noise with a different atomic clock architecture, we built

a strontium beam machine from scratch, employing a Zeeman slower and 1D angled MOT to deliver neutral atoms for continuous frequency measurements using NICE-OHMS. We characterized the atomic beam to have a transverse temperature of less than 4 mK along the cavity axis, traveling on average at $23 \text{ m} \cdot \text{s}^{-1}$, and with a flux of $0.55(22) \cdot 10^9$ atoms per second through the cavity volume of a 5000 finesse optical cavity. The microwave electronics are built and tested, but the first NICE-OHMS signal from the atoms remains elusive. A few technical issues are to blame. We recommend replacing the optical cavity with one with higher finesse and lower transmission losses, the EOM with one with lower losses, and the high-bandwidth photodetector with one with lower detection noise.

Reaching high atomic fluxes was tough, which was anticipated to be the main challenge for an atomic clock based on a beam. Novel cooling designs and methods may be the only path forward for reaching atomic densities that resemble those used in pulsed optical atomic frequency standards. Hence, we also presented the circulating ring MOT (Arc MOT), which could be a novel and compact method for achieving higher atomic densities. The design will be tested experimentally in the future.

Taking cavity-enhanced phase measurements to the limit of very large atom numbers, we enter a new regime characterized by different physics. In the strong collective cooperativity regime, we see strong non-linearities and hysteresis of the atom-cavity system, which we describe reasonably well with a mean-field model. A numerical model will be required to understand the dynamics fully. Inspired by the NICE-OHMS measurement scheme, we probed an atom-cavity system in the strong collective cooperativity regime with I-Q detection to reconstruct the full complex cavity field transmission. This measurement technique has proven very versatile, and we use it to measure the effective coupled atom number and take spectra over atomic resonance to study the bi-stability regime. Operating at powers just above bi-stability, we find an ideal frequency discriminator signal exhibiting an almost step-function response close to atomic resonance. Several technical challenges remain to be overcome before a signal like this can continuously stabilize a frequency standard. One such challenge is limiting the heating of the atomic beam during continuous interrogation.

The origin and nature of the π step in phase and how it results from collective atom dynamics is a topic for future investigation. We look towards recent publications [94, 95] on light interaction with dense atomic ensembles that hint at rich physics still to be explored in these systems.

Appendix A

Old Clogged Sr Oven Nozzle

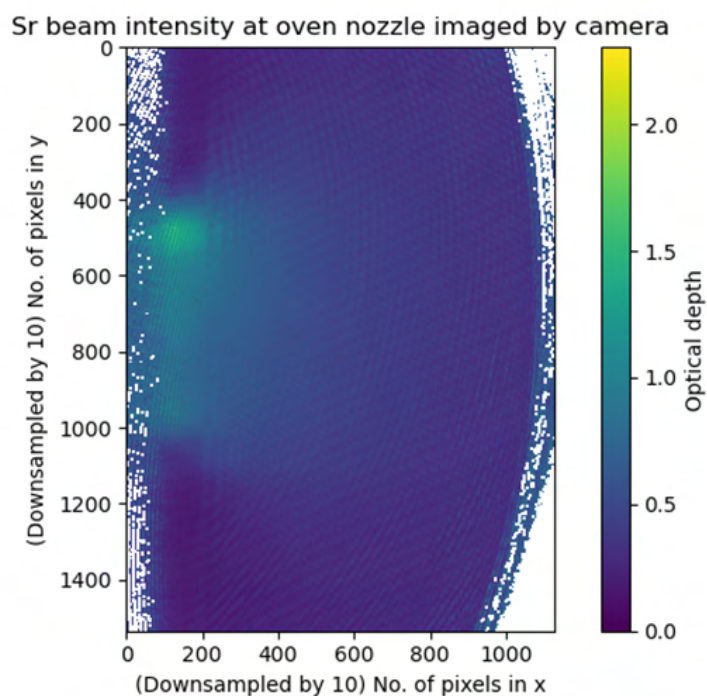


Figure A.1: **Absorption Image of Clogged Oven Nozzle.** Suspecting that the capillary tubes were clogged and that there was further strontium leaking from the oven, this image was taken to identify where the strontium was going. The two clear peaks in optical depth do not correspond to where the capillary tubes are, but rather the location of two screws securing the capillary tube lid. The peak should be exactly in the center at 700 y-pixel location.

Appendix B

Atom Number and Flux Calculations

Parameter	Value	Uncertainty	Unit
Power reaching photodiode	10.4	1%	uW
Power interacting with atoms	15.1	5%	uW
Voltage on photodetector for 10.4 uW	9.38	1%	V
Calibration of photodetector 70dB gain	1.11	1%	uW/V
Power scattered by atoms	4.44	5%	nW
Effective scattered power	6.464	5%	nW
Beam waist diameter	0.334	5%	mm
	0.0334	5%	cm
Scaling of probe vs cavity beam area	3.79	20%	
Beam Area	0.000888	10%	cm ²
Gaussian Beam Intensity	34,009	11%	uW/cm ²
Saturation intensity	40.76	1%	mW/cm ²
Saturation parameter	0.8904	11%	
Excitation probability	0.2355	1.40%	
Energy in photon	4.31E-19	1%	J
Scattered power per atom	3.10 e-12	1.40%	W/atom
Total atoms in probe beam path	2,085	5.20%	atoms
Total atoms in cavity volume	7902	21%	atoms
Average velocity	23	10%	m/s
Atom transit time	1.45e-5	22%	s
Detected Atom Flux	1.438E8	31%	atom/s
Atom flux adjusted for cavity volume	545,760,000	37%	atom/s

Table B.1: Calculation and error propagation for estimating the number of atoms in the beam machine travelling through the cavity volume of the optical cavity.

Appendix C

Atom-Cavity Parameter Summary Table

Table C.1 shows a list of important parameters for the beam machine described in the beam machine chapter 5, and pulsed machine which is the experiment used to generate the data in following chapter 8.

Parameter	Symbol	Beam Machine	Pulsed Machine
Atom Decay Rate	$\gamma/2\pi$	7.5 kHz	7.5 kHz
Cavity Architecture		Linear	Linear
Finesse	F	5000	1000
FSR	$\omega_{\text{FSR}}/2\pi$	3.7 GHz	781 MHz
Cavity Length	L_{cav}	37 mm	192 mm
Cavity Power Decay FWHM	$\kappa/2\pi$	700 kHz	780 kHz
Mirror ROC	r_{OC}	4 m	9 m
Waist Radius	w_0	250 μm	500 μm
Atom Velocity	v_{transit}	23 $\text{m} \cdot \text{s}^{-1}$	-
Transit Time Broadening	$\Gamma_t/2\pi$	60 kHz	-
Peak Atom Number in Cavity	N_{atom}	7,200	>50,000,000
Flux Through Cavity Volume	Φ_{atom}	$0.5 \cdot 10^9$	Pulsed
Doppler FWHM	$\Gamma_D/2\pi$	2 MHz	40 kHz
Saturation at 1 nW		108	5
Saturation at Single Photon	s_1	6	0.11
Atom-Cavity Coupling	$g/2\pi$	6.4 kHz	0.87 kHz
Single Atom Cooperativity	C	$7.9 \cdot 10^{-3}$	$4.4 \cdot 10^{-4}$

Table C.1: **Cavity-Atom Parameters.** Here the important values for the beam machine detailed in this thesis are contrasted with the pulsed machine

References

- [1] A. Aeppli et al. In: *Physical Review Letters* 133.2 (July 2024), p. 023401. DOI: 10.1103/PhysRevLett.133.023401.
- [2] S. M. Brewer et al. In: *Physical Review Letters* 123.3 (July 2019), p. 033201. DOI: 10.1103/PhysRevLett.123.033201.
- [3] D. DeMille, J. M. Doyle, and A. O. Sushkov. In: *Science* 357.6355 (Sept. 2017), pp. 990–994. DOI: 10.1126/science.aal3003.
- [4] M. Filzinger et al. In: *Physical Review Letters* 130.25 (June 2023), p. 253001. DOI: 10.1103/PhysRevLett.130.253001.
- [5] X. Zheng et al. In: *Nature Communications* 14.1 (Aug. 2023), p. 4886. ISSN: 2041-1723. DOI: 10.1038/s41467-023-40629-8.
- [6] R. M. Godun et al. In: *Physical Review Letters* 113.21 (Nov. 2014), p. 210801. DOI: 10.1103/PhysRevLett.113.210801.
- [7] N. Dimarcq et al. In: *Metrologia* 61.1 (Jan. 2024), p. 012001. ISSN: 0026-1394. DOI: 10.1088/1681-7575/ad17d2.
- [8] T. W. Hänsch et al. In: *Philosophical Transactions of the Royal Society A: Mathematical, Physical and Engineering Sciences* (Aug. 2005). DOI: 10.1098/rsta.2005.1639.
- [9] G. Marra et al. In: *Science* 361.6401 (Aug. 2018), pp. 486–490. ISSN: 0036-8075, 1095-9203. DOI: 10.1126/science.aat4458.
- [10] Z. L. Newman et al. In: *Optica* 6.5 (May 2019), pp. 680–685. ISSN: 2334-2536. DOI: 10.1364/OPTICA.6.000680.
- [11] S. Kolkowitz et al. In: *Physical Review D* 94.12 (Dec. 2016), p. 124043. DOI: 10.1103/PhysRevD.94.124043.

- [12] J. Vig. In: *IEEE Transactions on Ultrasonics, Ferroelectrics, and Frequency Control* 40.5 (Sept. 1993), pp. 522–527. ISSN: 1525-8955. DOI: 10.1109/58.238104.
- [13] F. Riehle. Weinheim: Wiley-VCH, 2004. ISBN: 978-3-527-40230-4.
- [14] A. Quessada et al. In: *Journal of Optics B: Quantum and Semiclassical Optics* 5.2 (Apr. 2003), S150–S154. ISSN: 1464-4266. DOI: 10.1088/1464-4266/5/2/373.
- [15] J. Lodewyck, P. G. Westergaard, and P. Lemonde. In: *Physical Review A* 79.6 (June 2009), p. 061401. ISSN: 1050-2947, 1094-1622. DOI: 10.1103/PhysRevA.79.061401.
- [16] R. Hobson et al. In: *Optics Express* 27.26 (Dec. 2019), pp. 37099–37110. ISSN: 1094-4087. DOI: 10.1364/OE.27.037099.
- [17] G. W. Biedermann et al. In: *Physical Review Letters* 111.17 (Oct. 2013), p. 170802. ISSN: 0031-9007, 1079-7114. DOI: 10.1103/PhysRevLett.111.170802.
- [18] E. Oelker et al. In: *Nature Photonics* 13.10 (Oct. 2019), pp. 714–719. ISSN: 1749-4893. DOI: 10.1038/s41566-019-0493-4.
- [19] M. J. Martin et al. In: *Physical Review A* 84.6 (Dec. 2011), p. 063813. ISSN: 1050-2947, 1094-1622. DOI: 10.1103/PhysRevA.84.063813.
- [20] D. Barberena et al. In: *Comptes Rendus. Physique* 24.S3 (June 2023), pp. 1–14. ISSN: 1878-1535. DOI: 10.5802/crphys.146.
- [21] S. L. Kristensen et al. In: *Physical Review Letters* 130.22 (May 2023), p. 223402. ISSN: 0031-9007, 1079-7114. DOI: 10.1103/PhysRevLett.130.223402.
- [22] U. Sterr et al. In: San Diego, CA: SPIE Optical Engineering + Applications, Aug. 2009, 74310A. DOI: 10.1117/12.825217.
- [23] J. M. Robinson et al. In: *Optica* 6.2 (Feb. 2019), pp. 240–243. ISSN: 2334-2536. DOI: 10.1364/OPTICA.6.000240.
- [24] D. Kleppner, H. M. Goldenberg, and N. F. Ramsey. In: *Physical Review* 126.2 (Apr. 1962), pp. 603–615. ISSN: 0031-899X. DOI: 10.1103/PhysRev.126.603.
- [25] M. A. Norcia et al. In: *Science Advances* 2.10 (Oct. 2016), e1601231. ISSN: 2375-2548. DOI: 10.1126/sciadv.1601231.

- [26] M. A. Norcia and J. K. Thompson. In: *Physical Review X* 6.1 (Mar. 2016), p. 011025. ISSN: 2160-3308. DOI: 10.1103/PhysRevX.6.011025.
- [27] H. Liu et al. In: *Physical Review Letters* 125.25 (Dec. 2020), p. 253602. ISSN: 0031-9007, 1079-7114. DOI: 10.1103/PhysRevLett.125.253602.
- [28] J. Tiedau et al. In: *Physical Review Letters* 132.18 (Apr. 2024), p. 182501. DOI: 10.1103/PhysRevLett.132.182501.
- [29] A. Louchet-Chauvet et al. In: *New Journal of Physics* 12.6 (June 2010), p. 065032. ISSN: 1367-2630. DOI: 10.1088/1367-2630/12/6/065032.
- [30] D. Oblak et al. In: *Physical Review A* 71.4 (Apr. 2005), p. 043807. ISSN: 1050-2947, 1094-1622. DOI: 10.1103/PhysRevA.71.043807.
- [31] J. G. Bohnet et al. In: *Nature Photonics* 8.9 (Sept. 2014), pp. 731–736. ISSN: 1749-4893. DOI: 10.1038/nphoton.2014.151.
- [32] M. Schulte et al. In: *Nature Communications* 11.1 (Nov. 2020), p. 5955. ISSN: 2041-1723. DOI: 10.1038/s41467-020-19403-7.
- [33] H. J. Metcalf and P. Van Der Straten. Ed. by R. S. Berry et al. Graduate Texts in Contemporary Physics. New York, NY: Springer New York, 1999. ISBN: 978-0-387-98728-6 978-1-4612-1470-0. DOI: 10.1007/978-1-4612-1470-0.
- [34] J. Söding et al. In: *Physical Review Letters* 78.8 (Feb. 1997), pp. 1420–1423. ISSN: 0031-9007, 1079-7114. DOI: 10.1103/PhysRevLett.78.1420.
- [35] J. P. Bartolotta et al. In: *Physical Review A* 98.2 (Aug. 2018), p. 023404. ISSN: 2469-9926, 2469-9934. DOI: 10.1103/PhysRevA.98.023404.
- [36] P. Morzyński et al. In: *Scientific Reports* 5.1 (Dec. 2015), p. 17495. ISSN: 2045-2322. DOI: 10.1038/srep17495.
- [37] N. Ramsey. Oxford classic texts in the physical sciences. Oxford : Oxford ; New York: Clarendon Press ; Oxford University Press, 2005. ISBN: 978-0-19-852021-4.
- [38] C.-C. Chen et al. In: *Physical Review Applied* 12.4 (Oct. 2019), p. 044014. ISSN: 2331-7019. DOI: 10.1103/PhysRevApplied.12.044014.
- [39] J. Olson et al. In: *Physical Review Letters* 123.7 (Aug. 2019), p. 073202. ISSN: 0031-9007, 1079-7114. DOI: 10.1103/PhysRevLett.123.073202.

- [40] I. Manai et al. In: *Journal of Physics B: Atomic, Molecular and Optical Physics* 53.8 (Apr. 2020), p. 085005. ISSN: 0953-4075, 1361-6455. DOI: 10.1088/1361-6455/ab707f.
- [41] T. Yang et al. In: *The European Physical Journal D* 69.10 (Oct. 2015), p. 226. ISSN: 1434-6060, 1434-6079. DOI: 10.1140/epjd/e2015-60288-y.
- [42] J. R. K. Cline et al. In: *arXiv* (Oct. 2022). DOI: 10.48550/arXiv.2211.00158.
- [43] R. Takeuchi et al. In: *Applied Physics Express* 16.4 (Apr. 2023), p. 042003. ISSN: 1882-0778, 1882-0786. DOI: 10.35848/1882-0786/accb3c.
- [44] H. Katori. In: *Applied Physics Express* 14.7 (July 2021), p. 072006. ISSN: 1882-0778, 1882-0786. DOI: 10.35848/1882-0786/ac0e16.
- [45] J. L. Hall and C. J. Bordé. In: *Applied Physics Letters* 29.12 (Dec. 1976), pp. 788–790. ISSN: 0003-6951, 1077-3118. DOI: 10.1063/1.88949.
- [46] J. Ye, L.-S. Ma, and J. L. Hall. In: *Journal of the Optical Society of America B* 15.1 (Jan. 1998), p. 6. ISSN: 0740-3224, 1520-8540. DOI: 10.1364/JOSAB.15.000006.
- [47] O. Axner, W. Ma, and A. Foltynowicz. In: *Journal of the Optical Society of America B* 25.7 (July 2008), p. 1166. ISSN: 0740-3224, 1520-8540. DOI: 10.1364/JOSAB.25.001166.
- [48] Y. Zhou et al. In: *Atmospheric Measurement Techniques* 12.3 (Mar. 2019), pp. 1807–1814. ISSN: 1867-8548. DOI: 10.5194/amt-12-1807-2019.
- [49] W. Ma, A. Foltynowicz, and O. Axner. In: *Journal of the Optical Society of America B* 25.7 (July 2008), p. 1144. ISSN: 0740-3224, 1520-8540. DOI: 10.1364/JOSAB.25.001144.
- [50] E. A. Curtis et al. In: *Journal of the Optical Society of America B* 34.5 (May 2017), p. 950. ISSN: 0740-3224, 1520-8540. DOI: 10.1364/JOSAB.34.000950.
- [51] S. A. Schäffer et al. In: *Physical Review A* 96.1 (July 2017), p. 013847. ISSN: 2469-9926, 2469-9934. DOI: 10.1103/PhysRevA.96.013847.
- [52] M. R. Henriksen. PhD thesis. University of Copenhagen, 2019.

- [53] J. Ye and T. W. Lynn. In: *Advances In Atomic, Molecular, and Optical Physics*. Vol. 49. Elsevier, 2003, pp. 1–83. ISBN: 978-0-12-003849-7. DOI: 10.1016/S1049-250X(03)80003-4.
- [54] D. Kedar et al. In: *Optica* 11.1 (Jan. 2024), p. 58. ISSN: 2334-2536. DOI: 10.1364/OPTICA.507655.
- [55] X. Zhou et al. In: *Physical Review A* 81.1 (Jan. 2010), p. 012115. ISSN: 1050-2947, 1094-1622. DOI: 10.1103/PhysRevA.81.012115.
- [56] J. E. Sansonetti and G. Nave. In: *Journal of Physical and Chemical Reference Data* 39.3 (Sept. 2010), p. 033103. ISSN: 0047-2689, 1529-7845. DOI: 10.1063/1.3449176.
- [57] J. T. M. Walraven. 2016.
- [58] C. J. Foot. Repr. (twice with corr.) Oxford master series in physics Atomic, optical, and laser physics 7. Oxford: Oxford Univ. Press, 2011. ISBN: 978-0-19-850696-6 978-0-19-850695-9.
- [59] B. T. R. Christensen et al. In: *Physical Review A* 92.5 (Nov. 2015), p. 053820. ISSN: 1050-2947, 1094-1622. DOI: 10.1103/PhysRevA.92.053820.
- [60] J. J. Tollett et al. In: *Physical Review Letters* 65.5 (July 1990), pp. 559–562. ISSN: 0031-9007. DOI: 10.1103/PhysRevLett.65.559.
- [61] P. G. Westergaard et al. In: *Physical Review Letters* 114.9 (Mar. 2015), p. 093002. ISSN: 0031-9007, 1079-7114. DOI: 10.1103/PhysRevLett.114.093002.
- [62] M. Tang, S. A. Schaffer, and J. Westenk. In: ().
- [63] M. Tang, S. A. Schäffer, and J. H. Müller. In: *Physical Review A* 106.6 (Dec. 2022), p. 063704. DOI: 10.1103/PhysRevA.106.063704.
- [64] S. A. Schäffer et al. In: *Physical Review A* 101.1 (Jan. 2020), p. 013819. DOI: 10.1103/PhysRevA.101.013819.
- [65] H. Liu et al. In: *Physical Review Letters* 125.25 (Dec. 2020), p. 253602. ISSN: 0031-9007, 1079-7114. DOI: 10.1103/PhysRevLett.125.253602.
- [66] C. J. Bordé et al. In: *Physical Review A* 14.1 (July 1976), pp. 236–263. ISSN: 0556-2791. DOI: 10.1103/PhysRevA.14.236.
- [67] S. Bennetts. PhD thesis. University of Amsterdam, 2019.

- [68] M. Schioppo et al. In: *Review of Scientific Instruments* 83.10 (Oct. 2012), p. 103101. ISSN: 0034-6748, 1089-7623. DOI: 10.1063/1.4756936.
- [69] E. Staub. MA thesis. Technical University of Munich, 2019.
- [70] S. A. Schaffer. PhD thesis. University of Copenhagen, 2019.
- [71] E. Bohr. PhD thesis. University of Copenhagen, 2023.
- [72] D. Z. Anderson. In: *Applied Optics* 23.17 (Sept. 1984), p. 2944. ISSN: 0003-6935, 1539-4522. DOI: 10.1364/AO.23.002944.
- [73] L. Neuhaus et al. In: *2017 Conference on Lasers and Electro-Optics Europe & European Quantum Electronics Conference (CLEO/Europe-EQEC)*. Munich, Germany: IEEE, June 2017, pp. 1–1. ISBN: 978-1-5090-6736-7. DOI: 10.1109/CLEOE-EQEC.2017.8087380.
- [74] J. Chen. In: *Science Bulletin* 54.3 (Feb. 2009), pp. 348–352. ISSN: 2095-9273, 2095-9281. DOI: 10.1007/s11434-009-0073-y.
- [75] K. Debnath, Y. Zhang, and K. Mølmer. In: *Physical Review A* 98.6 (Dec. 2018), p. 063837. ISSN: 2469-9926, 2469-9934. DOI: 10.1103/PhysRevA.98.063837.
- [76] M. A. Norcia et al. In: *Physical Review X* 8.2 (May 2018), p. 021036. ISSN: 2160-3308. DOI: 10.1103/PhysRevX.8.021036.
- [77] S. B. Jäger et al. In: *Physical Review A* 104.3 (Sept. 2021), p. 033711. ISSN: 2469-9926, 2469-9934. DOI: 10.1103/PhysRevA.104.033711.
- [78] D. Meiser et al. In: *Physical Review Letters* 102.16 (Apr. 2009), p. 163601. ISSN: 0031-9007, 1079-7114. DOI: 10.1103/PhysRevLett.102.163601.
- [79] H. Tanji-Suzuki et al. In: *Advances in Atomic Molecular and Optical Physics* 60 (Jan. 2011), pp. 201–237. DOI: 10.1016/B978-0-12-385508-4.00004-8.
- [80] D. Rivero et al. In: *New Journal of Physics* 25.9 (Sept. 2023), p. 093053. ISSN: 1367-2630. DOI: 10.1088/1367-2630/acf954.
- [81] R. J. Thompson, G. Rempe, and H. J. Kimble. In: *Physical Review Letters* 68.8 (Feb. 1992), pp. 1132–1135. DOI: 10.1103/PhysRevLett.68.1132.
- [82] J. Gripp, S. L. Mielke, and L. A. Orozco. In: *Physical Review A* 56.4 (Oct. 1997), pp. 3262–3273. ISSN: 1050-2947, 1094-1622. DOI: 10.1103/PhysRevA.56.3262.

- [83] H. M. Gibbs, S. L. McCall, and T. N. C. Venkatesan. In: *Physical Review Letters* 36.19 (May 1976), pp. 1135–1138. ISSN: 0031-9007. DOI: 10.1103/PhysRevLett.36.1135.
- [84] D. A. Tieri et al. In: *Physical Review A* 92.1 (July 2015), p. 013817. ISSN: 1050-2947, 1094-1622. DOI: 10.1103/PhysRevA.92.013817.
- [85] E. A. Bohr et al. In: *Nature Communications* 15.1 (Feb. 2024), p. 1084. ISSN: 2041-1723. DOI: 10.1038/s41467-024-45420-x.
- [86] S. L. Kristensen. PhD thesis. University of Copenhagen, 2023.
- [87] E. Suarez et al. In: *Physical Review A* 107.2 (Feb. 2023), p. 023714. DOI: 10.1103/PhysRevA.107.023714.
- [88] S. Ravenhall, B. Yuen, and C. Foot. In: *Optics Express* 29.14 (July 2021), p. 21143. ISSN: 1094-4087. DOI: 10.1364/OE.423662.
- [89] K. I. Lee et al. In: *Optics Letters* 21.15 (Aug. 1996), p. 1177. ISSN: 0146-9592, 1539-4794. DOI: 10.1364/OL.21.001177.
- [90] J. Wu, F. Moscatelli, and E. Oh. In: *Optics Express* 14.12 (2006), p. 4969. ISSN: 1094-4087. DOI: 10.1364/OE.14.004969.
- [91] M. Morinaga. In: *Journal of the Physical Society of Japan* 77.10 (Oct. 2008), p. 104402. ISSN: 0031-9015, 1347-4073. DOI: 10.1143/JPSJ.77.104402.
- [92] S. Eckel et al. Nov. 2020. DOI: 10.48550/arXiv.2011.07979.
- [93] S. Bondza et al. Oct. 2023. DOI: 10.48550/arXiv.2310.14861.
- [94] P. W. Courteille et al. Sept. 2024. DOI: 10.48550/arXiv.2409.06042.
- [95] E. Y. Song et al. Aug. 2024. DOI: 10.48550/arXiv.2408.11086.